Strategies to encode information with glutamate release in synapses of the *Danio Rerio* visual system

Lea Darnet

A thesis submitted for the Degree of Doctor of Philosophy in the University of Sussex

May 2018

Declaration

I hereby declare that this thesis has not been and will not be, submitted in whole or in part to another University for the award of any other degree.

Signature:

Part of chapter 3 (Data from 3.3.1,3.3.2. and 3.3.4.) and chapter 4 (data from 4.3.2., 4.3.3. and 4.3.4.), results will be published:

James, B.*, Darnet, L.*, Moya-Diaz, J.*, Seibel, S-H.* and Lagnado, L. An amplitude code increases the efficiency of information transmission across a sensory synapse. BioRxiv 328682. Submitted.
* These authors contributed equally to this work.

Part of chapter 5 will be published:

Johnston, J., Seibel, S.-H., Darnet, L.S.A., Renninger, S., Orger, M., and Lagnado, L. (2018). A retinal circuit generating a dynamic predictive code for orientated features. BioRxiv 331504. Submitted

Acknowledgments

I wish to express my gratitude to Professor Leon Lagnado for giving me the opportunity to work on this project.
Thanks to my colleagues for their assistance especially Jamie Johnston, Rozan Vroman and Michaela Fuchs.

I thank Sussex university for providing me the research studentship grant for this work. I am grateful to Hazel Smulder for taking care of my fish and maintaining the fish facility.

I would like to thank the School of Life Science office team, especially Anna Izykowska and my second supervisor, Professor Miguel Maravall for their fantastic support.

Finally, I would like to thank my friends and my family for their incredible support, encouragements and continuous love during these years.

University of Sussex

Lea Darnet ***DPhil***

Strategies to encode information with glutamate release in synapses of the *Danio Rerio* visual system

Abstract

I have used the fluorescent reporter iGlusnFR to observe glutamate release from bipolar cell (BC) terminals onto retinal ganglion cells (RGCs) dendrites and from RGCs outputs in live zebrafish using multiphoton microscopy.

Most neurons in the brain represent information using a digital code: temporal sequences of spikes of fixed amplitude that trigger the quantized release of neurotransmitter. The amplitude distribution of BCs events demonstrated clear quantization, showing that bipolar cells generate multivesicular events *in vivo* to encode visual information. I showed then that the vesicles constituting the events were released in a coordinated fashion and was not described by a Poisson process. It was then possible to understand for the first time how visual information was encoded with a vesicle code. Coding with amplitude was more prevalent in OFF cells than ON cells. Multivesicular events encoded higher contrasts with elevated temporal precision, achieving an accuracy comparable to spikes leaving the retina (about 3 ms). Ribbon synapses therefore discretize their outputs into sequences of numbers ranging from zero up to ~11 enhancing the dynamic range and the temporal accuracy of the vesicle code.

Further, when observing iGluSnFR signals on the dendrites of individual RGCs, multiple individual inputs could be distinguished with varying sensitivity to tuning to spatial orientation. Thus, I used iGluSnFR to understand how visual information was transmitted onto RGCs by comparing inputs from BCs into single RGCs and outputs from the same RGCs in the optic tectum. I used this optical approach to study retinal computations such as dynamic predictive coding. Dynamic predictive coding is computed by RGCs of zebrafish. A combination of excitatory inputs from BCs and inhibitory inputs generate this phenomenon.

Table of contents

List of Figures

Chapter 1

Chapter 2

Chapter 3

Chapter 4

Chapter 5

List of abbreviations

AC	Amacrine cell
AchSnFR	Acetylcholine sensing fluorescent reporter
BC	Bipolar cell
cpGFP	circularly permuted GFP
DPC	Dynamic predictive coding
DPF	Day post fertilization
E_c	Event per cycle
EM	expectation maximization
EOM	Electro optical Modulator
FLIP	fluorescence indicator protein
FRET	Forster Resonance Energy Transfer
GABA	Gamma-Aminobutyric acid
GABASnFR	GABA sensing fluorescent reporter
Gal	Galactose
GECI	Genetically encoded calcium indicator
GFP	Green fluorescent protein
HC	Horizontal cell
iGluSnFR	intensity-based glutamate sensing fluorescent reporter
IPL	Inner plexiform layer
LTD	Long term depression
LTI	Linear Time Invariant system
LTP	Long term potentiation

min	minutes
MLSM	Multiphoton laser scanning microscopy
ms	milliseconds
MVR	Multivesicular release
mW	milliWatt
nL	nanoliter
OPL	Outer plexiform layer
OSI	Orientation selectivity Index
PBP	periplasmic binding protein
PMT	Photo-Multiplier Tube
Q_c	Quanta per cycle
Q_e	Quanta per event
RGC	Retinal ganglion cell
ROI	Region of interest
s	seconds
SF-iGluSnFR	Super Folder intensity-based glutamate sensing fluorescent reporter
SNR	signal to noise ratio
UAS	Upstream activation sequence
μL	microliter
μm	micrometer

Chapter 1

Introduction

1.1. The retinal players in visual transmission

1.1.1. Organization of the retina

The purpose of this thesis is to understand how information is encoded by glutamate release at synapses. To this aim, I studied the synapses of BCs and RGCs in the retina. The retina is a perfect model to understand how sensory information is encoded by synapses due to the anatomy and structure of the retinal neurons have been well studied (Cajal, 1972) (Figure 1.1.), and physiological properties of neurons are well detailed (Adrian and Matthews, 1928; Rodieck, 1965).

Moreover, this piece of the central nervous system tissue is the first place where visual sensations are analysed. The different input neurons (photoreceptors), the intermediary neurons (BCs) and the outputs neurons (the retinal ganglion cells (RGCs)) are identified. Besides, there is almost no feedback from other parts of the brain (but see Esposti et al., 2013). A large amount of visual signal processing already occurs in the retina (Gollisch et Meister, 2010) thanks to the different type of neurons.

The organization of the retina has been extensively described and comprises five types of cells structured in different layers: the photoreceptors, the amacrine cells (ACs), the horizontal cells (HCs), the BCs and the RGCs. The different neuron types are confined in three nuclear layers and the processes and synaptic connections of these cells occur in synaptic laminae, the outer and inner plexiform layers (OPL and IPL) (Figure 1.1.).

Photoreceptors are located in the outer layer in the retina and transduce light into an electrical signal in a graded manner (Arshavsky and Burns, 2012). Two major types of photoreceptors exist; cone photoreceptors, which operate at photopic light levels and participate in colour vision, and rod photoreceptors, which are responsible for scotopic vision. These input neurons depolarize and release glutamate in response to decreases in light intensity and reduce their glutamate release in response to light

increments. The photoreceptors synapse onto two neurons types in the OPL; BCs and HCs (see below). Photoreceptors synapses are arranged as triads. Triad synapses are constituted of a membrane-anchored ribbon at presynaptic sites in the photoreceptor terminals, one to three BC dendrites and two HC processes. Both BC dendrites and HC processes insert into the photoreceptor terminal, forming an invagination. The HC activity lie in close proximity to the ribbon, which is thought to allow them to regulate neurotransmitter release from the photoreceptors to BC dendrites (Dowling, 1970).

The secondary sensory neurons in the retina that convey signals to the next synaptic layer are BCs. These neurons integrate the photoreceptor signal in various ways and establish glutamatergic output synapses onto RGCs as well as ACs interneurons. The BCs form dyad ribbon synapses in the IPL which includes two postsynaptic dendrites from a combination of ACs and RGCs (Figure 1.2.). AC axon terminals form conventional synapses in the IPL, which lack ribbons but contain other synaptic elements, including postsynaptic densities and presynaptic vesicles. Conventional synapses originate from inhibitory, GABAergic or glycinergic ACs synapsing onto BC axons, RGC dendrites, or other AC processes. These synapses are regularly observed in the proximity of ribbon synapses (Dowling 1970). BC output signal are modulated in the IPL by ACs. AC dendrites that appose BC ribbons often make conventional synapses onto the same BC terminal, and thus form a reciprocal synapse. ACs have also conventional synapses that are involved in a feed-forward circuit in the IPL; ACs that are postsynaptic to a BC ribbon synapse form conventional synapses onto RGCs sharing the same ribbon. Thus, while reciprocal synapses monitor RGC responses by modulating their BC inputs, feed-forward terminals shape the electrical properties of the RGC itself (Chen et al., 2010; Grimes, 2012). Lastly, RGCs, which are the last layer of neurons in the retina, send the results of visual information processing to the brain in a spiking code.

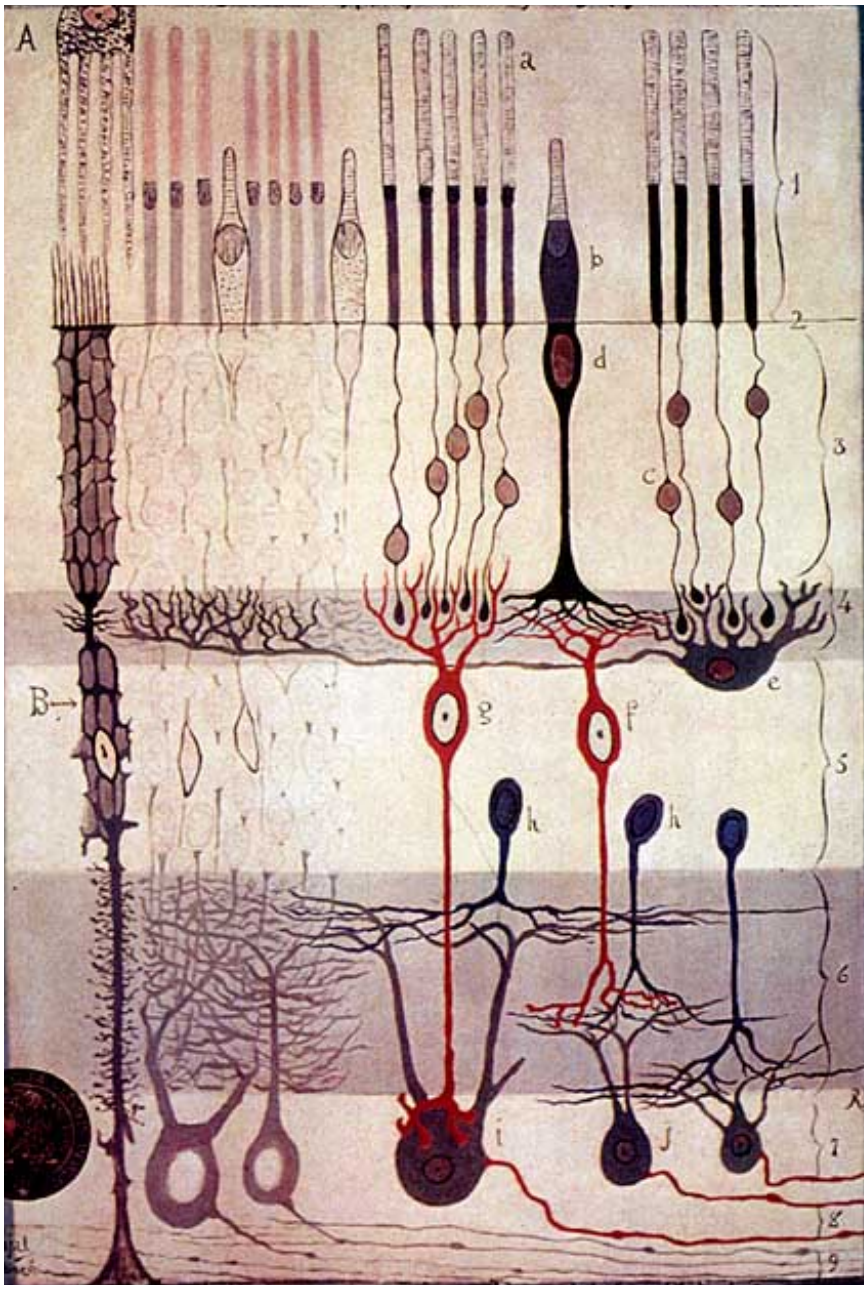

Figure 1.1. Organization of the mammalian retina (from "Structure of the Mammalian Retina" by Santiago Ramon y Cajal (1900).

Outline of the structure of the mammalian retina. 1. Rod and cone layer. 2. External limiting membrane. 3. Outer granular layer. 4. Outer plexiform layer. 5. Inner granular layer. 6. Inner plexiform layer. 7. Ganglion cell layer. 8. Optic nerve fibre layer. 9. Internal limiting membrane. A. Pigmented cells. B. Epithelial cells. a. Rods. b. Cones. c. Rod nucleus. d. Cone Nucleus. e. Large horizontal cell f. Cone-associated BC. g. Rod-associated BC. h. Amacrine cells. i. Giant ganglion cell. j. Small ganglion cells.

1.1.2. Computations in the retina

It has been known for a long time that the retina does not simply convey visual signals that are detected by photoreceptors but rather, carry out a lot of complex computations already before sending out information to the brain. The classical study from Lettvin et al., (1959) shows that the frog retina transmits at least four different operations to the brain such as sustained contrast detection or moving edge detection. These computations are transmitted through different groups of neurons. Later on, numerous computations were found to happen in the retina (Gollisch and Meister, 2010; Baccus, 2007). Here is a summary of retinal computations:

- Contrast adaptation: this is a process that consists in adjusting sensitivity in response to different range of intensities around a mean light. It occurs at the level of phototranduction as well at the level of BCs or RGCs (Nikolaev et al., 2013; Burns and Baylor, 2001; Pugh et al., 1999; Barlow and Levick, 1969; Enroth-Cugell and Lennie, 1975). It affects the sensitivity of the neuron as well as the kinetic of the responses (Smirnakis et al., 1997 ; Baccus and Meister, 2002; Kim and Rieke, 2001; Kim and Rieke, 2003; Rieke, 2001; Chander and Chichilnisky, 2001). When a low contrast switches to a high contrast, RGCs spiking shows a decrease of sensitivity (Baccus and Meister, 2002). The gain of RGCs responses decreases by 25% to 75%. This change of gain can persist for 30 s (Baccus and Meister, 2002).

- Direction selectivity: some RGCs exhibit response selectivity for a specific direction of motion (Barlow et al., 1964; Barlow and Levick, 1965; Vaney and Taylor, 2002). For these cells, the preferred direction produces responses strongly whereas motion in the opposite direction evokes almost no response.

- Orientation selectivity: refers to the selectivity of neuronal firing in presence of elongated visual stimuli oriented along a given axis in the visual environment. When the stimulus is oriented orthogonally to the preferred axis, the responses are suppressed (Hubel and Wiesel, 1974; Antinucci and Hindges, 2018; Antinucci et al., 2016; Johnston et al., 2018).

- Motion anticipation: Changes in light intensity are encoded with delay due to neurotransmission and phototransduction. When an object moves, neural representation of the position of this object always lags behind its real position due to the neuronal delay. The retina can compensate this delay by representing the position of the object in advance of its location (Berry et al., 1999, Johnston and Lagnado, 2015).

- Global motion sensitivity:sSome RGCs named Object Motion Sensitive cells (OMS) are very sensitive to an object that is moving over the background but are suppressed when the background is moving (Olveczky et al., 2003).

- Global Shift suppression: during saccades (fast eyes movements), visual sensitivity to changing stimuli decreases. The retina is able to produce this perceptual suppression (Mackay, 1970).

- Dynamic predictive coding: the statistics of natural scene are not static and correlations between time and space may change. The retina can also adapt to this type of spatial-temporal correlations. In the review of Baccus (2007), the author mentions the following example: trunks in a forest are correlated vertically but not horizontally. However, with closer a look, bark and leaves present a more uncorrelated environment. An efficient encoder of the visual scene would correct to these diverse predictable statistics of the stimulus. Hosoya et al., (2005) showed that RGCs adapt over a few seconds to encode the current visual scene more efficiently. In my last result chapter, I will focus on exploring the mechanisms of dynamic predictive coding in RGCs (see Chapter 5).

1.1.3. Bipolar cells transmit visual information through different channels

Two chapters of my thesis (Chapter 3 and Chapter 4) focus on glutamate neurotransmission in BCs terminals. Hence, I will concentrate the next paragraphs on presenting them.

1.1.3.1. Discovery of bipolar cells

The role of BCs in analysing and decomposing visual information was described extensively in the review of Euler et al., (2014). The name of these cells was coined by a student of Golgi, Tartuferi (Tartuferi, 1887) who described these first projection neurons in the retina, and used the term “bipolar” for the first time. Bipolar refers to the fact that these cells have two protrusions: one that goes up to the OPL layer and one that goes down to the IPL. These protrusions underline the particularity of these cells: they form a third layer in the visual system that relays the sensory neurons (photoreceptors) to the output neurons of the retina, the RGCs. Thus, this unusual peripheral layer of neurons is the first layer to perform computational operations in the visual system and all the visual signals go through the BCs.

1.1.3.2. Physiology of bipolar cells

BCs transfer visual signals via different channels such as polarity (ON-OFF channel), temporality (two distinct temporal filters have been known for decades: transient or sustained BCs) or chromatic composition. In teleosts, there are approximately 20 types of BCs, which stratify in different layers (Connaughton et al., 2004; Connaughton, 2011). A cell type can stratify in different strata of the IPL. There are more OFF types in teleosts (compared to mammals where the ON type represents the majority of BCs).

The differences between OFF and ON cells is established at the level of the OPL. First, a difference of receptors expression at the level of the dendrites of the BCs mediate these polarizing mechanisms. OFF BCs have sign preserving ionotropic receptors (Regus-Leidig and Brandstätter, 2012) such as AMPA, kainate receptors or both, whereas ON cells have sign inverting metabotropic receptor mediated mechanisms (Koike et al., 2010). However, there are differences between ON cells

at the level of the intracellular cascade. Several proteins regulate the activity of G protein for instance (Sulaiman et al., 2013; Rampino and Nawy, 2011; Sulaiman et al., 2010; (De Sevilla Müller et al., 2013). Some of these molecular factors have been shown to impact the kinetics of signalling of ON cells. Another difference between ON and OFF cells is the cone-contact morphology. ON BCs have an invaginating contact (they extend into the synaptic cleft). OFF cells establish a flat contact (they contact the base of the cone pedicle). Whether it affects the delay between ON and OFF channels remains under debate.

Sensory neurons such as photoreceptors and hair cells in the cochlea transmit signals (both visual or sound signals) that can differ by several orders of magnitude in intensity. This kind of information is thought to be encoded in a graded manner. Graded synaptic outputs require a large pool of vesicles (hundred to several thousands) to support continuous vesicle release. To obtain this level of transmission, these sensory neurons have a particular chemical synapse: the ribbon synapse. Interestingly, the BCs have ribbon synapses as well (Figure 1.2.). Moreover, recent studies showed that BCs in several species not only transmit signals in a graded manner but can also generate spikes (Dreosti et al., 2011; Saszik and DeVries, 2012) (spikes were reported in hair cells as well). These spikes were shown to encode light signals, challenging the traditional view of BCs that were thought to encode information only in a graded manner. The fact that BCs can encode information in both a graded and digital manner raises the question about the role of the structure of their ribbon synapses in processing information.

Ribbon synapses have a very specific structure that was studied using electron microscopy (Sjostrand, 1953; Sjostrand, 1958). Briefly, the ribbon synapse is composed of an arciform density (containing proteins such as Ca^{2+} channels) and the ribbon structure (including the proteins ribeye and piccolo for instance). The number of ribbons varies per BC type. There are approximately 30 to 50 ribbons per axon terminal in sustained BCs whereas there are around 100 ribbons in transient BCs depending on the specie. These ribbons are thought to support vesicle release.

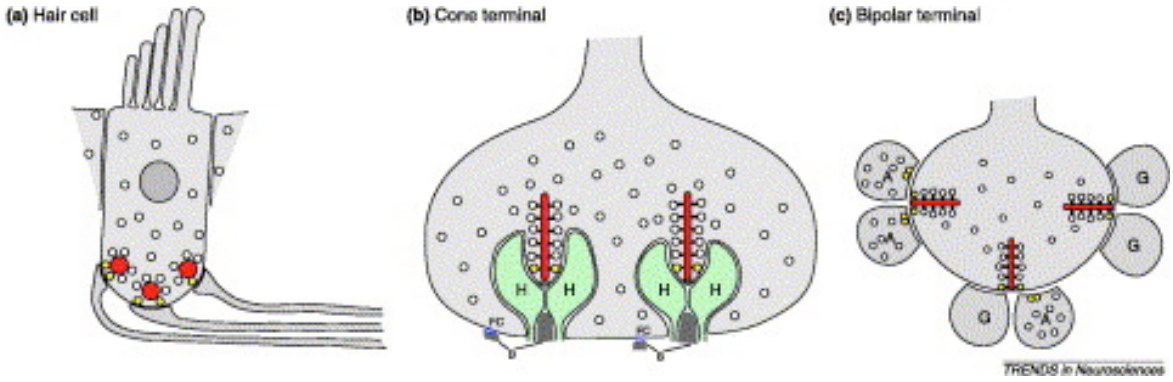

Figure 1.2. Examples of ribbon synapses in sensory systems (adapted from Sterling and Matthews, 2005).

(A) Hair cells. A hair cell can contain from 10 to 20 ribbons. Ribbons are tethering several vesicles.

(B) Photoreceptors. Each cone has between 20 and 50 ribbons. The ribbons are located at an apex of an invagination. It forms a triade with three other processes: two Horizontal cells and one bipolar cell.

(C) BCs. Each ribbon constitutes a dyad with two postsynaptic neurons: two RGC dendrites, two AC processes or one RGC dendrite and one AC process.

1.1.3.3. Computations at bipolar cell synapses

A lot of studies on BCs used electrophysiology techniques and are based on recordings from the soma of the cells. However, Leon Lagnado's laboratory developed a calcium reporter targeted at the synapse to study computations in BCs (Dreosti et al., 2009). Several publications indicated then that complex computations already occur in BCs terminals. For instance, Odermatt et al. (2012) showed that BCs synapses were encoding luminance and contrast in both a nonlinear and linear fashion. Moreover, Nikolaev et al., (2013) in an *in vivo* study, revealed that these terminals could adjust their responses after an increase of the temporal contrast of the visual stimulus. A study done by Rosa et al., (2016) demonstrates that the first compartment tuned to low frequencies was the terminals of the BCs. Interestingly, in the article of Baden et al., (2014) show that the volume of the synapse participates to different temporal filters.

1.2. Ribbon synapses in the retina are key to the encoding of visual information

1.2.1. Pools of vesicles at the ribbon synapse

Several vesicle pools have been described at ribbon synapses, which can be distinguished by their kinetics. The number of vesicles that are released was measured in OFF BCs of turtles and rodents with a rate of 20 vesicles per second (Ashmore and Copenhagen, 1983; Berntson and Taylor, 2003). The plasma membrane at the active zone is defined as an ultrastructural and functionally specialized area of the presynaptic terminal where vesicles fuse (Rudolph et al., 2015). The vesicles docked at the active zone represent the ready releasable pool

(20% of the total number of vesicles available) (Mennerick and Matthews, 1996), which is immediately available for release after stimulation (Figure 1.3.).

The reserve pool (80 %) contains the vesicles released over several hundred of milliseconds (Lagnado et al., 1996) (Figure 1.3.). This pool contains the vesicles tethered at higher rows of the ribbons. After this phase, a large number of vesicles maintains a continuous release thanks to the reserve pool.

Another pool exists, the recycling pool, which has been shown to be released at very high stimulation frequencies in different species such as Drosophila (Delgado et al., 2000; Richards et al., 2000; Heuser and Reese, 1973; Kuromi and Kidokoro, 2000). Several studies suggest that this pool is mobilized after the recruitment of the reserve pool. Moreover, some BCs studies suggest that these vesicles are not recruited during physiological activity (they could be recruited only because of a strong stimulation) (Holt et al., 2004; Lagnado et al., 1996).

Vesicles that are docked at the plasma membrane are released at ribbon synapses thanks to L-type calcium channels ($Ca_V1.4$) that contain the calcium channel subunit1αF, which constitutes a particularity of ribbon synapses in the retina (Morgans, 2001). Electron microscopy observations showed that these channels are highly correlated in space with the synaptic ribbons. They are located along the docking sites of the vesicles, allowing vesicle fusion to be triggered by low levels of calcium.

Numerous roles of the ribbons have been suggested. The ribbon has been suggested to act as a calcium buffer, like a safety belt for vesicles, a device for compound fusion with other vesicles and ribbons were thought to take part in multiple vesicle release (reviewed in LoGiudice and Matthews, 2009). Graded signaling is possible thanks to large terminals that contain several thousands of vesicles with several active zones. Each active zone contains a ribbon with a lot of vesicles tethered near the fusion site (Baden et al., 2013), allowing continuous vesicle release. Another mode of information transmission is the digital mode (this second

mode of vesicle release is closer from conventional synapses). A Ca^{2+} spike can trigger the release of more than 20 vesicles at one active zone. These vesicles form a ‘rapidly releasable pool’ (RRP) (Baden et al., 2013) (Figure 1.3.). This digital mode permits high temporal precision (Baden et al., 2011; Saszik and DeVries, 2012) of neuronal responses.

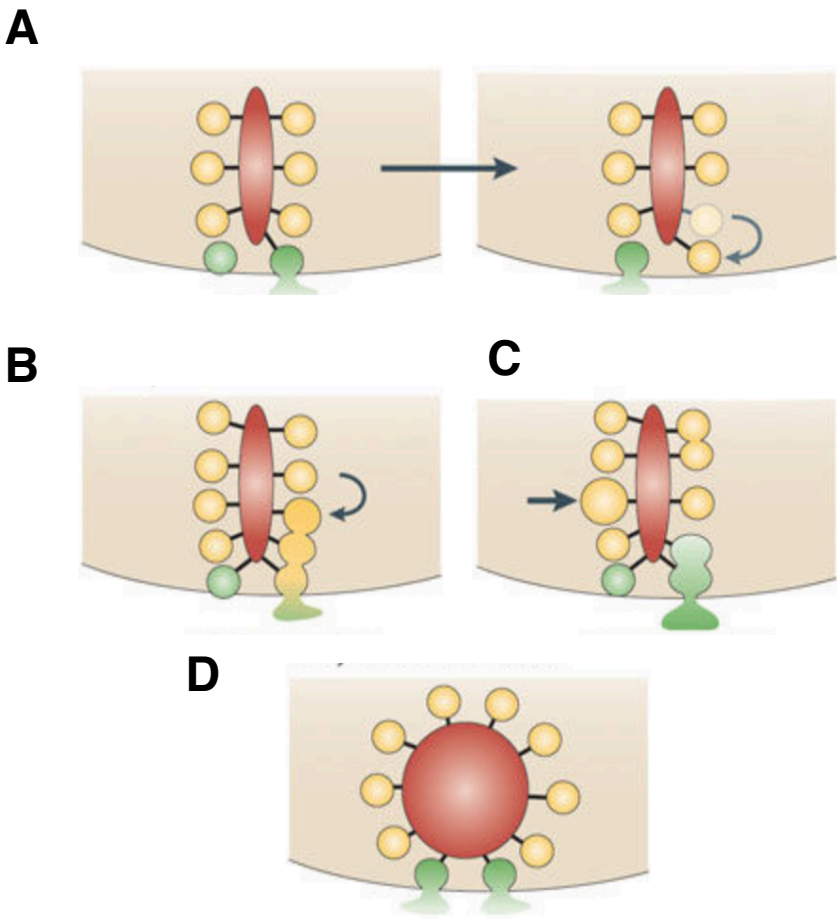

Figure 1.3. Different roles of ribbon synapses. (Adapted from (Matthews and Fuchs, 2010).

(A) Progressive fusion: Fusion that occurs during a maintained depolarization; generating independent unitary events.

(B) Sequential compound fusion: vesicles that are located at the base of the ribbon fuse first with the plasma membrane. They fuse then with the vesicles at the upper row.

(C) Homotypic compound fusion: vesicles fuse together before fusing with the plasma membrane.

(D) Synchronized fusion: fusion of multiple docked vesicles which can generate MVR.

The green vesicles represent the vesicles that are fusing from the ready releasable pool.

The yellow vesicles represent the vesicles from the reserve pool.

1.2.2. Multivesicular release at ribbon synapses

The mechanisms underlying vesicle release still remain a matter of debate. A tenet of vesicle release used to be that a maximum of one vesicle can be released per stimulation (Redman, 1990, Korn et al., 1994). This is the one-site-one-vesicle hypothesis. Several evidences support this hypothesis. Korn et al., (1982) observed that the number of quanta in Mauthner cells released after stimulation has been shown to be equal to the number of release sites available. Moreover, Schikorski and Stevens, (1997) observed that a single hippocampal bouton released at most one quantum of transmitter per response. However, some ribbon synapses have the ability to release multiple vesicles at the same time. This phenomenon is named multivesicular release (MVR). More precisely, MVR is the release of more than one vesicle per active zone in response to a presynaptic action potential in a coordinated manner (Rudolph et al., 2015). The first evidence showing this phenomenon at ribbon synapses was found in cochlear hair cells where multiquantal release occurs from single presynaptic active zones (Glowatzki and Fuchs, 2002). The authors of the study performed whole-cell, recording of postsynaptic currents from afferent fibers in contact with inner hair cells of rat cochlea. The responses recorded presented a large range of amplitudes, suggesting MVR. The idea that the release of several vesicles quasi simultaneously was coordinated results from the distribution of the EPSC intervals. These intervals were not described by a Poisson process. This indicated that the responses could not be generated by the stochastic release of single vesicles but rather by a coordinated release of a variable number of vesicles. In BCs, one study has shown MVR (Singer et al., 2004). One of the major lack of understanding in multiple vesicular release are the mechanisms that underlie this phenomenon. How is this coordinated release mediated?

Several processes could explain the synchronized release of multiple vesicles. There are three main models of vesicle fusion. In the model of synchronized fusion (Figure 1.3.D.), the vesicles that are tethered to the ribbon move towards the plasma

membrane in an active or passive manner to replace the ones that are released at the base of the ribbon. Another possibility consists in the fusion of several vesicles on the ribbon: this is the compound fusion hypothesis. Compound fusion could follow two different scenarios. Sequential fusion could happen when the vesicles at the base of the ribbon partially fuse. The other vesicles at higher rows could then partially fuse, releasing glutamate through the vesicles that have already fused (sequential fusion, Figure 1.3.B, Figure 1.4.). This type of fusion could explain why in frog hair cells, a short depolarization causes the release of many more vesicles than the number docked at the membrane (Edmonds et al., 2004). The other scenario that has been suggested involves the fusion of vesicles prior to the fusion to the plasma membrane (homotypic fusion, Figure 1.3.C.). This hypothesis has been supported by electron microscopy that revealed the presence of larger vesicles tethered to the ribbon after stimulation (Matthews and Sterling, 2008). In the case of BCs, the results of Singer et al. (2004) were interpreted as synchronous release but could also be explained by neurotransmitter release from pre-fused vesicles.

Definitive evidence for compound exocytosis is still lacking and different possibilities could occur in different proportions. One way to better understand the synaptic release of neurotransmitter at ribbon synapses is to measure the neurotransmitter release directly at the synaptic cleft such as monitoring glutamate release *in vivo*. This is what I studied in Chapter 3 and Chapter 4 of this thesis.

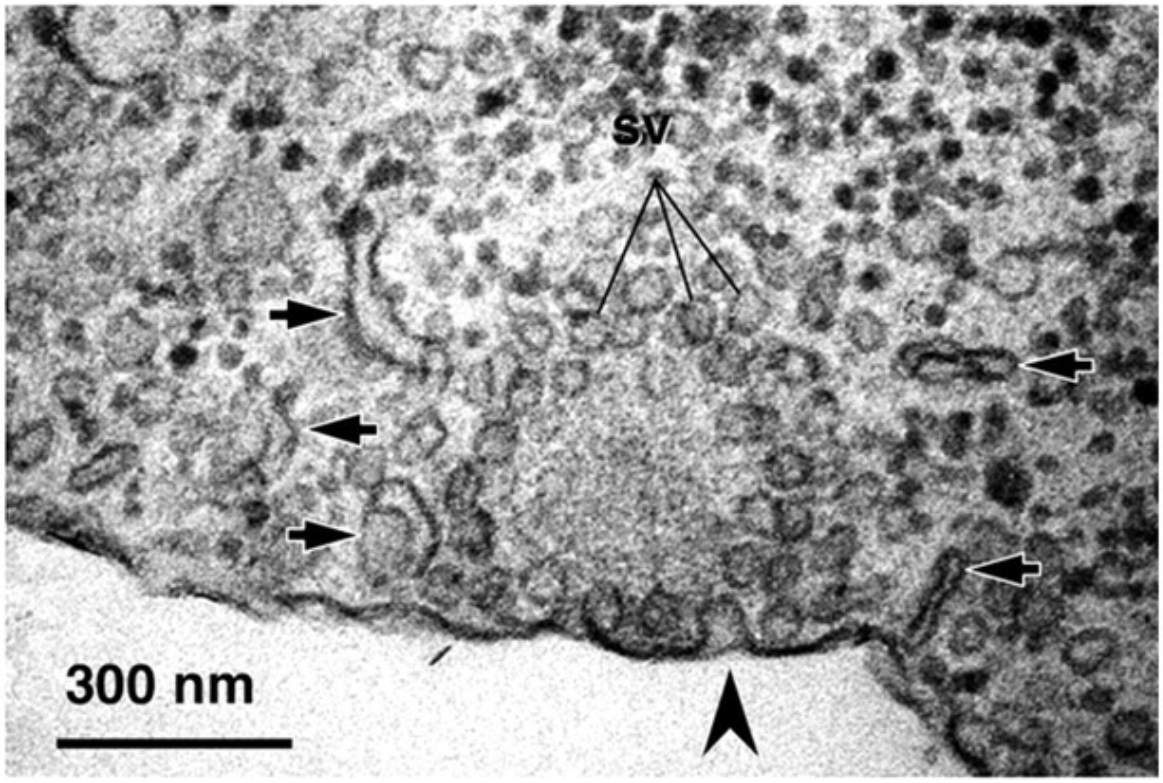

Figure 1.4. Electron micrograph of bipolar cell ribbon synapse (Wu et al., 2007)**.**

R: ribbon

SV= synaptic vesicles

The arrows indicate large compounds that could result from vesicles that fused together. The larger arrow indicates a vesicle fusing with the membrane or a retrieval of a vesicle at the active zone.

1.3. Neural coding in the inner retina

1.3.1. Different types of coding in the retina

Numerous studies have used electrophysiological methods to understand how neurons encode information. Neurons can generate different patterns in response to a stimulus such as spikes, burst or graded signals. Here are different features that contribute to encode visual information in the retina:

- Event rate (or rate code): the neural response to a stimulus, is fully described by the probability distribution of spike rate as a function of the stimulus. This probability distribution can be computed from the time-dependent firing rate r(*t*). r(*t*) includes all the information about the stimulus that can be obtained from the spike train. Two type of rate codes can be defined. The case where the generation of each spike is independent of each other is named independent-spike code. The case where the spikes are not independent from each other is named correlation code. The correlations between spikes can contain additional information about the stimulus (Dayan, 2005). Usually, information is carried by these two types of rate code.

-Analogue signalling: Photoreceptors in the retina detect the light and convert the visual information into graded changes in their membrane potential (reviewed in Heidelberger, 2007). Synapses in the photoreceptors transfer such analogue signals to postsynaptic cells by continuously releasing neurotransmitters according to current light intensity and recent stimulus history. However, depending on the size of a postsynaptic neuron, the ability to faithfully pass a graded input from the dendrite to the axon terminals may be limited by passive cable properties. Hence, the transmission of the signal through several neurons with this mechanism becomes weaker and weaker and some noise may be added to this signal too. On the other hand, converting these analogue signals into digital signals (action potentials or spikes) transfers information via regenerative processes (reviewed by Baden et al., 2013). However, the disadvantage of this digital mode is that some visual information

will be lost.

-Population coding: the simultaneous activity of a large set of neurons can represent information about the stimulus (Squire, 2009). This type of information encoding increases the organism's certainty as well as encoding different aspects together. One of the main characteristics of the population coding is the stochastic nature of the neuronal responses: when a stimulus is presented several times the response of a neuron and more generally form a group of neurons will be often different time to time. One of the consequences is that different stimuli can trigger the same population response with different probabilities.

-Temporal coding: Some studies emphasise that neural circuits can operate by RGCs responses containing only a few spikes or a single action potential. First, for some visual guided behaviours, the integration time is no longer than 50 ms , during which neuron responses could consists only a few spikes (Meister and Berry, 1999). Second, there is a study which demonstrated that the retina was continuously scanning the image with miniature eyes movements (Skavenski et al., 1979). Therefore, each RGC is activated for about 20 ms by light from a single point in a space. Third, the spikes that the RGS are generating can be precisely timed and these responses can be highly reliable: the temporal jitter of RGCs can be as short as 3 ms (Berry et al., 1997). However, the number of spikes can be variable trial to trial (Berry et al., 1997; Berry and Meister, 1998). This means that individual responses are highly significant and responses that contains a different number of spikes can reliably represent different features of a visual message.

-vesicle coding: as explained above, the spike code has been explored in detail but the vesicle code is not understood as well. Some neurons can release several vesicles at the same time by MVR. Therefore, some neurons can produce responses with different amplitudes and encode information with more units of coding: 1, 2, .., n vesicles per events than spike-coding with a set amplitude. In this thesis, I studied this neural code *in vivo* in bipolar cells. This type of encoding might considerably increase the capacity of information coding. Numerous studies tried to measure *in*

vivo the release of vesicles (especially from glutamate). This is discussed in the next section.

1.3.2. Towards a method of measuring glutamate release

Various methods have been used to measure extracellular glutamate concentration such as *in situ* microdialysis or readout of enzymes associated with glutamate production by coupling a second readout such as NADH fluorescence or a microelectrode current to glutamate oxygenase or glutamate dehydrogenase. All these methods lack temporal precision and have a poor signal to noise ratio (Marvin et al., 2013). Fluorescent reporters have many benefits. They provide a direct readout of glutamate and may have a better spatial and temporal resolution.

Thus, several attempts have been made to develop glutamate sensors such as Glutamate (E) optical sensor (EOS) based on a modified AMPA receptor fused with an Oregon green dye (Namiki et al., 2007). However, no cell specificity is possible with this probe and the low dissociation kinetics may be a problem when studying the late behaviour of neurotransmitter release. Other glutamate reporters have been developed.

Genetically encoded indicators can be expressed in specific cell-types with non-invasive techniques (transgenesis or viral transfection). Among the promising candidates for the development of glutamate sensors are the Bacterial periplasmic binding proteins (PBPs) (Marvin et al., 2013). *Escherichia coli gltI* encodes the periplasmic component of the ABC transporter complex for glutamate and aspartate. For instance, *glt1* was a scaffold for the genetically encoded probe glutamate-sensing fluorescent reporter glusnfr, the more sensitive variant SuperGlusnfr or the fluorescence indicator protein for glutamate (FLIP) using Förster Resonance Energy Transfer (FRET). Nonetheless, these methods lack sensitivity due to low signal to noise ratio (Okumoto et al., 2005; Hires et al., 2008).

Recently, a report described an intensity-based glutamate-sensing fluorescent

reporter (iGluSnFR) based on *glt* (Marvin et al., 2013). The authors attached a circularly permutated GFP (cpGFP) to the glutamate transporter. In the absence of glutamate, a domain close to the chromophore is distorted, resulting in low fluorescence of the cpGFP. When glutamate binds to the transporter, the correct configuration of cpGFP is restored, eliciting a brighter fluorescence (Figure 1.5.). This new probe has a lot of advantages: it can be targeted to particular cell types, the signal to noise ratio is improved allowing the detection of glutamate transient with high spatial resolution.

New iGluSnFR variants have been developed (Helassa et al., 2017; Marvin et al., 2017) They offer different improvements compared to the original version. SF-iGluSnFR has the circularly permuted GFP replaced with the circularly permuted super folder GFP (Pédelacq et al., 2006). This allows a faster maturation of the reporter. It facilitates the exportation of the reporter from the endoplasmic reticulum, leading to an increase in the expression level of the protein.

Moreover, the researchers introduced mutations in SF-iGluSnFR to modify its affinity and kinetics. The new variants can have an affinity up to eight times higher than the original version of iGluSnFR. Concerning the kinetics, one of the variants (S72) has a half–decay of 8 ms. Variants for chromatically different sensors are developed in this study. These variants led to functional yellow or blue versions (SF-Venus iGluSnFR or SF-Azurite respectively).

Another study (Helassa et al., 2017) introduced ultra-fast variants of iGluSnFR. One of the variants developed in this study, $iGlu_u$ has kinetics five-fold faster than the original iGluSnFR and present higher dissociation rate as well (six-fold faster dissociation rate).

Hence iGluSnFR has become a popular tool and different versions were created to respond to different need: targeting different cell type, increase the temporal resolution or brighten signal by increasing affinity of the reporter to work with iGluSnFR.

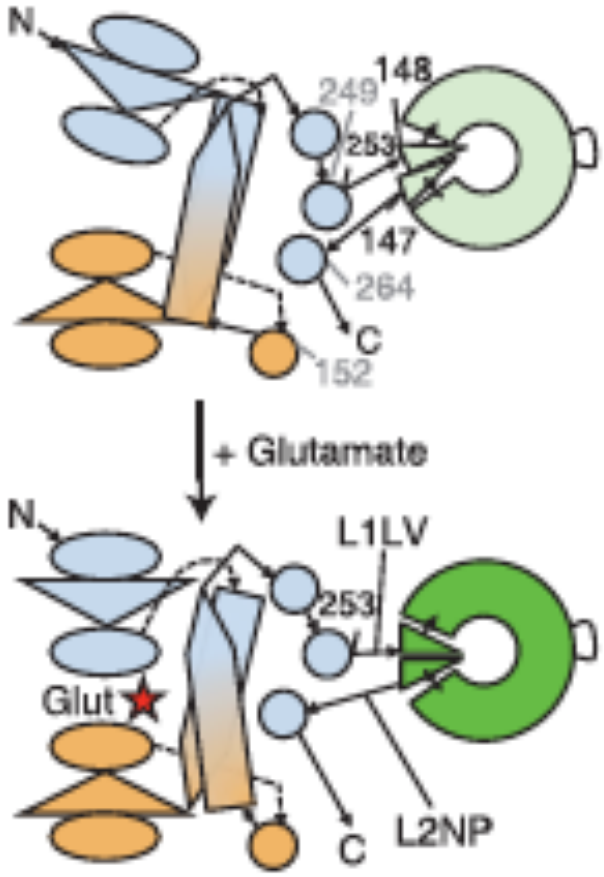

Figure 1.5. Schema of the extracellular domain of IGluSnFR. (Adapted from Marvin et al., 2013) The extracellular domain is composed of a glutamate binding domain and a circular permuted Green Fluorescent Protein (GFP). When a molecule of glutamate binds to IGluSnFR, a change of coformation of the cGFP happens and the cGFP emits some fluorescence.

1.4. Aims of the thesis

The aim of my PhD project is to study how synapses contribute to information computations. I used iGluSnFR or SF-iGluSnFR probes in combination with multiphoton imaging to study glutamate release in BCs synapses. For the first time, glutamate release from BCs and glutamate inputs onto RGCs can be observed *in vivo*. My research provides new insights on how BCs encode visual information with vesicles of glutamate: BCs are generating MVR in vivo in response to a visual stimulus. They encode visual information with MVR and event rate. Another possible application of iGluSnFR in the retina is analysing the wiring of BCs onto RGCs. Recently, the laboratory showed that 25% of BC terminals display orientation selectivity. Thus, using iGluSnFR, it is possible to look at single RGCs receiving different inputs from orientation selective BCs and to compare this with the outputs of the same RGCs in the optic tectum to understand how BC orientation selectivity influences orientation selectivity of the RGCs. I took advantage of this to understand how the retinal computation of dynamic predictive coding was encoded in RGCs by comparing the inputs and the outputs of the RGCs and by testing how inhibition from ACs was involved.

Chapter 2

Methods

2.1. Expressing iGluSnFR in the retina

2.1.1. Animal and housing

All animal procedures were performed in accordance with the Animal Act 1986 and were approved by the Home Office. Experiments were carried out in pigmentless (nacre-/-, roy-/-) zebrafish (*Danio rerio*) larvae (from 7 days post fertilization (dpf) to 9 dpf). I used two lines for glutamate recording in BCs, *Tg*(*ribeyeA:Gal4,UAS:iGluSnFR)* and *Tg*(*ribeyeA:nlsTrpR,tUAS:SF-iGluSnFR). Tg*(*ribeyeA:Gal4,UAS:iGluSnFR)* was generated by crossing an iGluSnFR reporter line *Tg(UAS:iGluSnFR*) and a BC driver *line Tg(ribeyeA:Gal4*). I generated an improved iGluSnFR expression line (see comments next page), *Tg*(*ribeyeA:nlsTrpR,tUAS:SF-iGluSnFR),* by co-injecting plasmids ribeyeA:nlsTrpR and tUAS:SF-iGluSnFR. RGC experiments were made by injecting plasmids elavl3:HucKalTA4 in the transgenic fish *Tg(UAS:iGluSnFR)*.

Fish larvae were raised in E2 medium with 1-phenyl-2-thiourea (200 μM, Sigma Aldrich, Dorset, UK) in an incubator at 28 degrees with a daily light cycle of 9 hours darkness and 15 hours light.

Representative sparse labellings of BCs by iGluSnFR or SF-iGluSnFR with the UAS/Gal4 (Asakawa and Kawakami, 2008) or TrpR/tUAS (Suli et al., 2014) system, respectively, are shown in Figure 2.1.

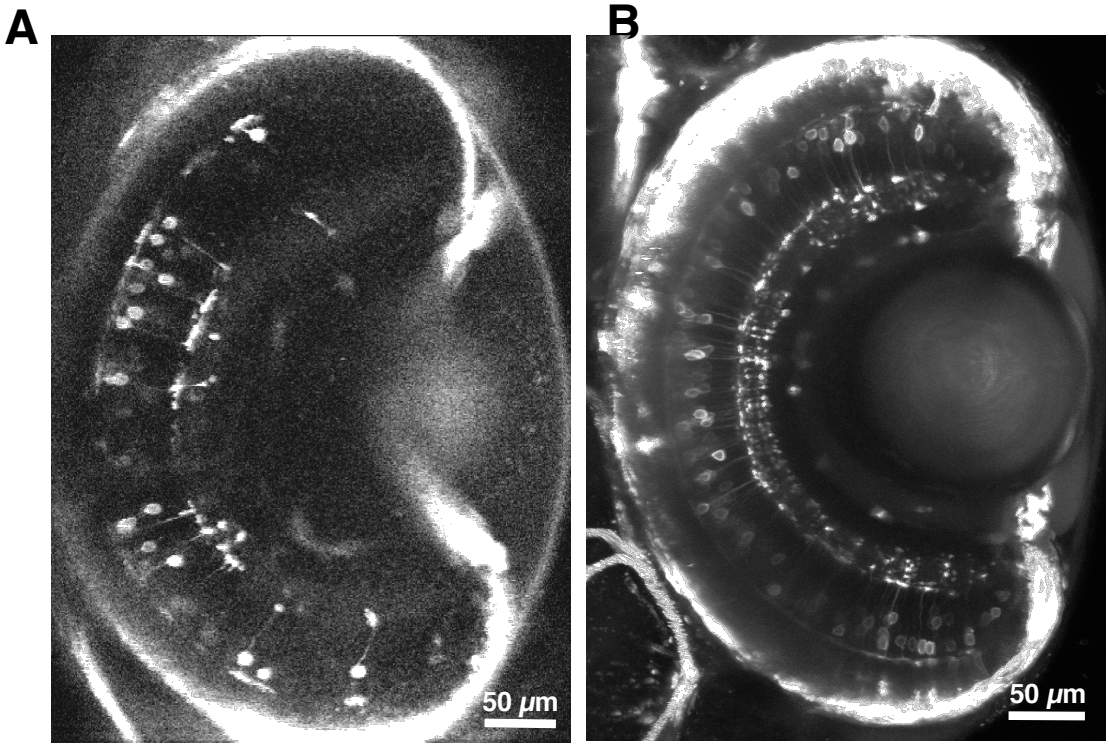

Figure 2.1. Expression of SF-iGluSnFR or iGluSnFR in zebrafish retina.

(A) Expression of iGluSnFR in *Tg(RibeyeA:Gal4,UAS:iGluSnFR)* at 6 dpf in the retina.

(B) Expression of SFi-GluSnFR in *Tg(RibeyeA:TrpR,tUAS:SF-iGluSnFR)* at 7 dpf in the retina.

First, I used the UAS/Gal4 system to perform my experiments. However, this system has several drawbacks due to the methylation of the UAS sequences, which causes silencing of reporter expression. This is known to be a defence mechanism system in organisms: it has been shown that aberrant methylation of gene was implicated in tumours development (Feinberg and Vogelstein, 1983) (Feinberg et al., 2006). The mechanisms underlying this phenomenon are not well understood, but it is known that repetitive sequences of DNA can trigger this methylation (Garrick et al., 1998). The plasmid that was used to create the line UAS contained 10 repetitions of UAS DNA sequence. These repetitions are prone to CpG methylation that causes silencing (Akitake et al., 2011). This silencing continues to occur throughout larval development so that the expression of iGluSnFR was severely reduced on fish older than 8 dpf. Moreover, my recordings often suffered from photobleaching, which may have been due to the lower expression level of iGluSnFR. In addition, it is known that UAS silencing increases over passage of fish line (Akitake et al., 2011; Goll et al., 2009), such that generation of a new fish line is often necessary or lines have to be carefully maintained by screening progeny for stronger expression.

I therefore generated a new fish line using the system TrpR/tUAS (Suli et al., 2014) with a newer version of iGluSnFR, SF-iGluSNFR (SuperFolder iGluSnFR) (Marvin et al., 2017). The variant SF-iGluSnFR exhibits the same kinetics as iGluSnFR in cultured rat primary neurons (data from Lagnado's laboratory). TrpR/tUAS was developed by using tryptophan repressor in *Escherichia coli*. The tUAS DNA sequence does not have methylation sites which allows the expression of the transgene to be maintained over several generations. SF-iGluSnFR is a variant that has a mutation in the circulating GFP DNA. This modified GFP has the property to fold faster than iGluSnFR and thus matures faster. This increases the expression of the protein at the membrane. With this variant, photobleaching problems were drastically improved, which allowed me to record as long as 45 min (with the Gal4/UAS system, iGluSnFR signal was photobleached within 10 min). I obtained several transgenic lines with this system; some lines display sparse labelling

("patchy" labelling that results in single cells labelling) and one line has labelling in almost all BCs, which was not possible with the UAS/Gal4 system. In this thesis, all the data from chapter 3 were obtained with IGluSnFR whereas 94% of the data from chapter 4 were obtained with SF-iGluSnFR. All the data from chapter 5 were acquired with SF-iGluSnFR.

2.1.2. Sparse labelling in the retina (Chapter 5)

One-cell-stage eggs from *Tg(UAS-iGluSnFR)* fish were injected with 15 ng/µl plasmid DNA encoding KalTA4 (Asakawa et al., 2008; Distel et al., 2009) under the control of the pan-neuronal *elavl3*/*HuC* promoter (*elavl3:HucKalTA4)* together with 14 ng/µl *Tol2* transposase mRNA diluted in Millipore water with 0.025% phenol red. *Tol2* sequences flanking the expression cassettes in the plasmids allowed for stable genomic integration.

2.2. Two-photon iGluSnFR imaging in zebrafish retina

2.2.1 Two-photon microscopy

Multiphoton laser scanning microscopy (MLSM) is an impressive apparatus that combines long wavelength multiphoton fluorescence excitation with laser scanning microscopy. This facilitates imaging of neurons deep in living tissue with high spatial resolution and minimal photodamage (Denk et al., 1990; Denk and Svoboda, 1997).

In one-photon microscopy, such as confocal microscopy, the fluorophores of the samples are excited by a single photon and return to their initial state by emitting a photon with a wavelength determined by the energy difference between the "excited" and "ground" states. Two-photon microscopy is based on exiting the fluorophore by absorption of two photons instead of one. When two photons arrive at the level of the fluorophore quasi-simultaneously, their energy is added and can excite the fluorophore. Therefore, a fluorophore that is excited by one blue/green photon (for

conventional microscopy) will be excited by two infrared photons. Two-photon microscopy requires high intensity light because of the necessity for two photons to arrive at the same time (Figure 2.2.). This is achieved by using pulsed lasers.

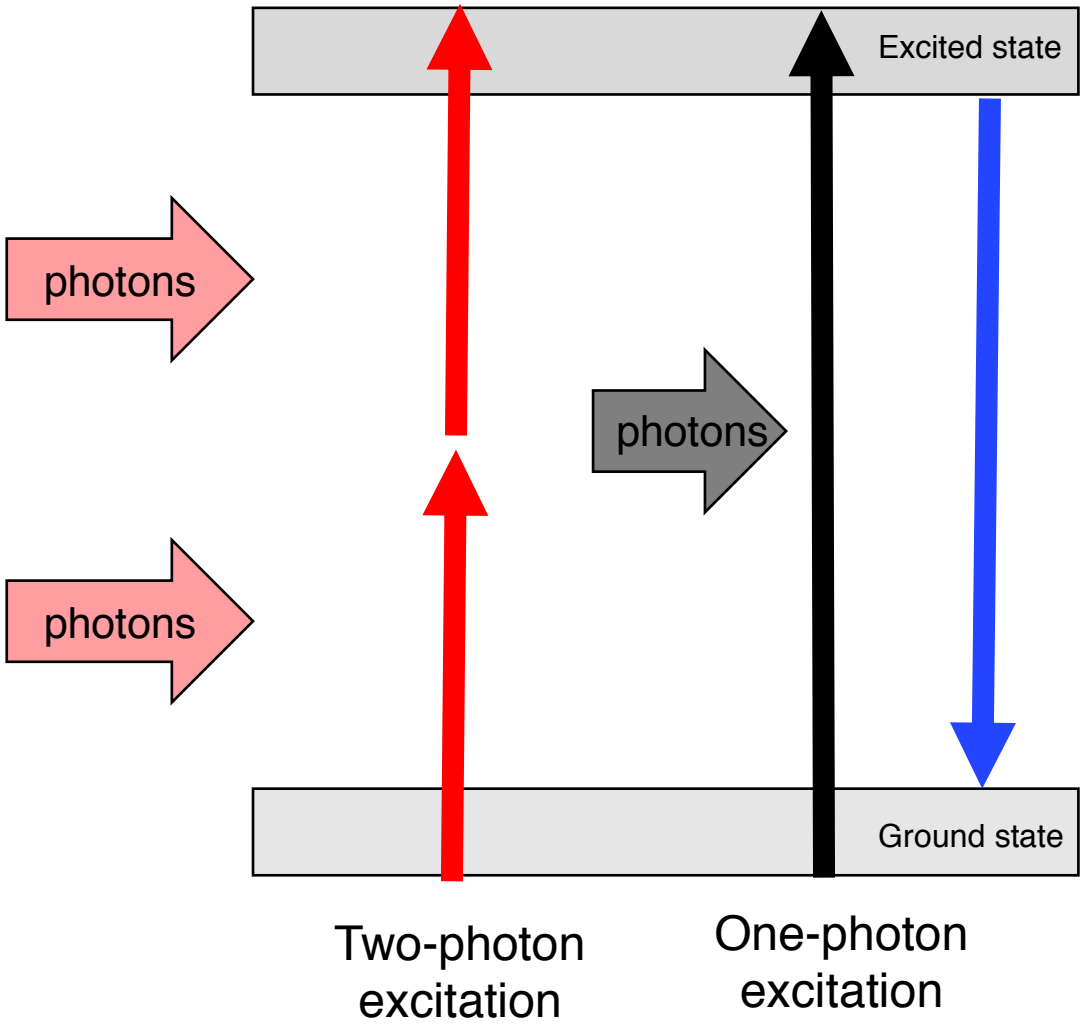

Figure 2.2. The principles of two-photon excitation: Jablonski energy diagram.
In one photon microscopy, the fluorophore is excited by a single photon, relaxes and emits a photon. Two-photon microscopy relies on the concept of two photon absorption. Two-photon absorption is the notion that two photons can excite a molecule from one energy state (the ground state) to a higher energy state (excited state) in a single quantum event. This state of the fluorophore can be described physically as the jump of an electron from one atomic orbital to another that is less stable. The energy difference between the two states is equal to the sum of the energies of the two-photon absorbed. Afterwards, the electron returns to its stable state. Through this process, the electron releases a photon with less energy than the excitation photon. During my experiments, I used iGluSnFR or SF-iGluSnFR that both contain a GFP. This fluorescent dye has an excitation spectrum in the 400-500 nm range. Therefore, the wavelength I used to excite this dye with a multiphoton microscope was 940 nm (in the infrared spectrum).

Multiphoton microscopy is more light-efficient than conventional microscopy (confocal). There is reduced photobleaching because the photon density required for two-photon excitation is achieved with a focal volume of 1–2 μm in diameter (Denk, 1994) (Figure 2.3.B.). This small volume of excitation made it possible to record retinal neuron activity without activation of photoreceptors by the scanning laser. Once the excitation is accomplished, there is no need to use a spatial selection of the photons, such as a pinhole in confocal microscopy (Figure 2.3.A.). Hence, more photons are detected with multiphoton microscopy and a deeper penetration of the tissue is possible (up to 1.6 mm for two-photon microscopy compared with 200 μm for confocal microscopy) (Kobat et al., 2011). Moreover, since detection of fluorophore light is possible with lower excitation intensity (infrared light), there is less phototoxicity associated with multiphoton microscopy.

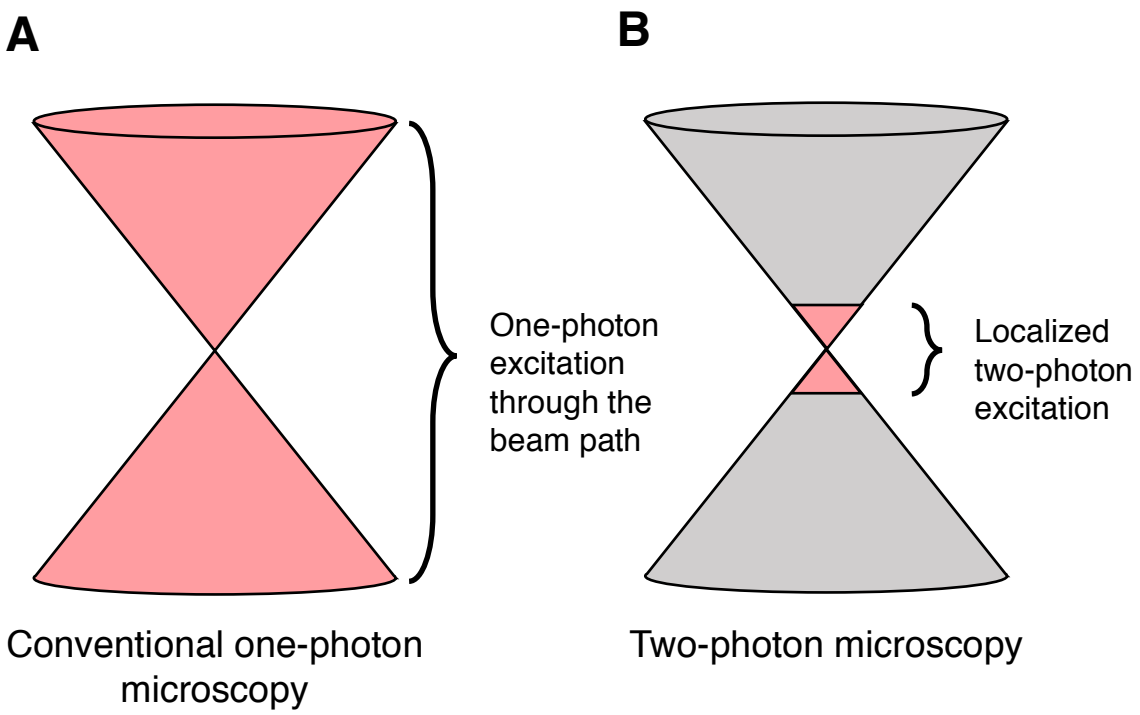

Figure 2.3. Two-photon excitation is confined to a small volume of excitation.

(A) In one-photon fluorescence microscopy, one photon will excite the fluorophore. These events happen through the laser beam (it forms a cone of excitation).

(B) Concerning two-photon microscopy, two photons are needed to excite the fluorophore. This event is extremely rare since it can only happen where there is a very high photon density. In two-photon microscopy, excitation is confined to a small focal volume (1 μm^3). Hence the excitation occurs only in the focal plane. As a result, this decreases considerably the photodamage and photobleaching of the sample. Another advantage is that the signal-to-noise ratio of the recording is increased.

Sample mounting, detection, and recordings were performed as described below (Figure 2.4.). Fish were immobilized in 3% low melting point agarose (Biogene, Kimbolton, U.K.). To avoid eye movements, the ocular muscles of each larva were paralyzed by injection of 1 nL of α-bungarotoxin (2 mg/mL, Sigma) behind one eye. α-bungarotoxin is a neurotoxin that blocks muscle movements. Fish were then placed inside the microscope with one eye pointing at a LED or at a screen (Figure 2.4.B. and Figure 2.4.C., respectively). BCs and RGCs were imaged *in vivo* using a Scientifica two-photon microscope (Scientifica, Uckfield, U.K.) equipped with a mode-locked Chameleon titanium–sapphire laser tuned to 915 nm (Coherent Inc., Santa Clara, CA, U.S.A.). The laser of the two-photon system is a pulsed femtosecond infrared laser that uses Ti:sapphire as the gain medium, pumped by a 10 W Diode: this is a laser with a pulse length of about 100 femtoseconds and repletion rate of 100 MHz. A shutter blocks the laser beam when no pictures are taken. The laser beam is then projected onto a lens system by piezo-controlled scanning mirrors. A tube lens projects the beam into the back aperture of an Olympus XLUMPLFLN 20X water immersion objective (NA 0.95, Olympus, Tokyo, Japan). The emitted light is separated from the incoming infrared light by dichroic mirrors situated behind the condenser and behind the objective. The wavelengths of light are detected by different GAaSP photomultiplier tubes (H744p-40, Hamamatsu, Hertfordshire, UK) which are located behind different band pass filters. For the results presented in chapter 3 and 4, the photons were collected through an objective and an oil condenser (ND 1.4, Olympus, Tokyo, Japan) (Figure 2.4.B.). The condenser was essential to increase the signal to noise ratio and to resolve single vesicles. The signals from the objective and the condenser were added up with an amplifier. The sampling rate was between 500 Hz and 1 kHz. Scanning and image acquisition (linescan) were monitored using ScanImage v.3.8 software (Pologruto et al., 2003).

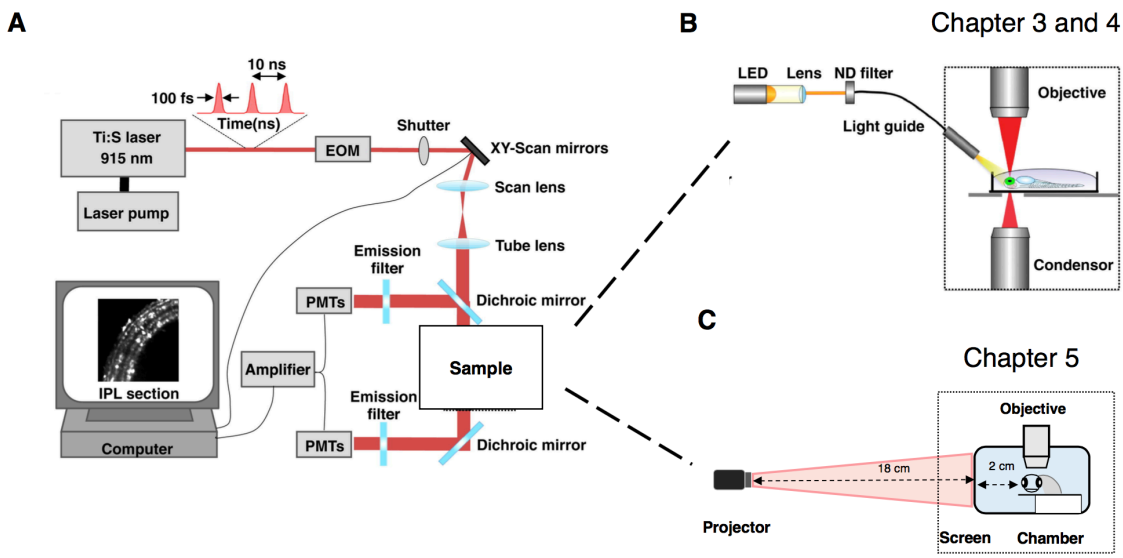

Figure 2.4. Imaging glutamate release in the retina of live zebrafish using a two-photon microscope. (Adapted from Odermatt et al., 2012)

(A) Imaging set up of the two-photon microscope used to perform the experiments.

(B) Mounting configuration to measure quanta of glutamate from BCs (chapter 3 and 4). Full-field stimuli were applied through a light guide. The signals were recorded with an objective and a condenser. The condenser was essential to increase the ratio signal to noise.

(C) Mounting configuration to study pattern adaptation in the retina (see Chapter 5). Spatial gratings were presented to the fish with a screen.

EOM= Electro optical Modulator

PMT= Photo Multiplier Tube

2.2.2. In vivo zebrafish recordings

2.2.2.1. Stimuli

An Optoma PK320 pico projector (Optoma, Watford, U.K.) was customized by inactivating the power supply to the green and blue LEDs (but not the red LED). This prevented light bleeding through to the recording photomultiplier tube from the green channel (with an emission filter HQ 535/50, Chroma Technology, U.S.A.). The mean irradiance of the screen was: 12.7 nW mm^{-2}. Visual stimulation was synchronized with imaging by recording the times of screen refresh rates during stimulus presentations using custom-written code (Matlab software) and a U3 LabJack digital-to-analog converter (Labjack, Lakewood, CO, U.S.A.). The size of the grating was 4.1 degrees and the temporal frequency was 5 Hz. For RGC recordings, three sequences of four gratings with opposite orientations (0 degrees or 90 degrees) were projected on the screen (Figure 2.4.C.). Each grating lasted 10 s and each sequence was separated by 15 s of constant light (see Chapter 5). The laser power used for the recordings was 50 mW.

Full field light stimuli were delivered by amber LED (thorlabs, Ely, UK) (590 nm), filtered through a 590/10 nm band pass filter, controlled in Igor Pro 6.37, and time locked to image acquisition. Responses of BCs to contrast were assessed with the following protocol: constant median light (10 s), temporal contrast (from 10 to 100 %) (sine wave) for 20 s, followed by constant median light (10 s). A new trial started one minute after the end of the previous one (chapter 3 and 4). Modulations were around a mean intensity of 165 nW/mm^2. The other protocols are described in more details in the result chapters. The laser power used for the recordings were 10 mW with *Tg*(*ribeyeA:nlsTrpR, tUAS:SF-iGluSnFR)* and 30 mW with *Tg(ribeyeA:Gal4, UAS:iGluSnFR).*

2.2.2.2. Drug application (Chapter 5)

Manipulating GABA and Glycine signaling in the retina was achieved by injecting ~1 nL of a solution containing 10 mM gabazine and 10 mM strychnine in the vitreous

space between the retina and the lens of the zebrafish larvae. Given that zebrafish eyes can be approximated as a hemisphere and that its diameter is about 200 μm, the maximal dilution of the drugs in the retina was estimated to 1(Johnston et al., 2018).

2.2.2.3. Laser ablation (Chapter 3 and Chapter 5)

Laser ablation was performed on the soma of the cell. The laser wavelength used was 800 nm. Laser irradiation was performed under simultaneous visual control. When the field of view became overexposed, the ablation was stopped.

2.3. Analysing iGluSnFR signals

2.3.1. Quanta analysis (Chapter 3 and Chapter 4)

Several steps were necessary to analyse the linescan of iGluSnFR (summarized in Figure 2.8.). The iGluSnFR signals were obtained by using high sampling rate (1 kHz) with two-photon microscopy. Due to the kinetics of iGluSnFR (that are faster than those of calcium reporters), several algorithms had to be developed to extract and analyse iGluSnFR signals. The procedures were semi-automated using a Graphical User Interface (GUI).

- Extraction of the fluorescence.

Initially, the fluorescence signal from the BC terminals were plotted (Figure 2.8. A.) as a kymograph.

- ROI extraction

The next step in the analysis was to extract the iGluSnFR signals from recordings containing several sources of glutamate release (active zones). The different ROIs were isolated assuming that once glutamate is released, its concentration in the

synaptic cleft can be described by diffusion. Since the temperature and pressure are constant in the zebrafish retina, Fick's second law of diffusion predicts how glutamate concentration changes with time:

$$\frac{\partial C}{\partial t} = D\frac{\partial^2 C}{\partial x^2} \tag{1}$$

where **C** is the glutamate concentration, **t** is time, **x** is the distance in the synaptic cleft, and **D** is the diffusion coefficient. From a single point source, the diffusion can be estimated.

Hence, the concentration of glutamate release from one active zone can be described with:

$$c(x,t) = \frac{N}{2\sqrt{\pi D t}} * \exp\left[-\frac{x^2}{4Dt}\right] \tag{2}$$

where **N** is the total number of glutamate molecules released at x=0. Since D is difficult to estimate due to the noise of the recordings, it is possible to approximate it with a Gaussian function.

If

$$2Dt = \sigma^2(t)$$

then

$$c(x,t) = \frac{N}{\sqrt{2\pi\sigma^2(t)}} * \exp\left[-\frac{x^2}{2\sigma^2(t)}\right] \tag{3}$$

The formula has the form of a Gaussian equation where σ^2 represents the variance (it increases with time). Hence, it is possible to compute the spatial profile (average over the time dimension) of a linescan and to fit this spatial profile with a sum of Gaussian curves with the build-in curve fitting software in Igor:

$$k(x) = \sum_{i=1}^{n} \frac{A_i}{\sqrt{2\pi\sigma_i^2}} * \exp\left[\frac{-(x-\mu_i)^2}{2\sigma_i^2}\right] \quad (4)$$

where $\boldsymbol{A_i}$ is constant, $A_i > 0$ and $\boldsymbol{\mu_i}$ is the average of the Gaussian. To avoid overfitting the spatial profile, μ_i was determined manually (It represents the local maxima of the spatial profile). The total number of components is equal to the number of averages determined (Figure 2.5.B).

-Extraction of Fluorescence trace.

Once each spatial component had been defined, a time-series for that component, **F(t)**, was calculated based on the linescan and the Gaussian equation presented in (6). To extract the signals from the centre and to remove noise as well as to demix signal from other active zones, the weight of pixels located at the centre of the spatial profile was higher than the pixels located at the edges of the profile.

$$F(t) = \sum_{x} F(x,t)k(x)\,, \quad (5)$$

where **F(x,t)** is the raw linescan matrix and **k(x)** is the Gaussian component for the ROI (6).

- Calculation of the ΔF/F.

Extracted fluorescence traces were corrected with a linear function fit using the mean fluorescence taken from the beginning and the end of the recording session. If excessive photobleaching was observed, the baseline for the entire trace was calculated and subtracted as well (Figure 2.8.B.). A correction was made by scaling F(t) according to a linear function fit using the mean fluorescence taken from the beginning and the end of the episode. The relative fluorescence $\Delta F/F_0$ was then calculated from the corrected signals. the most frequent value (i.e. the baseline) of the trace was used as F_0. The trace was then smoothed using a Savitzky-Golay filter.

This filter allows a better signal-to-noise ratio without altering the original signal (Figure 2.8.C.).

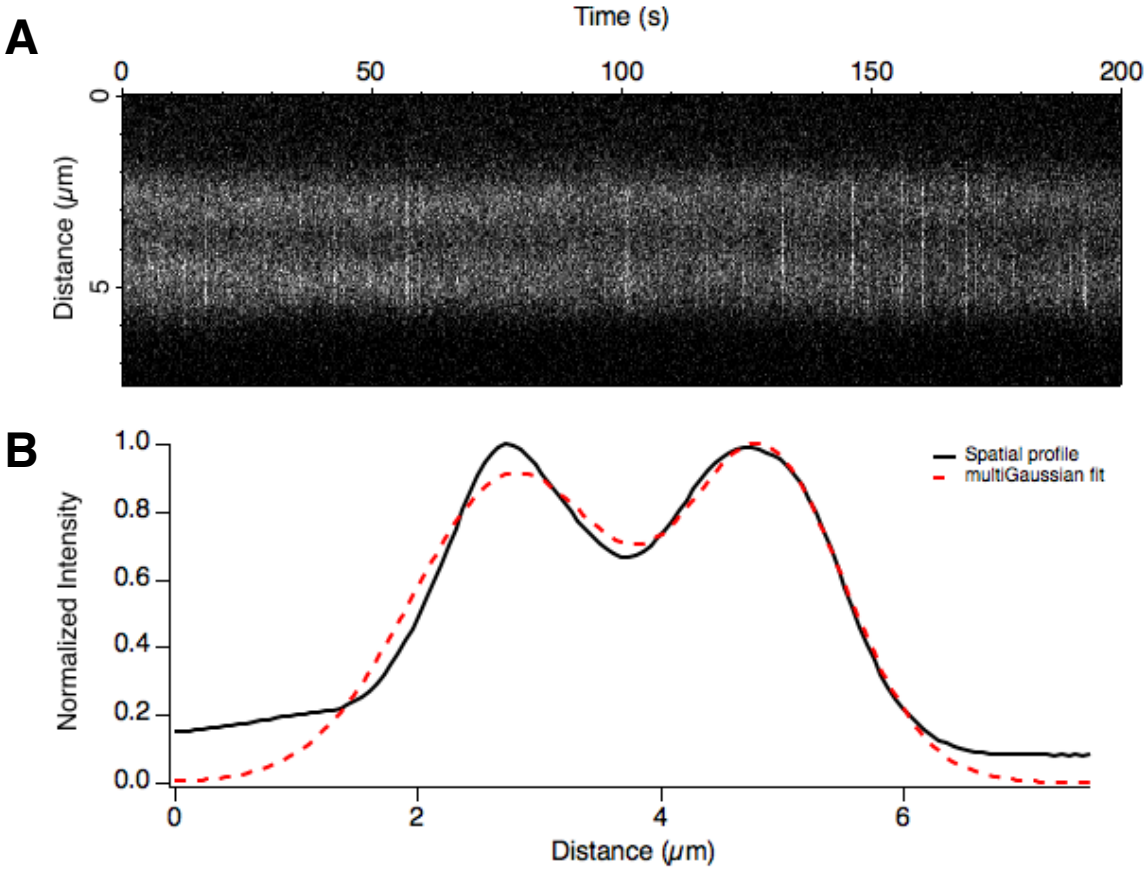

Figure 2.5. ROI extraction.

(A) Example of a recording (linescan) from my experiments (spontaneous activity).

(B) Averaging over time resulted in a spatial profile (black trace). The mean for each peak was manually selected and a sum of two Gaussian fit detected the two active zones (red dashed line).

- Deconvolution

To remove the noise from the resulting trace, the trace was deconvolved. SF-iGluSnFR and iGluSnFR are linear under the conditions of the experiments, suggesting that the system could be described by a linear time invariant system (LTI). Under these conditions, a Wiener Deconvolution (Wiener, 1964) could be used to analyse the extracted fluorescent trace. The kinetics of iGluSnFR fluorescence for an event could be described by the following equation:

$$h(t) = A * exp\left[-\frac{t}{\tau_f}\right] * \left(1 - exp\left[-\frac{t}{\tau_r}\right]\right), \quad (6)$$

where ***A*** describes the amplitude of an uniquantal event and, τ_f and τ_r are the parameters guiding the exponential fall and rise of fluorescence, respectively. For most of the traces, I used **tf**=0.06 and **tr**=0.001. A Wiener kernel can be calculated from the parameters selected (Figure 2.6.). The trace was then deconvolved using this Wiener kernel. This process allowed me to separate events that occurred closely in time (Figure 2.8.D).

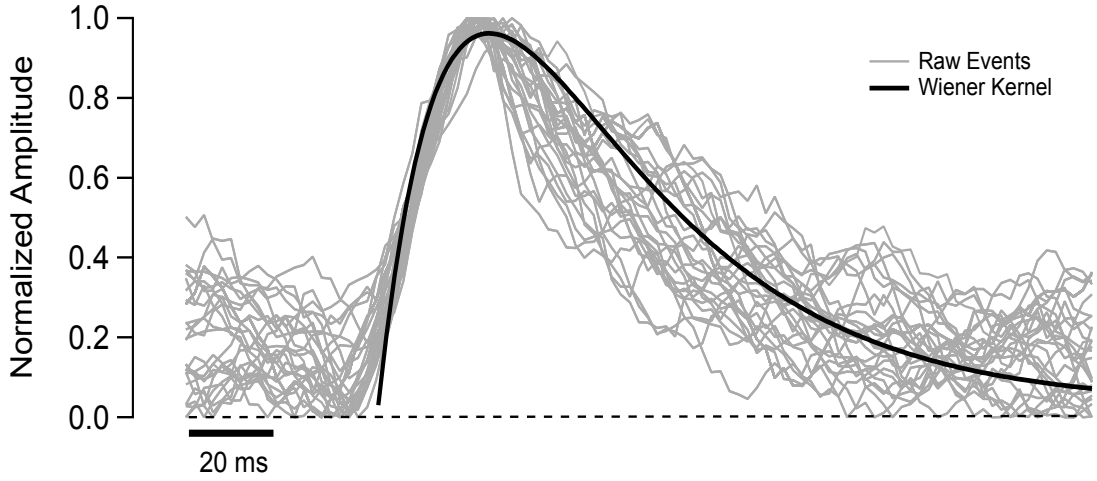

Figure 2.6. Events from raw traces overlaid with a Wiener Kernel. (Data from Lagnado's laboratory (James et al., 2018)

The raw events (grey traces) were normalized and are superimposed with a Wiener kernel (black trace) (**tf**=0.06 and **tr**=0.001). The Wiener kernel describes the events and does not contain noise anymore.

- Event Extraction

The deconvolved trace was used to determine events by selecting a threshold. The threshold was determined to detect the smallest events (the unitary events). The amplitudes were then extracted from the deconvolved trace using this threshold (Figure 2.8.E.).

- Amplitude Clustering

To determine how many quanta each event consisted of, the deconvolved amplitudes were plotted as a histogram. An expectation maximization (EM) algorithm (Dempster et al., 1977 ; Do and Batzoglou, 2008; Ceppellini et al., 1955) was used to cluster the amplitudes from events into quanta (Figure 2.7.). For each active zone, the algorithm generated 15 time clusters with different component numbers. The deconvolved amplitudes were then plotted as a histogram as well as each partition. An optimal clustering was manually chosen. The clustering was optimal when the number of clusters matched the number of peaks observed. For each event, the number of quanta was determined based on the clustering selected. Each deconvolved amplitude was clustered into a number of quanta per event based on this selection (Figure 2.8.F).

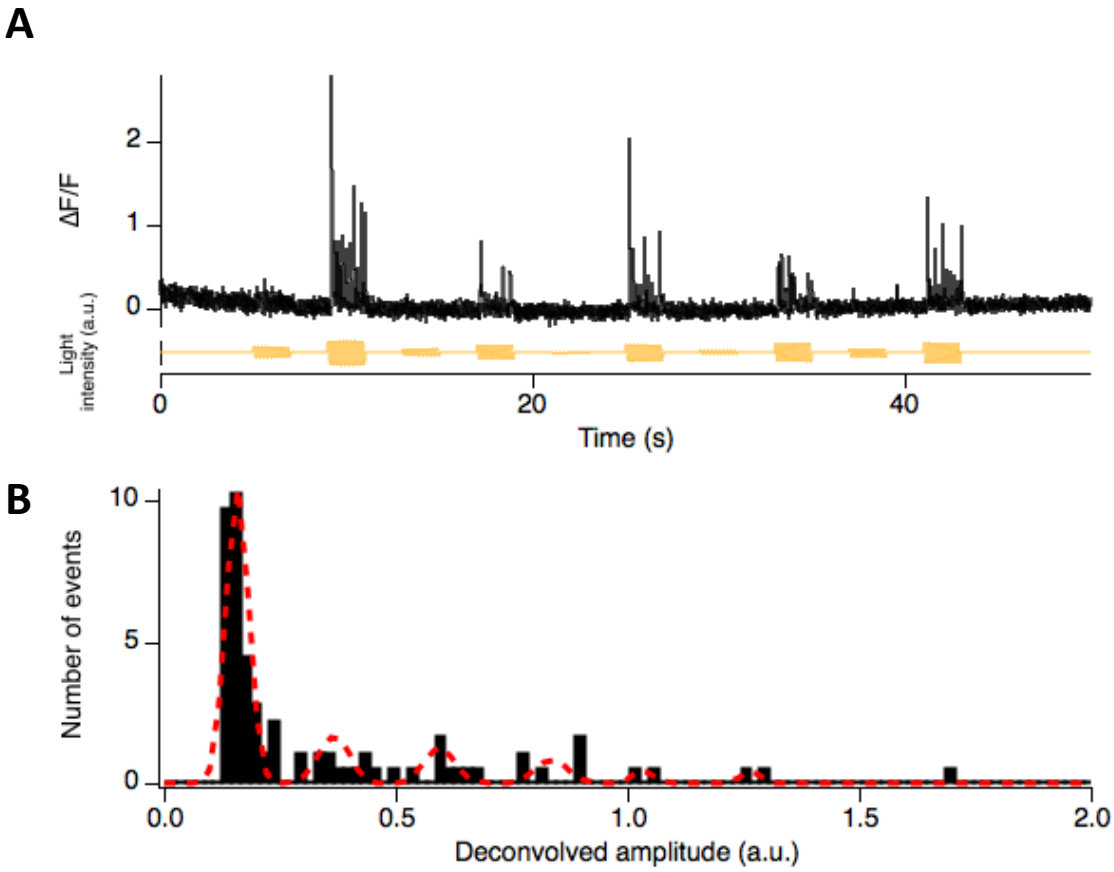

Figure 2.7. Histogram of deconvolved event amplitudes.

(A) Example of a recording containing events with different amplitudes. The experiment consisted in presenting different contrasts at 5Hz. Each contrast was presented in randomly for 2s.

(B) The amplitudes from the deconvolved events were plotted as a histogram (black bars).

An EM algorithm was used to decompose the events into sets of Gaussian components (red dashed trace). Note that the intervals between peaks are equal.

a.u.=arbitrary unit

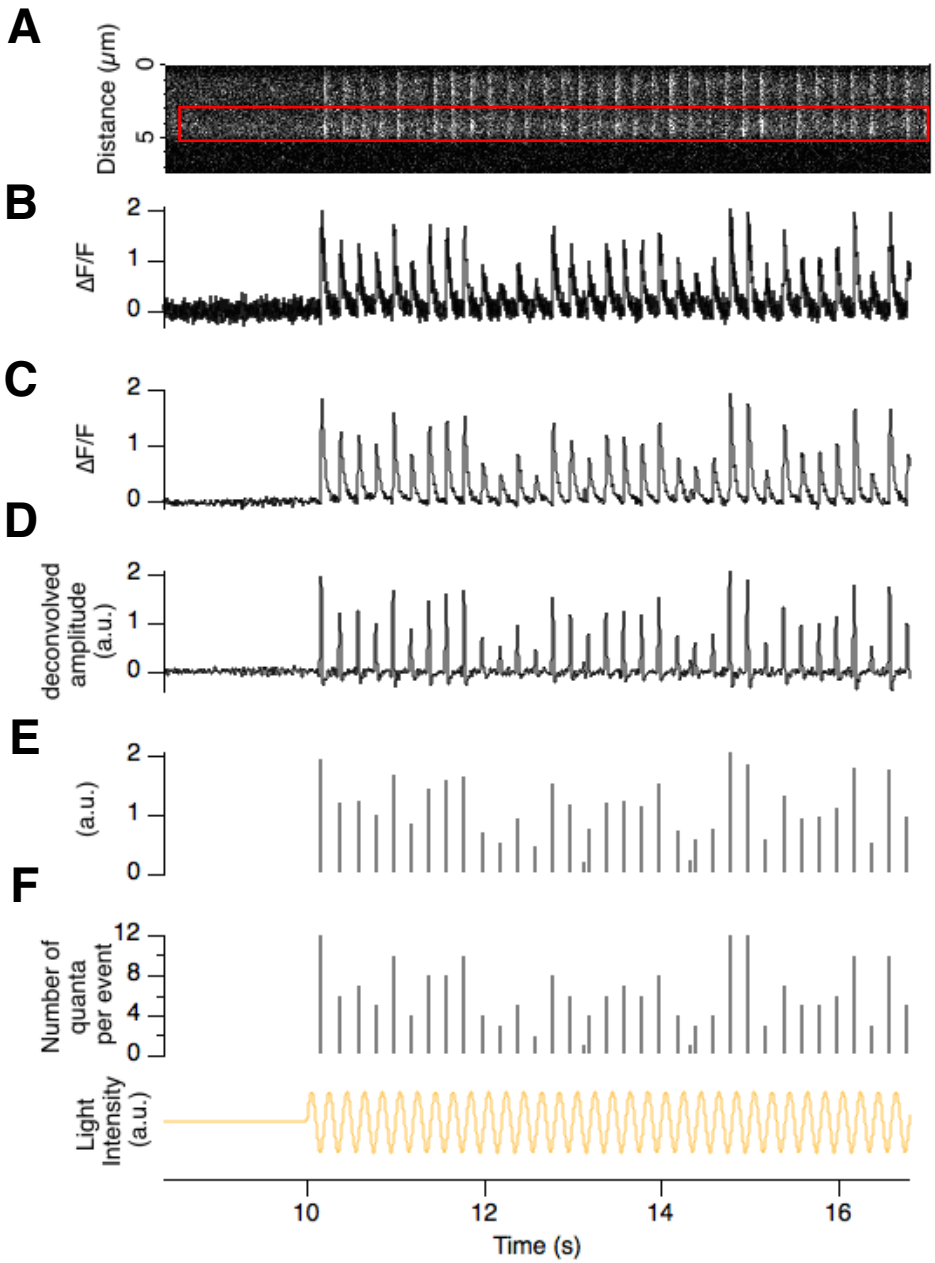

Figure 2.8. Analysis of a linescan recording of iGluSnFR in a terminal.

(A) Example of a linescan recording (the stimulus was a contrast a 5Hz).

Analysis of the bottom active zone presented in (A) (red dashed square):

(B) Raw trace (ΔF/F)

(C) Smoothed trace using a Savitzky-Golay filter.

(D) Deconvolved trace (obtained using a Wierner deconvolution).

(E) Deconvolved amplitudes. A clustering is made from a histogram of the amplitudes. These clusters each amplitude in a quanta number per event.

(F) Number of quanta per event.

2.3.2. Time window for discrimination of events

iGluSnFR kinetics are fast (Marvin et al., 2013). However, due to noise condition and the fast kinetics of events. If two events are too close from each other, they may be not easily distinguished by the algorithm anymore. Hence, it is essential to evaluate the minimal time windows where two events cannot be distinguished anymore (temporal discrimination window). A series of events were simulated with different inter event interval. The signal to noise ratio used to simulate these events was similar to the one observed in the experiments. The analysis of these events was then performed using the method explained above (see 2.3.1.). Figure 2.9. indicates that when two events are within a window of 10 ms, then cannot be discriminated from each other. Hence the time discrimination window seems to be 10 ms.

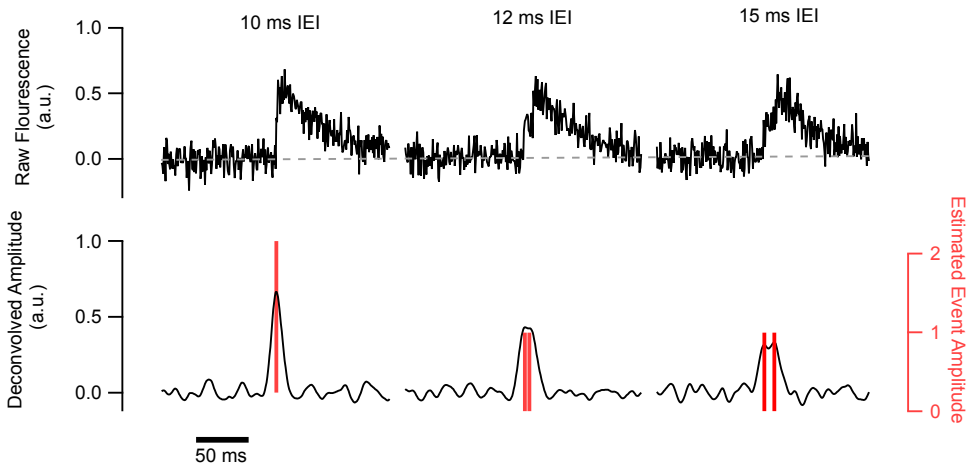

Figure 2.9. Examples of event simulations used to estimate the temporal discrimination window. (Data from Lagnado's laboratory (James et al, 2018)).

Left: Two uniquantal events separated by 10 ms. These events were incorrectly classified as a single 2-quanta events (bottom). Middle: Two events separated by 12 ms generated two distinguishable maxima in the deconvolved trace counted as two distinct events, the amplitude and timing of which is shown by the vertical red bars (bottom). Right: Two uniquantal events separated by 15 ms could be distinguished too.

2.3.3. Analysis of iGluSnFR signals in RGCs (Chapter 5)

Data processing was performed in Igor Pro 7 and SARFIA routines (Dorostkar et al., 2010). A custom-written algorithm of signal identification extracted fluorescence from synapses. Regions of interest (ROIs) corresponding to synapses were extracted from the registered time series using an iterative method. First, a local correlation was established by cross correlating time series of each pixel with its eight neighbors. The first pixel was replaced by the maximum value. The local correlation map was used afterwards to seed the ROIs. This process was iterated for all the neighbors of all the pixels added to the ROI. The process was repeated until no further pixel was added to the ROI. I chose a local correlation threshold to add pixels to the ROI. This threshold was kept consistent for each fish. I carefully joined the ROI that were strongly correlated (Johnston et al., 2018). This ensured that I did not count synaptic terminals belonging to single RGCs more than once. More precisely, the steps of the analysis were:

-Correlation map.

A local correlation map is created from the raw movie. It generates a pixelised image of the average of the movie (Figure 2.10.A and Figure 2.10.B) where each bright pixel represents the maximum correlation between it and its neighbours. The correlation between pixels was based on the activity of the neuron (a Pearson's correlation was calculated between each pair of neighbouring pixels). I manually adjusted the threshold for each recording to select the areas that were responsive (the areas that were bright because of neuronal activity, not because of the expression level of the reporter) (Figure 2.10.B.). The value that I chose was used afterwards to segment the movies into ROIs. I decided on the minimum of pixels that each ROI contained (20 pixels for RGC outputs and 5–10 pixels for RGC inputs), and a threshold value for the correlation between the neighbouring pixels and the local maximum pixel. If the neighbouring pixels had a higher value than the threshold, they were included in the ROI (an example is shown in Figure 2.10.C.).

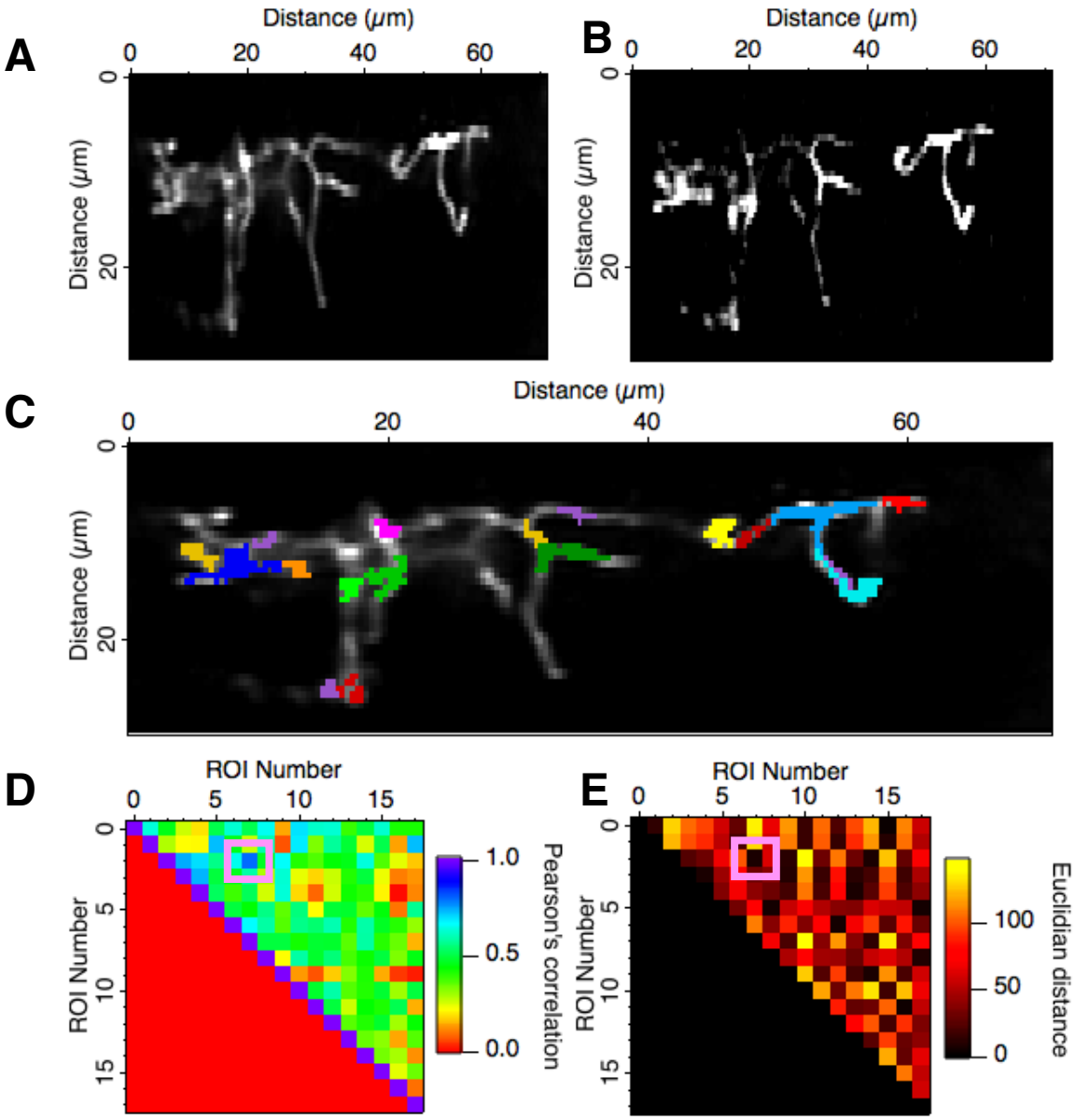

Figure 2.10. Analysis of iGluSnFR signals in RGCs.

(A) Overview of RGC dendrites.

(B) Correlation map of a recording from the RGC dendrites presented in A.

(C) Segmentation showing the different ROIs generated with the correlation map.

(D) Pearson's Correlation matrix between different ROIs.

(E) Euclidian distance between different ROIs. The pink square represents two ROIs that have the highest Pearson's correlation coefficient (0.79). These ROIs are close to each other (Euclidian distance close to 0). These ROIs are potential candidates to be joined.

- Final ROI selection.

I then compared ROIs with a cross correlation matrix created with the segmentation. This matrix contained a Pearson's correlation between pairs of ROIs. (Figure 2.10.D.). The Pearson's correlation coefficient for each pair of fluorescence traces was calculated with the following formula (from Igor software):

$$\mathrm{r} = \frac{\sum_{k=0}^{n-1}(\mathrm{traceA[k]} - A)(traceB[k] - B)}{\sqrt[2]{(\sum_{k=0}^{n-1}(traceA[k] - A)^2 * (\sum_{k=0}^{n-1}(traceB[k] - B)^2}} \quad (7)$$

where trace **A** and trace **B** represent different responses from ROIs. **A** is the average of the elements in the trace **A**, **B** is the average of the elements in trace **B**, and the sum is over all the elements. **r** is the Pearson's correlation coefficient.

A distance matrix was calculated to evaluate the physical distance between two ROIs (Figure 2.10.F.). The centre of mass for each ROI was used to calculate the Euclidian distance **d** between each pair of ROIs:

$$d = \sqrt{(xa - xb)^2 + (ya - yb)^2} \quad (8)$$

where **xa** and **xb** are the x coordinates of two ROIs, **ya** and **yb** are the y coordinates of two ROIs from the average picture of the raw movie analysed (Figure 2.10.A).

I used these two matrices to join two ROIs if they had a square Pearson's correlation coefficient over 0.8. Moreover, I could overlap traces from two different ROIs with a high Pearson's correlation coefficient to check whether they were very similar and from the same cell. Each time that I joined two ROIs, the matrix containing the raw fluorescence (Figure 2.11.D.) trace was updated. The final ROIs for the example in Figure 2.10. are shown in Figure 2.11.A.

- Calculation of the ΔF/F.

The F_0 was calculated from average of the five seconds before the start of the grating. $\Delta F/F_0$ was then calculated using this value.

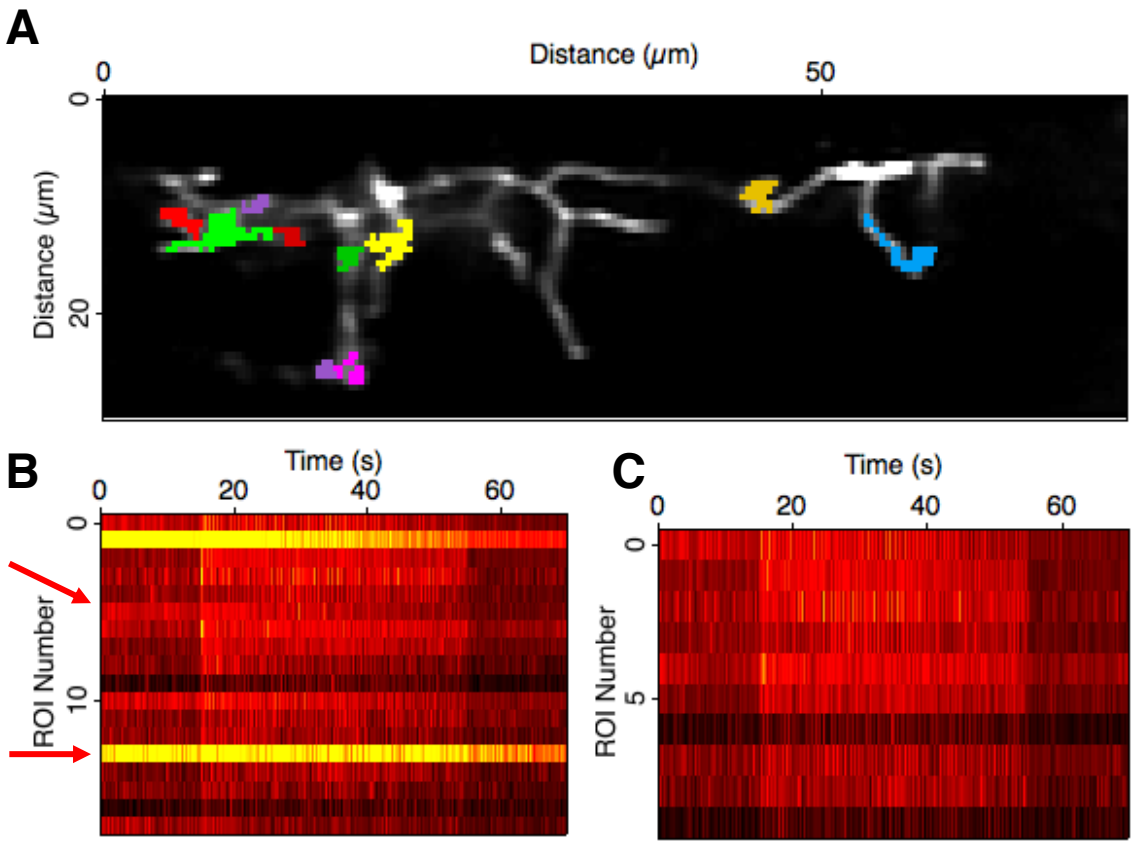

Figure 2.11. Final selection of ROIs.

(A) Final ROIs that were selected.

(B) Raster plot showing ROI traces before selection. The upper arrow indicates an ROI with a lot of photobleaching, not suitable for analysis. The lower arrow shows an ROI that is not responding to the stimulus.

(C) Raster plot showing ROI trace after final selection.

Chapter 3

Multivesicular release revealed by imaging iGluSnFR *in vivo*

3.1. Introduction

How is visual information encoded by synapses? BCs are uniquely positioned among graded and spiking neurons. Classically, BCs were thought to encode visual information only with graded signals (Wässle and Boycott, 1991, Masland, 1996) but it is now commonly accepted that they use both graded and digital encoding (see 1.1.3.3.) (Dreosti et al., 2011; Baden et al., 2011; Saszik and DeVries, 2012; Lipin and Vigh, 2015). However, how BCs transmit visual information by vesicles release is less understood. Since the work of Katz and Heuser (Katz and Del Castillo., 1954 ;Heuser and Reese, 1973)(see Chapter 1), it has been established that neurotransmitters are released as quanta that correspond to vesicles. Do BCs release vesicles one by one or release several vesicles per active zone in a synchronous manner and simultaneously? The release of several vesicles in a response to a stimulus is named Multi Vesicular Release (MVR) (see 1.2.2.).

MVR is specific of some neuron types. As explained in Chapter 1, MVR consist in the release of several vesicles in response to an action potential. When the release is quasi-simultaneous, it indicates that the release is coordinated (the release of vesicles can be coordinated by diverse mechanisms at the level of the presynaptic element such as compound fusion). The active zone is an area localized in the presynaptic element of the synapse that mediates neurotransmitter release. It composed of different proteins such as the cytomatrix at the active zone or the ribbon protein in BCs. Proteins at the active zone tether vesicles to the presynaptic membrane and monitor the synaptic vesicle fusion to have a fast and reliable fusion in response to an action potential. In BC terminals, multivesicular release is mediated by ribbon synapses. The release modality of vesicles remains under debate but the active zones might be constituted of different release sites along the ribbon protein that coordinate MVR.

The existence of MVR stayed controversial because it was thought that only one vesicle could be liberated per release site (Korn and Faber, 1991;Korn et al., 1994; Redman, 1990; Zucker, 1973) or that MVR could not be detected with electrophysiology (recordings at the postsynaptic neuron after current impulses in the presynaptic neuron) because the release of a single quantum could already saturate all the postsynaptic receptors (Redman, 1990). However, this view has been challenged in central synapses. Several *ex vivo* studies using postsynaptic neuronal recordings provided evidences of MVR in the brain:

-hippocampus: dissociated neuronal cell culture (Tong and Jahr, 1994) and organotypic slice (Oertner et al., 2002).
-ear: auditory hair cells (Li et al., 2014; Glowatzki and Fuchs, 2002).
-cerebellum: stellate and basket cells (Auger et al., 1998).
-cerebral cortex : Purkinje cells (Wadiche and Jahr, 2001).
-hypothalamus: paraventricular nucleus neurons (Gordon and Bains, 2005).

Several drawbacks exist concerning the results for most of these studies. Primarily, some of the studies could not rule out that the release of several vesicles originate from different active zones (Tong and Jahr, 1994; Gordon and Bains, 2005; Wadiche and Jahr, 2001; Auger et al., 1998), the asynchrony of individual quanta constituting the multivesicular events suggested that the release sites were not coordinated (Singer et al., 2004) or did not have the adequate time resolution; the release of several quanta would have be within a window of 10 milliseconds (Oertner et al., 2002). Moreover, concerning some of these studies (cerebellum, cortex and hypocampus), MVR could have been caused by a high release probability of the release site and not by coordination (asynchronous release). MVR has already been observed at ribbon synapses in other sensory systems (Li et al., 2014). In hair cells, vesicle release was highly synchronous, suggesting that release might be temporally coordinated in hair cells. Like hair cells, BCs are good candidates for using MVR because of their synaptic structures, the ribbon synapses that could act as a convey

belt for vesicles and could facilitate the coordinated fusion of vesicles. Singer et al., 2004 carried out *ex vivo* paired recordings in mouse retina from presynaptic rod BCs and postsynaptic AII ACs and found that the excitatory post synaptic current (EPSC) indicated MVR at the rod BCs synapses. From these experiments, the authors suggested that BC active zones were releasing simultaneously several glutamate vesicles. They showed that the simultaneous release of vesicles was synchronized, indicating that the release of vesicles was not random but originated from a coordinated mechanism. They calculated the number of vesicles for observed EPSCs and found that in some cases the number of vesicles exceeded the number of active zones contained in rod BCs. To explain these findings, they suggested that these cells use MVR. To explore this hypothesis, they first isolated spontaneous events (mEPSCs). The amplitude of these mEPSCs did not change when they varied the external concentration of calcium, showing that these events were likely uniquantal. Next, they showed that the presumed MVR events were coordinated by isolating individual synaptic events. The rise time of the large EPSC was similar to the EPSC generated by uniquantal events, indicating that the release of multiple vesicles was nearly simultaneous, implying that the release of these vesicles was coordinated. However, this study has several drawbacks. It was performed *ex vivo*, without visual stimuli and they did not record signals from individual active zones.

Taken together, several previous studies point at a role of MVR in synaptic transmission at sensory synapses. However, how MVR can be used to encode sensory information remains poorly understood. To tackle this issue, I expressed the fluorescent reporter iGluSnFR (Marvin et al., 2013) in BCs of larval zebrafish. This enabled me to observe *in vivo* glutamate transmission in BCs (Franke et al., 2017, Borghuis et al., 2013). In this chapter, I show that using this technique, it is possible to observe single vesicle associated iGluSnFR signals from single active zones. The iGluSnFR transients had different amplitude suggesting that events were constituted of different number of vesicles. Histograms from the iGluSnFR signal amplitudes shows multiple peaks with equal interval that likely correspond to multiple quanta,

suggesting that it is possible to observe single vesicles with iGluSnFR and that BCs perform MVR *in vivo* (the release of several vesicles in one event). It has been shown that release site from single active zone operate independently (Katz, 1969). As explained before, the structure of the ribbon might organize vesicles at release sites that facilitate MVR. To show that MVR was coordinated at the level of single BCs active zones, I showed that the distribution of intervals between events was not distributed exponentially as it should be if the vesicle release sites were distributed independently. I then show that, during visual stimulation, the distribution of quanta per event is not described by a Poisson process as it should be if the release sites were independent.

3.2. Methods

Due to the fast kinetics of iGluSnFR sensor ($\tau_{1/2}$ rise around 11ms (Marvin et al., 2013)) recording with a conventional frame rate (around 10 Hz) would not enable the detection of the fast release of neurotransmitter, some event would be missed, amplitudes would be underestimated and their timing inaccurately evaluated. Accordingly, I used linescans at 1 KHz (Oertner et al., 2002, Borghuis et al., 2013, Mainen et al., 1999a, Mainen et al., 1999b) (see Chapter 2.). This allowed capturing peak amplitudes of iGluSnFR signals before decay. Figure 3.1 shows an example of iGluSnFR signals recorded at 1 kHz using in the linescan mode (Figure 3.1.B.). Each line of one panel represents one acquisition. An example of a BC with one terminal is shown in this figure. I scanned a BC terminal along the line indicated (Figure 3.1.A.) using the software ScanImage. A full-field light stimulus of 1 or 5 Hz temporal contrast and varying intensity modulation was presented to the fish from an amber LED (590 nm). At 10% contrast, events were more transient and had lower amplitude than the ones at 100% contrast (Figure 3.1.D). The events at 10% were more variable too. Moreover, the events have different amplitude, indicating that each event may be constituted of a different number of vesicles.

The recordings were analysed as described in 2.3.1.

For the distance between ribbon analysis, the retina of 7 dpf larvae were dissected and the retinal epithelium was gently removed. The retina were incubated in permeabilization (PBS with 0.5% Triton X-100 and for 10 min followed by 3 days incubation at 4°C with primary antibodies (rabbit anti-GFP (millipore, 2127776, 1:500), chicken anti-ribeye a (Cambridge Research Biochemicals, 1:200). Samples were rinsed three times in phosphate buffered saline with 0.5% Trion-X 100 and incubated for another day with secondary antibodies : Alexa-546 anti-chicken and for GFP (Invitrogen, 682609, 1:500) and Alexa-647 anti-rabbit (Invitrogen, 464140, 1:500). Finally, samples were washed in PBS with 0.5% Triton X-100 and mounted in mounting media (VectaShield, Vector, H-1000) for fluorescent imaging. Confocal images were taken on Leica TCS SP8 using objectives 63x (HC PL APO oil CS2, Leica), at xy: 0.1-0.07 µm/pixel, and z-step: 0.25µm for high-resolution images. Images were median-filtered and brightness and contrast were adjusted in FIJI (NIH). The pictures were analysed with FIJI.

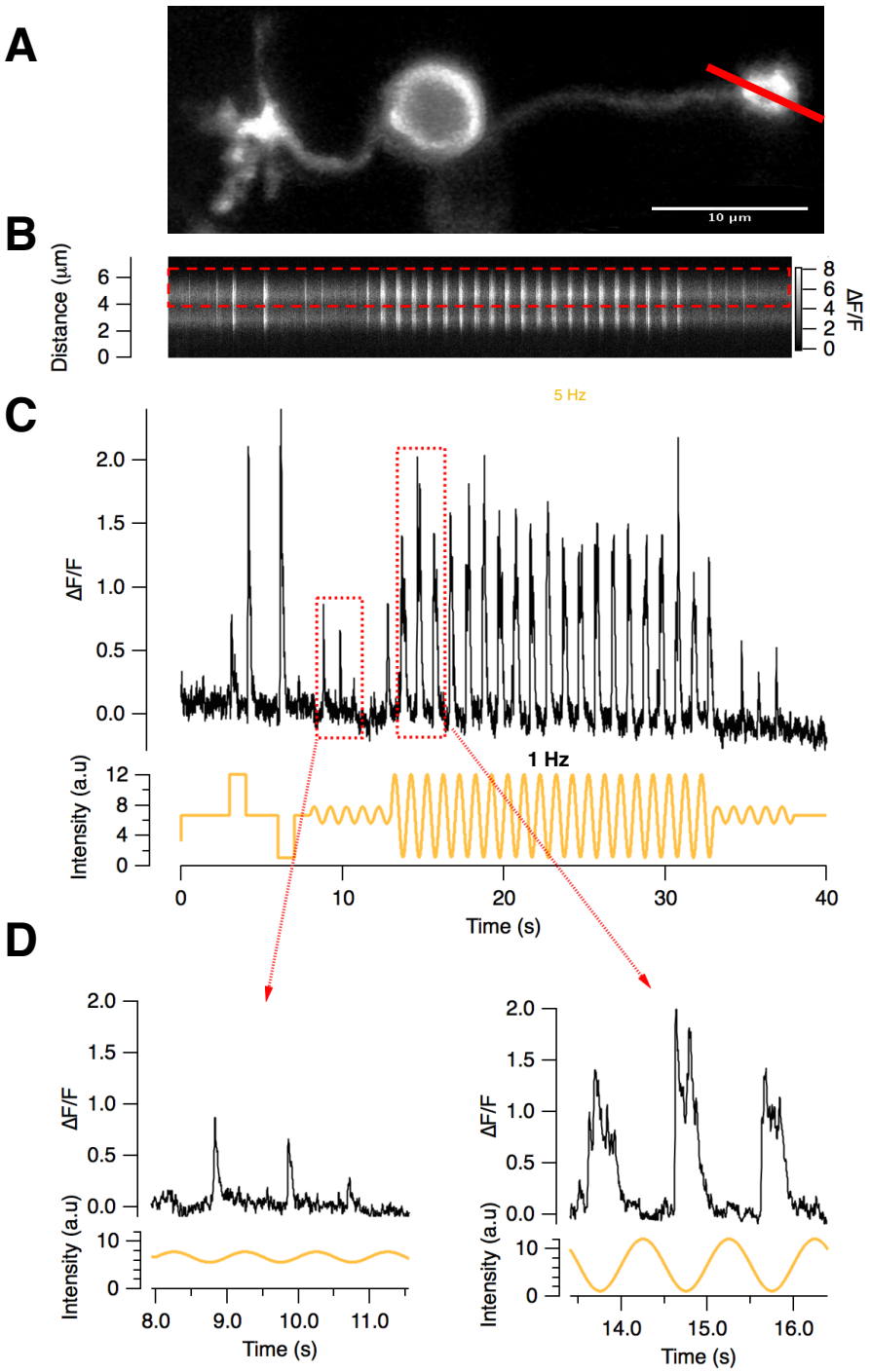

Figure 3.1. iGluSnFR signals from a BC terminal.

(A) Image of a BC cell expressing iGluSnFR. The red line represents the line scanned by the laser.

(B) Linescan recording from the same BC. Note that we can distinguish two different synapses. During my experiments, I did not observe iGluSnFR signals from axons.

(C) Temporal profile of the linescan of the upper synapse (from the red dashed square of (B)).

(D) Trace from zoom in areas presented in (C). Note that at low contrast the events are more transient than at high contrast.

The Poisson cumulative distribution function from 3.3.4. was calculated with custom script from Lagnado's laboratory with the following equation:

$$f(x) = 1 - \exp\left(-\frac{x}{\lambda}\right) \quad (10)$$

Where λ is the average of time interval between events.

3.3. Results

3.3.1. iGluSnFR does not detect spillover from neighbouring bipolar cells

Spillover of neurotransmitter from synapses is an important mean of transferring information in various parts of the brain. For instance, the importance of spillover was shown in information processing between mitral cells (Isaacson, 1999) as well as for communication between Purkinje cells and interneurons of the cerebellum (Szapiro and Barbour, 2007). Furthermore, spillover induces heterosynaptic LTP (Long Term Potentiation)/ LTD (Long Term Depression), increases the EPSC durations and permits a homeostatic regulation of glutamate release in hippocampal slices (Arnth-Jensen et al., 2002). Thus, even if it has never been reported before, spillover might occur in the IPL of the retina (Borghuis et al., 2013). This may cause some difficulties concerning the interpretation of the data because if iGluSnFR senses glutamate spillover from neighboring BCs, the measurement of glutamate would be not only the glutamate release of the terminal of an interest but also the neurotransmitter release from other synapses. To test to what extent glutamate spillover may affect our results, I designed the following experiment. A soma from a single BC expressing the probe is ablated and the signals from the BC terminal are recorded before and after ablation. If there are still signals at the synapse (that are not due to spontaneous activity), then it means that spillover is detected by

iGluSnFR.

Figure 3.2. shows the results of this experiment. The red trace shows the response of a BC terminal before ablation of the soma. The trace on the right (Figure 3.2.B.) represents the response of the synapse once the soma has been ablated. The results indicate that there are no synaptic responses after ablation of the soma.

To understand whether cells close from the ablated cell were affected by the ablation, preventing spillover to happen (this could explain why there was no signal recorded at the synapse from the ablated cell) a neighbouring cell was recorded before and after ablation as a control. Figure 3.2. indicates that the control cell is still responding after ablation, indicating that the physiological environment of the ablated cell was not affected. In total, two ablation experiments were performed and they both showed the same results. Hence, we concluded that iGluSnFR does not detect spillover and the signal recorded from a BC terminal corresponds to glutamate release from the same synapse (James et al., 2018).

This type of experiment was performed in Chapter 5 on RGCs . I found the same result : IGluSnFR does not detect glutamate release form neighbouring synapses. One limit of my laser ablation experiment is that I did not have positive controls. If I observe responses with this experiments, it was difficult to know whether it is because the laser ablation failed or whether it is due to spillover. One experiment that I could be performed is glutamate uncaging by two-photon microscopy. Caged compound are biological molecules (such as glutamate) which have been rendered inert by the attachment of a photochemical group (Ellis-Davis, 2000). These molecules enables a local photochemical release of caged compounds by two-photon microscopy. Some compounds such as Nitroindolinyl-caged glutamate can be photolyzed at the range of 710-730 nm. Moreover, two-photon photolysis of these compounds enables the activation of single synapse (Matsuzaki et al., (2001)).

Therefore, by uncaging glutamate at different distances of IGluSnFR, it would be possible to know the minimal distance for iGluSnFR to detect glutamate from BC

terminals *in vivo.*

However, this experiment has some limitations. First, the distance between BCs terminals is not known. Hence, even if the minimal distance between glutamate and IGluSnFR is determined of might be difficult to know whether it is smaller that the distance between two terminals. Some data from electron microscopy could help to resolve this issue. Second, The concentration of glutamate release during photolease is not known and it would be better to monitor the uncaging of glutamate representing several vesicles to monitor glutamate release in physiological conditions.

Another way to study spillover at bipolar cells terminals could be to know the concentration of glutamate in neighbouring bipolar cells after glutamate release. The concentration of glutamate within one vesicle has been estimated between 60 mM and 200 mM. This concentration is high enough to be detected by iGluSnFR although is likely not reflecting the concentration of glutamate in the synaptic cleft of bipolar cells. The concentration profile in glutamatergic synapses has been study by Clements et al., (2012). The peak of glutamate is 1.1mM it is still within the range of what can be detected. The glutamate diffuses in the synaptic cleft and decayed with a time constant of 1.2 ms. It means that after 1.2 ms (Clements et al., (2012)) the concentration in the synaptic cleft decreases by 37%. The glutamate concentration reached then 407 μM.

Several elements participate to the monitoring of glutamate within the synaptic cleft: the glutamate transporters and diffusion barriers. The glutamate transporters are proteins located at the membrane. They are sodium and potassium coupled transporters. EAATS are antitransporters. They exchange three molecules of Na+ and one molecule of H+ for one molecule of potassium and one molecule of glutamate (Tanaka, (2000)). They are located in Muller cells and presynaptic side. Their role is to decrease quickly the concentration of glutamate to avoid exocitoxicity. For instance the transporter GLAST is localized in muller cells (Otori et al., 1994)

and the transporter EAAC-1 is present in BCs of rats (Shultz and Stell, 1996). Muller cells might act as well as diffusion barrier as it was shown in photoreceptors (Rauen et al., (2000)).

However, the profile of glutamate concentration has never been studied in BCs. Using data from electron microscopy to determine the exact space between bipolar cells and how muller cells act as physical barrier would help to tackle the issue of spillover and to understand the profile of glutamate concentration at bipolar cells in response to a stimulus and to know whether the concentration of glutamate at neighbouring terminals is high enough for iGluSnFr to detect it.

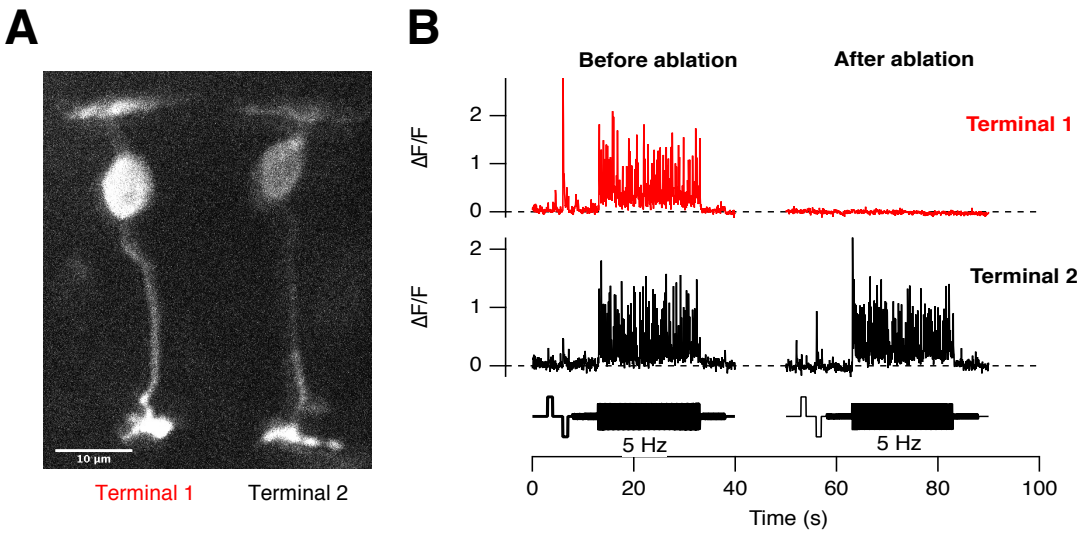

Figure 3.2. Laser ablation of the soma do suppress iGluSnFR responses.

(A) Picture of two BCs.

(B) Top: the soma of the BC connected to terminal 1 was photoablated. There is no iGluSnFR signals after laser ablation. Bottom: signal from terminal 2 which the soma was not ablated.

3.3.2. Glutamate release from different active zones can be distinguished.

During my experiments, I frequently observed two or more “release hotspots” within the same terminal (Figure 3.3.A.) which I hypothesise to correspond to different active zones of the same terminal. In the example of Figure 3.3. it is even possible to distinguish asynchronous release events between two simultaneously recorded areas (Figure 3.3.A.). The size of these iGluSnFR signals was about 1-2 μm, which is bigger than active zone in rod BCs observed with electron microscopy in zebrafish. Figure 3.4. shows an electron micrograph of a bipolar terminal (Figure 3.4.A.) in a 7 dpf zebrafish. In this example, the active zone size is 320 nm (Figure 3.4.B.). The measure from the Figure 3.4.B. might be just an estimation because there is a lot of variability among BC terminals morphology in zebrafish (Connaughton et al., 2004), but it seems to be around 300 nm. The spatial resolution of two-photon microscopy is not good enough to resolve structure <700 nm. However, since it was possible to observe different fluorescence peaks inside the same terminal with the dimension that is the same range as an active zone, these areas are likely to be distinct active zones from the same terminal. Hence using iGluSnFR, I can distinguish active zones separated by 1-2 μm (James et al., 2018).

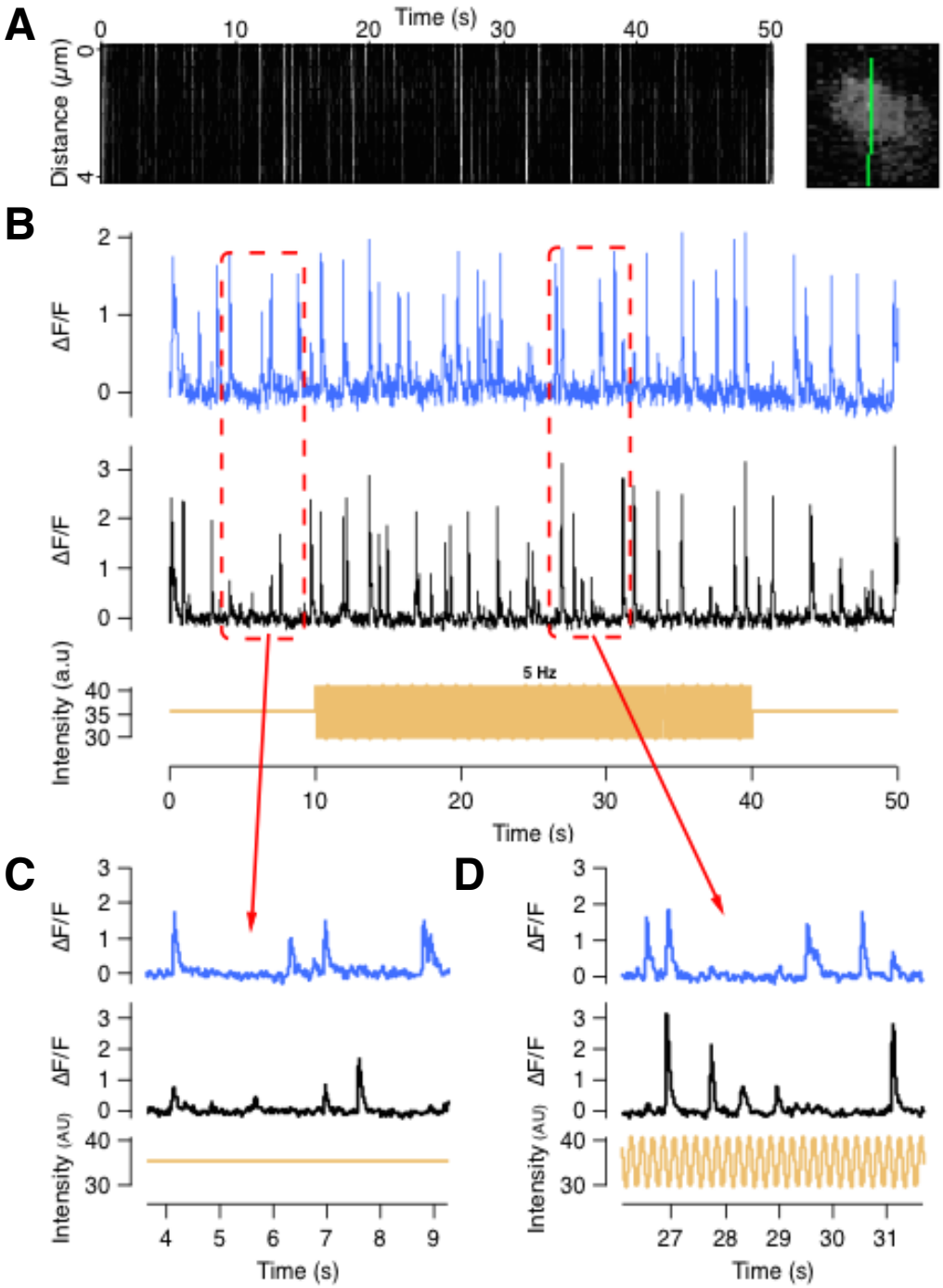

Figure 3.3. Recordings from different active zones in the same terminal.

(A) Example of a linescan with two active zones of the same synapse (right)

(B) Raw traces of two active zones of the same synapse (above (blue) and bottom (black)).

(C) Zoom in one area showing the upper active zone being active and not the lower active zone (red arrow).

(D) Zoom in one area showing the lower active zone being active and not the upper active zone (red arrow).

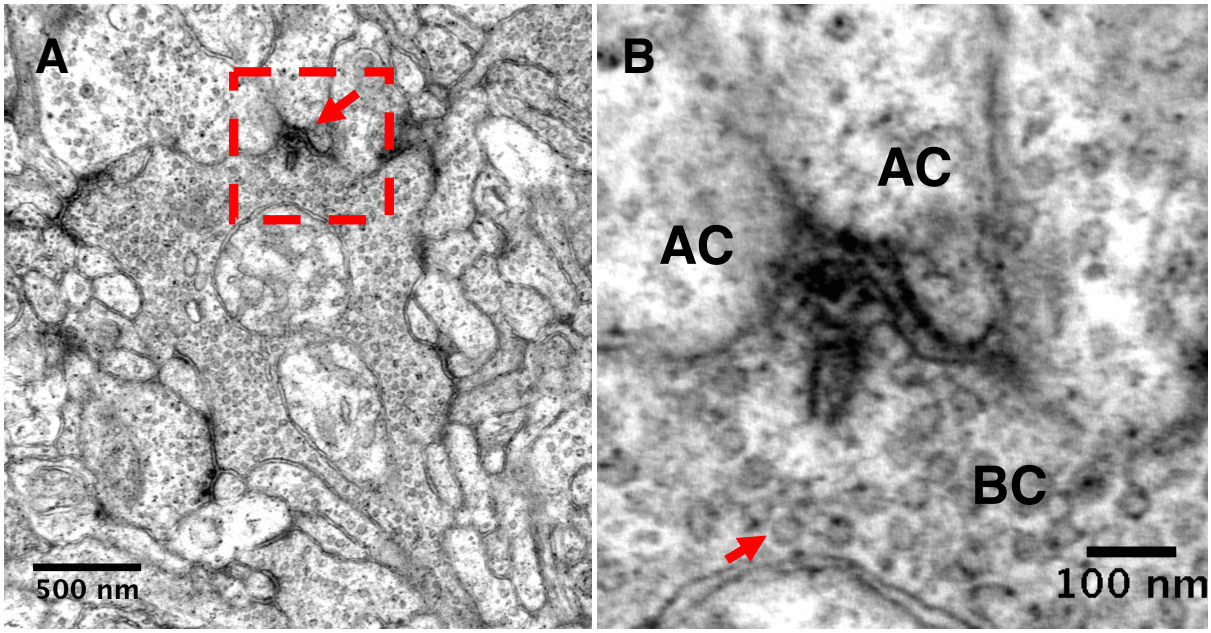

Figure 3.4. Micrograph of a BC terminal of a 7dpf zebrafish larvae. (provided from Rachel Wong's laboratory to Nachiket Kashikar).

(A) Overview of a BC terminal. The red dashed square indicates the terminal and the red arrows the ribbon synapse.

(B) Active zone from a ribbon synapse (from the overview presented in (A)). The red arrow shows an example of a glutamate vesicle. The active zone forms a dyad with the two neuronal targets. There are vesicles in the two structures that are facing the active zone indicating that they are likely amacrine cells. The size of this active zone is 320 nm.

AC: Amacrine Cell

BC: Bipolar Cell

To separate the signals from these two active zones, the fluorescence signals were demixed as follows: The ROI extraction from these two active zones was built with a diffusion model (see 2.3.1.). For each area, the maximum intensity was determined (supposedly where the vesicles of glutamate fused). Then the fluorescence signals around this maximum were averaged using a Gaussian fit (Figure 2.5.). The contribution of each data point to the average depended on its distance with the local maximum. The closer it was, the more contribution it had. Hence the signals further away from the active zone were not added to the ROI or had a minor input.
This indicated that the two active zones of the same terminal independently encoded the common stimulus (Figure 3.4.B.). One explanation for these different signals could be that the active zones were not recorded within the same plane. One active zone could be below the other one and the signal of this active zone could be weaker resulting in detecting less events. However, some events are missing in each active zone (Figure 3.4.C. and Figure 3.4.D.). Therefore, there was not an active zone that has a weaker signal then the other one and my data show that these active zones were not responding at unison reflecting the probabilistic release of vesicles.

3.3.3 Bipolar cells encode visual information with quanta of glutamate

Is it possible to detect the release of multiple quanta with the fluorescent reporter iGluSnFR? What could be the limitations of this reporter?
Several hypotheses could be considered concerning the issue of detecting multiple vesicles:
- the limitations of the reporter such as the kinetics could not allow to detect the unit of vesicle release. However, this is unlikely to present a limitation. iGluSnFR is present at the synapse at the level of the active zone. The concentration of free glutamate in the synaptic cleft peaks at 1.1 mM (Clements et al., 1992). The affinity of iGluSnFR is 4.5 μM (Marvin et al., 2013), hence, iGluSnFR should be sensitive enough to detect fusion of single vesicle.

- Another issue that could arise is whether iGluSnFR fluorescence is increasing linearly with glutamate concentration in the synaptic cleft. However, several evidences suggest that iGluSnFR is linear with increase of glutamate.
(i) Borghuis et al., (2013) showed that iGluSnFR fluorescence increases linearly with the presynaptic current. The fact that iGluSnFR signal does not saturate with the increase of stimulation indicates that glutamate concentration at BC synapse is within the linear dynamic range of iGluSnFR.
(ii) Marvin et al., (2013) Figure 1 shows several *in vitro* titrations of iGluSnFR signals against known glutamate concentration. It would be interesting to know the exact concentration of glutamate in the synaptic cleft of BCs. The concentration of glutamate inside the bipolar synaptic cleft is very difficult to evaluate and there is no study that provides insights about its spatial or its temporal profile inside the BC synaptic cleft. However, I observed that the fluorescence of the ΔF/F signal in BCs can vary from 0.15 to 3.5, which corresponds to signal amplitudes where response amplitudes as reported by Marvin et al., (2013) are linear.

To explore to what extent BCs use MVR *in vivo*, I recorded spontaneous activity from BCs (one example is presented Figure 3.5.). Figure 3.5.A. presents an example recording from a single active zone of a BC that exhibited a lot of spontaneous activity. Importantly, the event-amplitudes displayed substantial variability suggesting that each event could be constituted of a different number of vesicles. To obtain a better resolution regarding the events that could overlap and to remove the noise from the trace, a Wiener filter was applied to the recording (see Chapter 2.). “Events” were then extracted if they crossed a threshold (see Chapter 2). The event amplitudes in the deconvolved trace were plotted as a histogram to discern potential cluster of event amplitudes that could represent multivesicular events (Figure 3.5.B.).

This revealed several peaks and equal intervals (between peak center) indicating that all events might be composed of multiples of equal amplitude units, likely reflecting the single quantum. What constitutes a unitary event? the unitary events are likely to be the result of single vesicle fusion (see Chapter 3.1.). Moreover, the fact that the intervals between peaks are evenly distributed shows that each peak represents events with multiple vesicles.

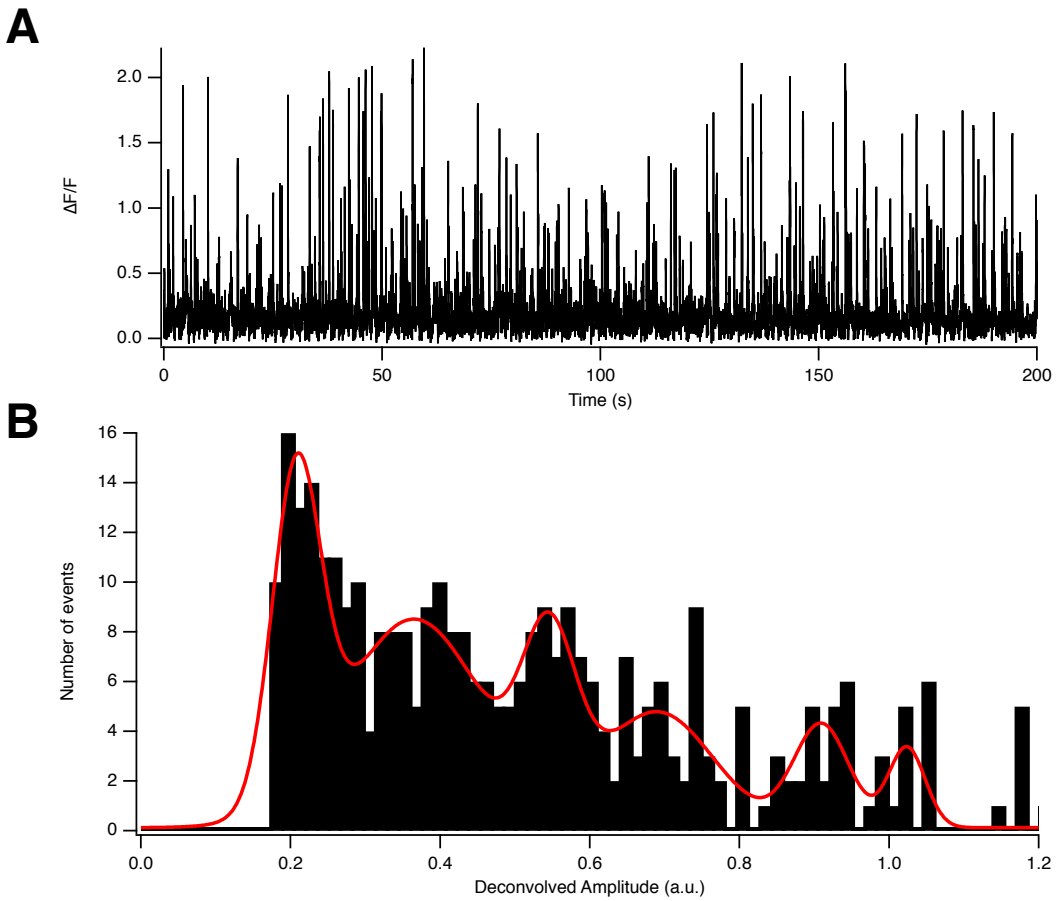

Figure 3.5. Example of spontaneous activity amplitude histogram.

(A) Raw trace of BC active zone of spontaneous activity.

(B) Amplitude histogram showing distribution of quantal events during no stimulation. This histogram was obtained with the method described in Chapter 2. Multiple Gaussian fits of the histogram is shown as red line.

Do BCs produce multivesicular events in presence of a visual stimulus? To obtain a large panel of event amplitudes, different contrasts were presented to the fish at 5 Hz (from 10% to 100%). Each period of stimulation lasted two seconds and was separated by two seconds of mean light to ameliorate adaptation effects. Figure 3.6. presents an example of a BC that was responding to a wide range of contrast (from 20%). I observed again that the glutamatergic signal amplitude varied. Moreover, at high contrast (for instance 100%), the amplitude was much higher than at low contrast (for instance 20%) (Figure 3.6.A., bottom), indicating that BC terminals might generate multivesicular events constituted of more events at higher contrast than at low contrast. The amplitude histogram for this recording (Figure 3.6.B.) reveals again multiple peaks with equals intervals between the peak centers. There are more peaks when a cell is stimulated (Figure 3.6.B.) compared to spontaneous activity (eight peaks against five respectively) (Figure 3.5.). The grey histogram (Figure 3.6.B.) was generated from the responses of the active zone at 40% contrast. It shows that one contrast is not encoded by only one type of multivesicular events but rather by a combination of multivesicular events containing a variable number of quanta. Importantly, Singer et al. (2004) estimated the number of quanta to 4 vesicles per event. In this example, multivesicular events contain up to 8 vesicles. Across all experiments, I observed that up to 12 vesicles could constitute a multivesicular event (Figure 4.6.A.). I also observed that nearly all the BCs generated multivesicular events (90/92 BCs presented in this thesis). Some BCs (2/92) showed responses that may not present coordinated MVR (see Chapter 4) although it was not possible to extract quanta from the two traces recorded. Hence, MVR is a general phenomenon among BCs.

In this chapter, I presented amplitude histograms that clearly show quantization. Another experiment that could be performed to confirm this point is to lower the concentration of calcium inside the BC terminals. Calcium is necessary to trigger the release of glutamate vesicles. Hence, modulating the calcium concentration could change the amplitude and the frequency of the events. If the small events that I observed were not uniquantal events, then decreasing the concentration of calcium

should change the shape of these events. Experiments were performed in Leon Lagnado's laboratory (data not published) using the neuromodulator substance P that inhibits the activation of L-type calcium channels in the BC terminals (Ayoub and Matthews, 1992). Substance P reduces both the amplitude and frequency of the events but does not alters the amplitude of the smaller events (the unitary events I used to analyse my data). Hence I conclude that the smallest events I observed were uniquantal events.

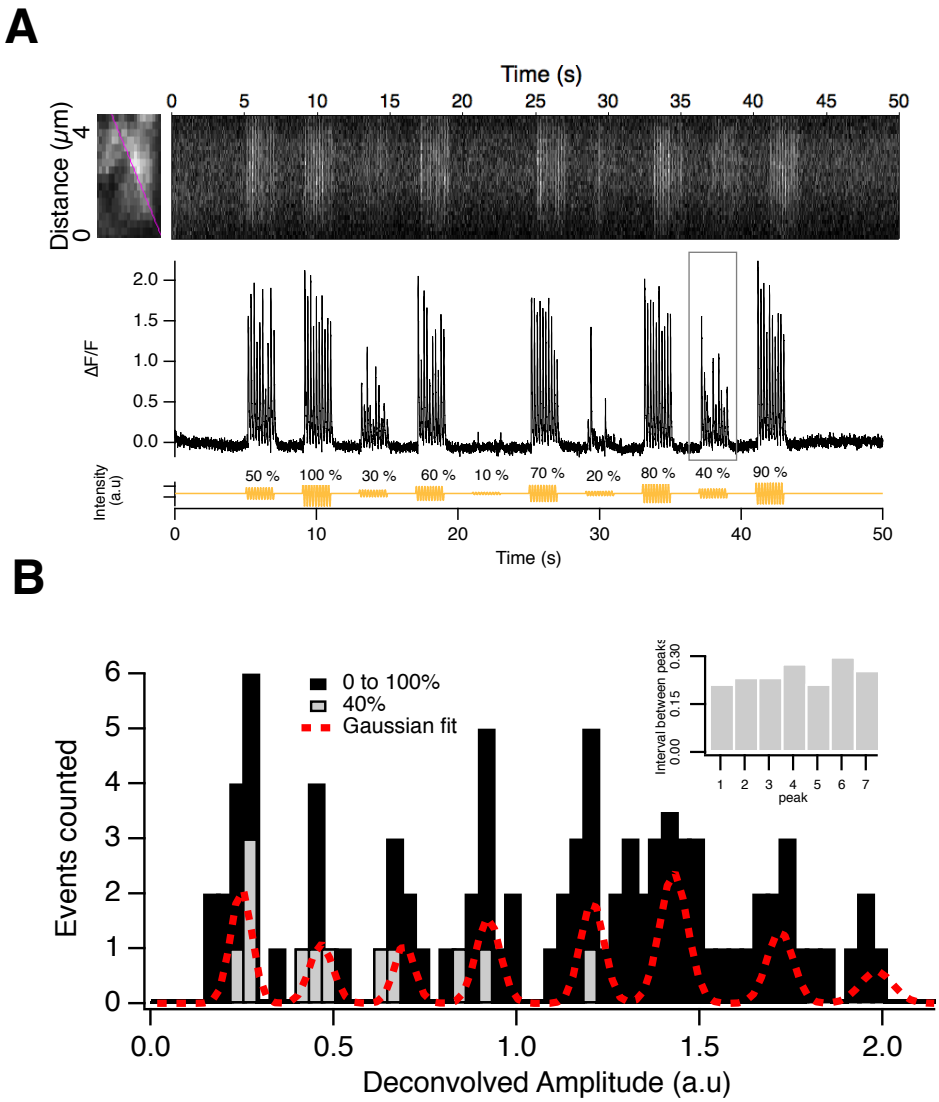

Figure 3.6. *In vivo* imaging of glutamatergic multivesicular release at BCs in the zebrafish retina.

(A) (top) Linescan recording of glutamate release at BC axon terminal (shown on the left) upon stimulation of various contrasts. (bottom) A trace of signal from a single active zone at the terminal. Stimulus pattern is shown at the bottom.

(B) A histogram of response amplitudes during various contrast stimulation (black bar) and responses during 40% contrasts stimulation (grey bar). Multiple Gaussian fits of the histogram are shown as dashed red line. Intervals of amplitudes between neighboring peaks in Gaussian fits are plotted in an inset.

3.3.4. The quanta that constitute the multivesicular events are released in a synchronous, coordinated manner

Each active zone may contain multiple release sites (Parsons and Sterling, 2003). The fusion of multiple vesicles might then originate from independent release sites. Could it be that multivesicular events that I detected (during evoked or spontaneous activity) originated from stochastic, coincidental superimposition of individual release of quanta?

Several studies suggested that the release of several vesicles by ribbon synapses was coordinated and not independent from each other (Mehta et al., 2013; Glowatzki and Fuchs, 2002; Singer et al., 2004). I decided to calculate the time between quanta within multivesicular events too. An example of a spontaneous activity trace is presented in Figure 3.7.A.. A terminal was recorded during 200 s to obtain enough events. The synapse was exposed to 5 min of light before the experiment to avoid adaptation effects. Due to the properties of the reporter iGluSnFR, it is impossible to distinguish individual events within a window below 11 ms (see 2.3.2.). Hence, it is not possible to resolve the release time interval between quanta within a multivesicular event if they occur at a shorter interval. Therefore, the time between events was binned into 10 ms intervals. The number of quanta were counted within 10 ms windows and the average time interval between quanta was calculated (0.42 s) by dividing the length of the recording (200 s) by the total number of quanta (385). If the vesicles were released independently, with the same probability, the time interval between quanta would be described by a Poisson process (with an exponential distribution). An exponential distribution was calculated with the same average of time between events (Figure 3.7.B.). The results from Figure 3.7. show that the time between quanta distribution is not described by a Poisson process. Hence, the vesicles were not released independently, in a random manner and the release of more than one vesicle is coordinated in BCs terminals (James et al., 2018).

Figure 3.7.B. indicates a refractive period where the probability of generating an event less than 20 ms after another one is zero (blue dashed line). This suggests that an active zone has a refractive period of around 20 ms before being able to generate another event (James et al., 2018).

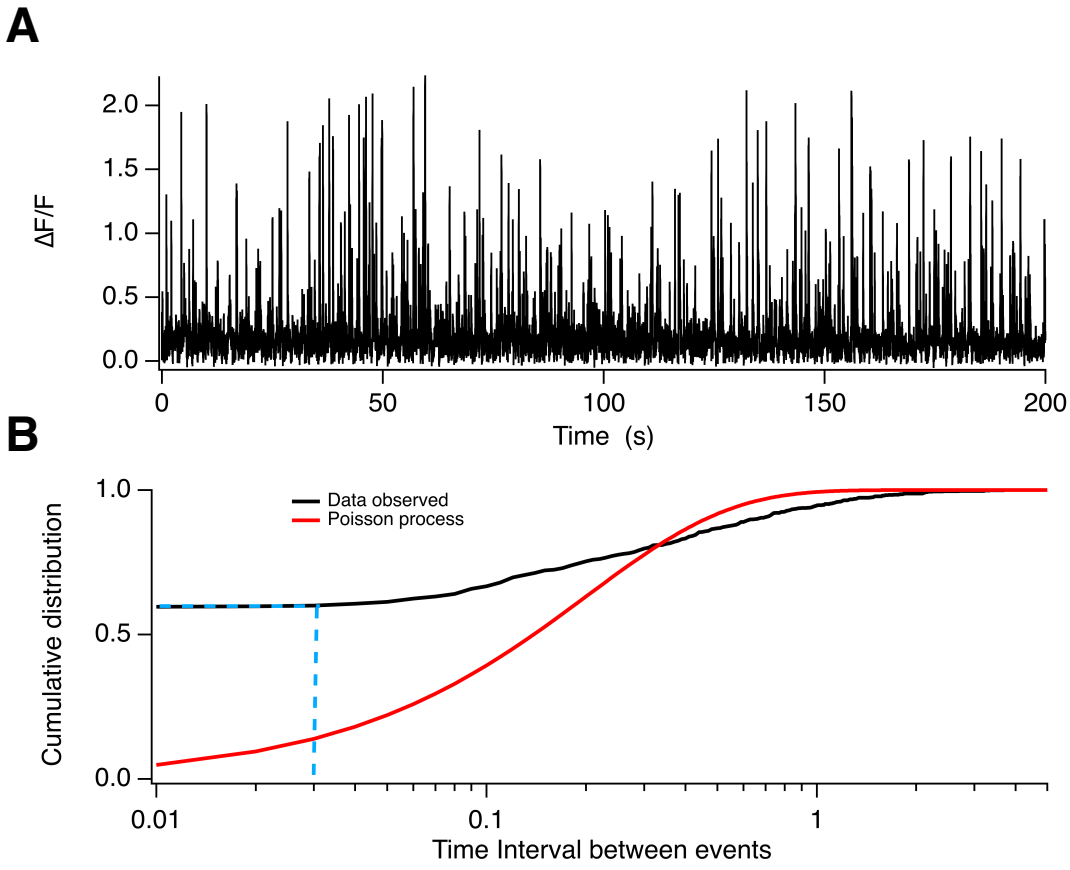

Figure 3.7. Multivesicular release is not described by a Poisson Process.

(A) Example of a trace with spontaneous activity.

(B) Cumulative probability of interevent time (black) of the raw trace (A) and an exponential cumulative distribution calculated from the parameters of the raw trace.

The dashed blue lines show that the probability of release fell to zero for at least 20 ms after a release event.

The results of this experiment were reproduced five times by other lab members (James et al., 2018)

3.4. Discussion

3.4.1. IGluSnFR is a good reporter to study MVR *in vivo*

I choose to use iGluSnFR (and SF-iGluSnFR) over other reporters to sudy MVR in BCs terminals. Other reporters such as SypHy were candidates to study glutamate release at BC terminals. As explained in Chapter1, Syphy is a pHluorin (GFP senstitive to pH) coupled with the synaptic vesicle protein synaptophasin. When SypHy is expressed in a neuron cell type, the pHluorin is located inside the neurotransmitter vesicles that have a pH of 5.5. Hence, inside the vesicles, the pHluorin does not emit fluorescence. When a vesicle fuses at the plasma membrane, the pH increases (it becomes to 7.5), triggering photons emission. The SypHy proteins are then endocyted, the pH decreases inside the vesicles and the pHluorin does not emit fluorescence anymore.

Hence, SypHy presented good characteristics to study vesicles fusion. However, a study in zebrafish revealed that the kinetics of SypHy are not fast enough to resolve precisely responses during a short stimulus. SypHy was already used to study BCS in zebrafish (Odermatt et al., (2012)). In this study, the authors studied the responses of BCs in response to 40 s visual stimuli. They calculated the number of average number of vesicles.s^{-1} (12 vesicles.s^{-1}). This number was similar to the one I obtained (17 vesicles.s^{-1}). The kinetics of SypHy are slower than iGluSnFR (recovery time with a constant of 3-7 s against 40 ms for iGluSnFR). At 5 Hz contrast, signals from SyPhy would have been difficult to interpret. The distinction between endocytosis and exocytosis could be challenging too. It seems difficult to resolve events that occurs at 5 Hz (Odermatt et al., (2012)). Moreover, the fact that endocytosis and exocytosis arises together makes the data difficult to interpret due to simultaneous increase and decrease of fluorescence. Moreover, the signal-to-noise ratio is lower than iGluSnFR (Odermatt et al. ,(2012)), detecting single vesicle events might be more difficult with SypHy than with IGluSnFR.

Other reporters based on IGluSnFR exist including SF-iGluSnFR variants (Marvin et al., (2018)). The variant I used is SF-iGluSnFR-A184A that has the same properties than the original iGluSnFR reporter (Marvin et al., (2013)) (Figure S4, Marvin et al. (2018)). As explained before, I used SF-iGluSnFR instead of iGluSnFR because due to less photobleaching (As observed by Marvin et al., (2018)) and the zebrafish line I used did not present silencing, which was a major improvement to perform my experiments (see Chapter 2). Marvin et al., (2018) showed that SF-iGluSnFR is brighter than iGluSnFR when expressed in the visual cortex of mice (due to a higher expression) and presents less photobleaching. Other variants for SF-iGluSnFR exist. Using a faster version of SF-iGluSnFR could help to decrease the minimum time necessary to distinguish two events (10 ms). However, Figure S4 (Marvin et al., (2018)) indicates that this variant saturates more than iGluSnFR, making it more difficult to resolve the number of quanta per event with this variant. Hence, SF-iGluSnFR-A184A is the best alternative to iGluSnFR.

The study from Marvin and al., (2018) presents other SF-iGluSnFR variants with different fluorescence such as green, yellow, cyan or blue. This could allow researchers to study *in vivo* the voltage, the calcium influx and the glutamate release of neurons by expressing three different sensors such as voltage sensors with a green fluorescence, GECIs (GCaMP or jRGECO) and SF-iGluSnFR with a yellow fluorescence.

3.4.2. Bipolar cells use MVR *in vivo*

In this chapter, I have shown that it was possible to detect quanta of glutamate at BC terminals in zebrafish larva *in vivo*. BCs generate MVR in response to a visual stimulus in a coordinated and synchronous manner. This is in line with the *ex vivo* study by Singer et al., (2004); BCs release 2-4 vesicles with electrical stimulation of BCs. However, it has been unclear whether BCs use MVR in physiological

conditions; MVR upon visual stimulation *in vivo*. I found that BCs release up to 12 vesicles per multivesicular event (I showed 8 vesicles per event in this chapter but see Chapter 4). Releasing vesicles in a synchronous manner is likely to have a higher metabolic cost than releasing vesicles in a graded manner or in an asynchronous way as in central synapses. What is an advantage of releasing several vesicles in one event? With this analogue code, BCs could encode a higher amount of information in one event. In theory, for one stimulation, a BC using MVR could generate a response with 12 possibilities against 2 for a neuron that releases only univesicular events. Therefore, a response from a neuron that uses MVR can transmit more information.

MVR is a critical advantage when neurons need to transmit information faster. By increasing the number of vesicle released in one event with stronger contrast stimulation, BCs transmit information about contrast strength in one event, whereas for spike coding neurons, it requires many spikes. In the next chapter, I will explore more about how BCs encode visual information (temporal contrast) with MVR.

MVR events are likely triggered by calcium transients. Are calcium spikes responsible for the MVR with higher amplitudes? One experiment that can directly link calcium spikes and glutamate release is to measure calcium and glutamate release simultaneously such as using a red calcium indicator such as jRGeco1a (Akerboom et al., 2013; Walker et al., 2013; Dana et al.,2016 ; Wu et al., 2014; Zhao et al., 2011). For this experiment, one has to take the difference in kinetics of two reporters into account such as rise time and decay time. However, simple experiments such as measuring amplitudes of calcium and glutamate changes in the same events would already be very informative.

3.4.3. Mechanisms for differences in the number of vesicles released among different active zones of the same terminal

Figure 3.3. shows different active zones from one terminal respond differently to the stimulus. What are the mechanisms of this differently behaving synapses in the same terminal? First this phenomenon can be a reflection of the probabilistic nature of vesicle release as described by Katz (1969). Indeed, Katz described the release of neurotransmitter depends on two probabilities. One is the probability with which a vesicle is located (or released) at an active zone site (or katzian release site) named katzian probability and the other one is the probability with which an excitation triggers a release at a synapse (that could contain several katzian release sites), named release probability (Stevens, 2003). For instance In BCs, an active zone (or a synapse) could be constituted of different release sites (that could coordinate the release of several vesicles quasi-simultaneously). The probability of release would be the probability to trigger a response and the Katzian probability would be the probability for each site to release a vesicle. The two probabilities might explain the difference between these two active zones. Vesicles tethered at ribbons that may be located differently or the number of vesicles within the pool vesicle available to be released varies from one active zone to another. Hence, two synapses can have different Katzian probabilities and respond differently to the same stimulus.

Another possibility is that the two active zones receive different inhibitory inputs. They can receive feedback from different ACs at proximal region of the active sites that modify the release kinetics. It might be that BCs are sending different signals to their neuronal targets. They could send outputs to different types of RGCs for instance.

3.4.4. Isolating IGluSnFR signals from individual active zones of BC terminals.

During my experiments, I observed several peaks of fluorescence representing distinct active zones in a terminal. I choose to record the brightest location where I could observe the strongest responses. However, it is possible that there are bleed through signals from neighbouring active zones due to the limitation of the microscope resolution. What is the probability to record two nearby active zones ? The problem is summarized in Figure 3.8..

One experiment I tried to localize the active zones during my experiments was to express iGluSnFR in the BCs in the background of ribeye-ribeyemcherry transgenic line. Ribeye-ribeyemcherry line expresses fluorophore mCherry coupled to the protein ribeye a which localises at active zones.

However, It was very difficult to do this experiment because of the photobleaching of mCherry. Here, I discuss other potential experiments that could localise more precisely the active zones and to determine what is the probability to record two active zones with a distance smaller than the spatial resolution of the microscope.

-The most precise way to measure the distance between active zones would be to perform electron microscopy experiments on the retina of zebrafish larvae. To look at the BCs population labelled with iGluSnFR, I could also express a probe that can be visualised under electron microscopy such as a membrane targeted peroxidase (Li et al., 2010) in the same BCs. This probe enables the recognition of the recorded cells with electron microscopy. It would be then possible to reconstruct terminals and to measure the distance between ribbons. This process would last several months and I did not have time to perform such experiments.

- I chose to use an immunochemistry method which is less time consuming. I performed a double immunostaining (one against GFP to label iGluSnFR positive cells and one against ribeye to localize the active zones of the terminals (James et al., 2019)(see Figure 3.9.). The number of active zones in a sample of 27 terminals

averaged 4.6 ± 2.4 (mean ± sd)(Figure 3.9.C.). The distance from one ribbon to its nearest neighbours averaged 0.96 ± 0.4 μm (Figure 3.9.D.).

How to calculate the probability of being sure to record individual active zones? One way is simulating a scan path at a terminal. With my immunostaining data, it is possible to know the shapes of BCs terminals and the distribution patterns of ribbons. Then, it would be possible to calculate the distance between a given scan path and the active zones, and to know if the distance is high enough to distinguish the two active zones (moreover, the spatial resolution of the two-photon microscope is known). By placing simulation scan path randomly, I could calculate the probability of collapsing multiple active zones as a single active zone.

-A third experiment could be done without modelling. It should be possible to perform first iGluSnFR recording on the BC terminals and then to perform immunochemistry against ribeye a as I explained before. By matching the same BC terminals in iGluSnFR recording images and in the immunostained images, I would know the exact position of each linescan relative to the position of the active zones. Hence, I could have a better estimation of the probability to record active zones that can be distinguish.

All the experiments presented above could be a good approach to calculate the distance between active zones, one limitation is that the protocol for immunochemistry or electron microscopy might slightly modify the structures of the terminals and the distances measured might be different from the distances between active zones in physiological conditions.

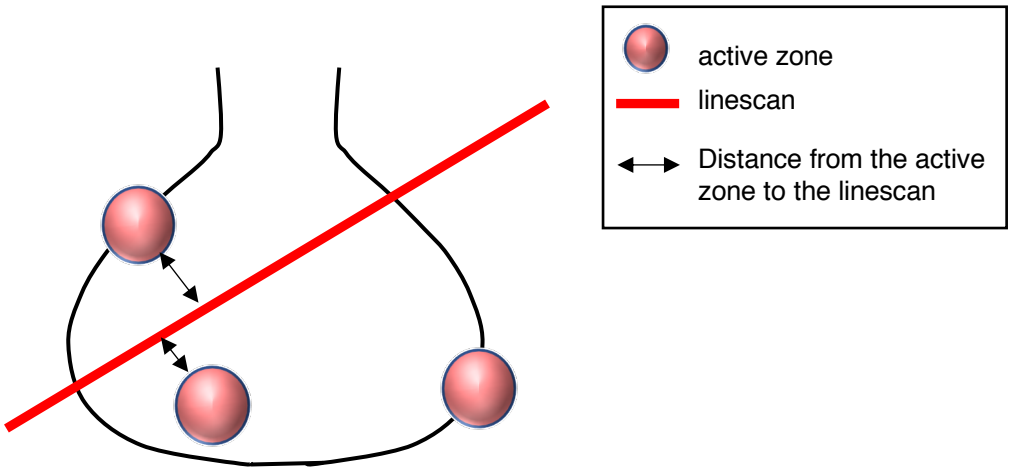

Figure 3.8. A schema of a linescan through a BC terminal with multiple active zones.
The linescan was realized where the response were the strongest. However, even it is unlikely (on average there are 5 active zones per terminal), I cannot rule out completely that I actually recorded active zones that cannot be distinguished from each other.

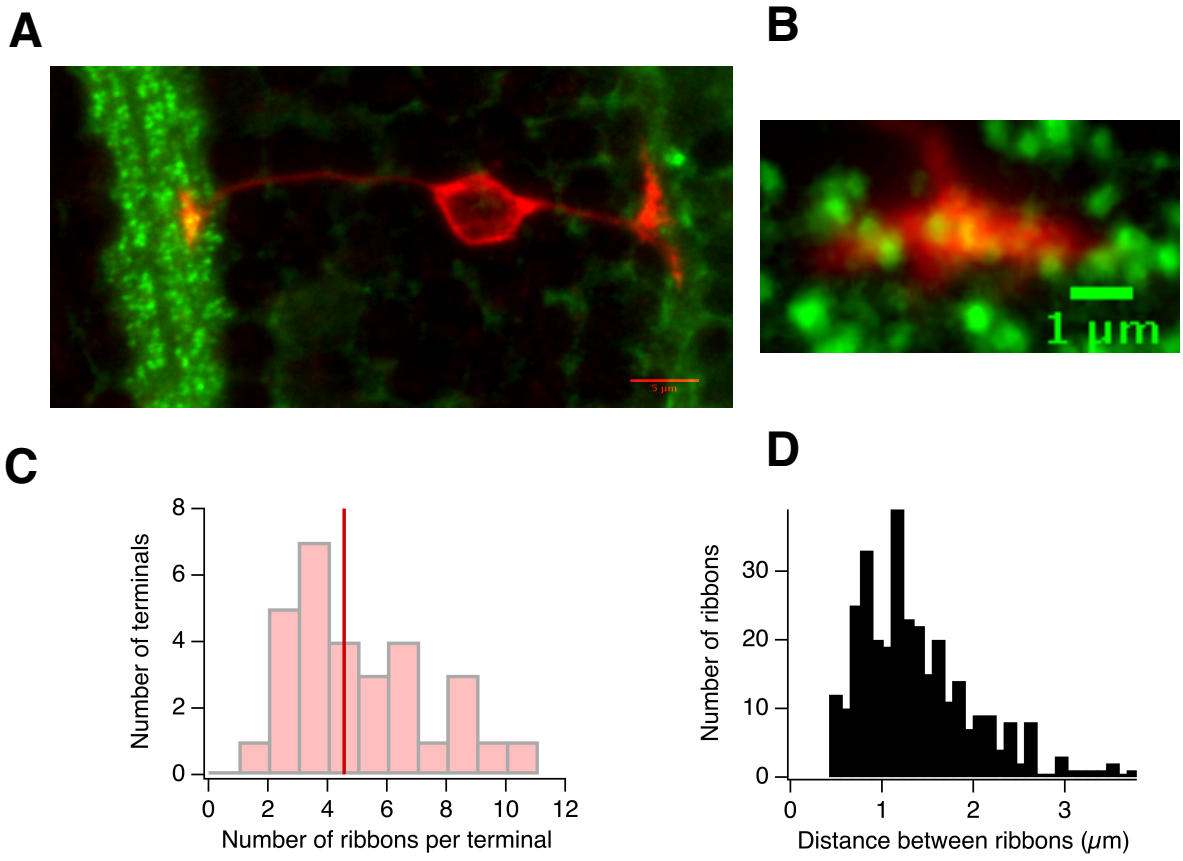

Figure 3.9. Counting active zones of bipolar cells terminals.

(A) Confocal image of a bipolar cell expressing iGuSnFR (red) and synaptic ribbons labelled with a ribeye a antibody (green). The image is a maximum intensity projection of the iGluSFR signal through a volume of 8.5 µm thickness. Note the ribbons scattered throughout the inner plexiform layer.

(B) Zoom in of the terminal from the cell shown in **a**. Note how the ribbons can be distinguished from each other. A threshold for the BC terminal signals was then applied to mask out ribeye a signals outside of the terminal. For each ribbon, the center was localised and the distances between the center of the ribbon and the centers of all other ribbons in the terminal were measured using FIJI (see Chapter 2).

(C) The number of ribbon per terminal of BCs (n=27 terminals). The number of active zones per terminal averaged 4.6 ± 2.4 (mean ± sd).

(D) Distances between ribbons from 27 BC terminals. The distances from one ribbon to all the others in the same terminal were averaged 1.36 ± 0.62 μm.

Chapter 4

The role of coordinated multivesicular release in the synaptic encoding of contrast

4.1. Introduction

In chapter 3, I showed that BCs generate MVR. How does MVR contribute to encode visual information? In this chapter I studied how MVR is produced to encode temporal contrast.

Contrast is a fundamental characteristic of the visual world. It represents the physical quantity of the luminance variation of a visual stimulus compared to the average level. Different types of contrasts can be defined: variation of contrast around space (spatial contrast) or variation in time (temporal contrast). Temporal contrast is a classical stimulus used to study sensitivity properties of neurons due to the modulation of photons number constitutes the visual message collected by the retina. For instance, fishes are animals that rarely stay still and they evolve in an environment that is moving around them. Zebrafish shoal live in a group with other zebrafish around them. Moreover, it has been reported in various species such as humans, monkeys and fish that eyes are constantly making saccades as they are rapidly changing focus to pay attention to different objects (Bianco et al., 2012; Beck et al., 2004). These saccades produce temporal contrast at the level of the eye. Thus, in natural conditions, visual stimulations in zebrafish environment involve rapid fluctuations of light intensity around a mean luminance that changes more slowly. Therefore, temporal contrast is a key feature of visual information encoded in the retina.

The brain processes temporal contrast in various ways. Some stimulation allowed to discriminate different classes of neurons based on their physiological response properties such as some neurons change response amplitudes or spike rates linearly or non-linearly to the contrast. Early on, flickers were used to study neurons from the visual cortex of cats (Movshon et al., 1978) and in the lateral geniculus of macaque (Derrington et al., 1984), marmoset (Solomon et al., 1999) or kissing gourami (Sakai et al., 1995). In several studies, some cells were able to respond at lower levels of contrast whereas some of them did not seem to

saturate (paravocellular cells in the lateral geniculate nucleus of the marmoset) (Solomon, 1999).

The role of the retina in visual information transmission may be different from the rest of the brain as the neurons in the retina are the intermediary between the environment and the brain. The visual information transmission in the retina is a balance between transmitting visual information as precisely as possible and conducting visual messages in a fast and efficient manner. Recordings from postsynaptic cells of photoreceptors such as HCs data in turtle (Tranchina et al., 1991) or goldfish (Spekreijse and Norton, 1970), and findings on BCs (Marmarelis and Naka, 1973) provided evidence to support the idea of linear graded glutamate release in photoreceptors. The signals from the photoreceptors are transformed afterwards by downstream neurons of the retina before being sent to the brain. Concerning RGCs, there are several evidences of nonlinearity in RGC responses to temporal contrast (Y cells in cat retina and other examples found in channel catfish or kissing gourami (Satai et al.,1995)), providing nice examples of gain control in RGCs. Where does this nonlinearity come from? Does it arise in BCs (not in the soma, because the responses to temporal contrast are linear, but at the level of the terminals) or at the level of RGCs?

Odermatt et al., (2012) provided an answer to this question by studying synaptic vesicle release *in vivo* in zebrafish using the reporter SypHy (pH indicator coupled with synaptophysin to target vesicles) (Granseth et al., 2006) in BCs. They concluded that BC terminals use quantal vesicular release to increase their sensitivity to contrast. However, due to the limitations of the SypHy sensor, some questions remained to be answered such as the kinetics of glutamate release. Also, SypHy reports a change of pH (linked to vesicle fusion) but not directly the glutamate concentration. To understand how visual information is encoded with such quanta, I used iGluSnFR (6% of the data) and SF-iGluSnFR (94 % of the data) reporter that has higher sensitivity and faster kinetics over SypHy and also gives a direct readout of the glutamate concentration. This allowed me to investigate more precisely how BCs use multivesicular or univesicular release to

encode visual information. A study about photoreceptors suggested that an increase of contrast triggered a rise of realease rate (Choi et al., 2005). I observed that BCs encoded temporal contrast in a more complex manner using both frequency and MVR. Another property of MVR could be explored: its temporal precision. It has been shown (in *ex vivo* experiments) that MVR has a higher temporal precision than uniquantal events (Li et al., 2014). Does MVR contribute to increase the information transfer efficiency in BCs?

I found that the majority of BCs encode temporal contrast with MVR (increasing the number of vesicles to be released simultaneously when the temporal fluctuation intensity increases). BCs also use frequency coding (increase of number of release events when the fluctuations of contrast increase) together with MVR. Moreover, I demonstrated that MVR increases the range of temporal contrasts that can be discriminated by glutamate release from BCs. Lastly, I found that MVR has a higher temporal precision compared to uniquantal events as shown in other systems. In the retina, time precision is crucial as in various cases, visually guided behaviours need a short time integration. Especially, RGCs receive inputs from several BCs such that temporally coordinated releases among BC populations is critical to maximize the amount of information encoded by RGCs.

4.2. Methods

Five seconds of constant light (Odermatt et al. 20012) followed by 30 s of contrast at different levels from 10% to 100% followed by 10 s of constant light was applied. As a temporal contrast stimulus, I used sine waves rather than square waves because it constitutes the elementary component to study temporal contrast. Indeed, squares waves can be described as a sum of sinusoidal waves (Shapley, 2009). Moreover, it has been shown that most of BCs are maximally sensitive at 5-7Hz (Rosa et al., 2016). Hence, I choose to use 5 Hz as the frequency of stimulation (see Figure 4.2. for an example of stimulation).

Spontaneous activity was calculated for 5 seconds after the stimulus delivery. For each average of quanta calculated, the activity during spontaneous activity was subtracted to measure how many quanta were used to encode each contrast. The Hill equation fitting was made using the software Igor. ON and OFF cells were discriminated using the time delay between the beginning of the response and the beginning of decreasing/ increasing contrast (Figure 4.2.1.).

Concerning the contrast discrimination (4.5.) experiment, as explained before, several contrasts separated by 2% were delivered in a random fashion (4.3.3.). Several quantities were then calculated such as the average event per cycle or the average quanta per event per cycle for each contrast.

In order to calculate the temporal jitter of the glutamatergic events (4.3.4.), I first calculated the vector strength, **VS** (Goldberg and Brown, 1969, Baden et al., 2011) for each multivesicular event:

$$VS_q = \frac{1}{N_q}\sqrt{\left(\sum_{i=1}^{N_q} cos\left(\frac{2\pi t_{q_i}}{T}\right)\right)^2 + \left(\sum_{i=1}^{N_q} sin\left(\frac{2\pi t_{q_i}}{T}\right)\right)^2} \qquad (11)$$

where $\mathbf{t_{qi}}$ is the time of the $\mathbf{i^{th}}$ q-quantal event, **T** is the stimulus period, and $\mathbf{N_q}$ is the total number of events of composed of q-quanta. The temporal jitter **TJ** can then be computed by:

$$TJ = \frac{\sqrt{2(1-VS)}}{2\pi f} \qquad (12)$$

where **f** is the stimulus frequency (5 Hz).

The Kmeans clustering from 4.3.3. was performed using the software IGOR PRO 7.01. The KMeans operation analyses the clustering of data using an iterative algorithm. The number of classes used with Kmeans was 4.

The recordings were analysed as described in 2.3.1.

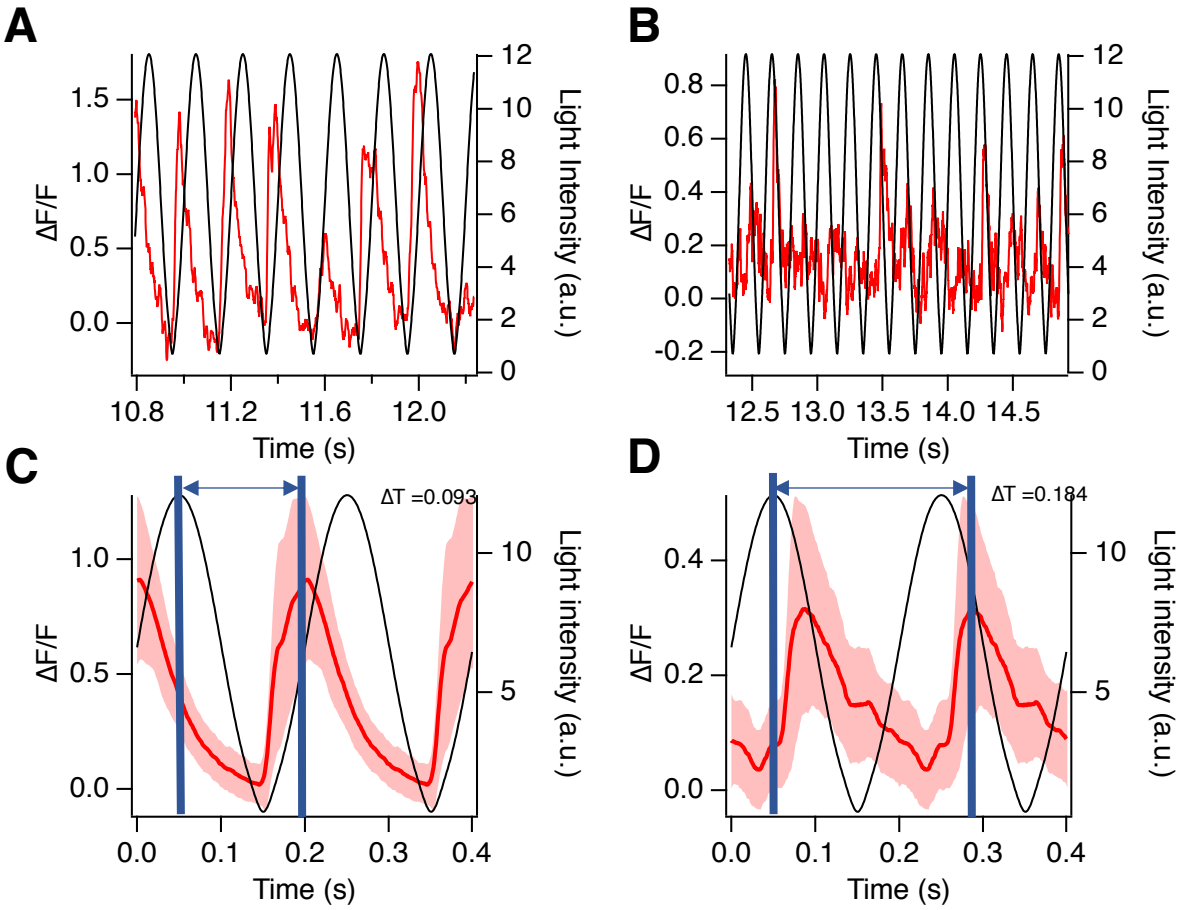

Figure 4.1. Distinction between ON and OFF cells analysis method.

(A and B). Examples of OFF cells and ON cells response (red trace). Stimulus waves are represented in black.

(C and D) Average of all the cycles (red trace) with the standard deviation (pink trace) and the stimulus (black trace) repeated twice. The blue lines indicate the beginning of the cycle. If delay to the peak of the response is greater than 150 ms, then the cell is responding to the rising phase of the cycle and the polarity of the cell is ON. (C) Example of an OFF cell. The delay is 93 ms. The phase of the cycle preceding the start of the response is a decreasing of contrast. Therefore, the cell responds to a decrease of contrast, It is an OFF cell. (D) Example of an ON cell. The delay is 184 ms. Hence, the cell is responding to increase of contrast, it is an ON cell.

4.3. Results

4.3.1. ON cells and OFF cells encode temporal contrast in a linear and nonlinear fashion

Odermatt et al. (2012) using the Syphy probe showed that OFF BCs use different strategies to encode temporal contrast. Using Hill equation to describe the neuronal responses, this study showed that some of the terminals were responding in a linear fashion whereas other were nonlinear. The authors explained that nonlinear synapses transmit more information but that linear synapses could transmit information at high contrast while nonlinear synapses saturate.

However, Syphy has a lot of drawbacks due to the low ratio of signal to noise and in the numbers of steps in estimating rate of vesicles release. I started my experiments with iGluSnFR and SF-iGluSnFR by using the same protocols as Odermatt et al. (2012). I then characterized further differences between ON and OFF cells and described how these two pathways were complementary to encode temporal contrast.

To compare temporal contrast sensitivities between ON cells and OFF cells, different contrast visual stimulations were applied to the fish (from 10 to 100%, Figure 4.2.). This allowed to study different phenomena such as encoding contrast or adaptation/ sensitization to the stimulus and it is possible to observe how BCs are encoding contrast with vesicles. A good description of the terminals' responses was obtained by fitting the response curves with a Hill equation (Figure 4.3.A-B.). The contrast **(R)** could be described with the following Hill equation:

$$R = \frac{C_{max}}{1 + (\frac{C_{1/2}}{C})^n}, \qquad (13)$$

Where $\mathbf{C_{max}}$ is the maximum contrast of the response, **n**, the Hill coefficient and $\mathbf{C_{1/2}}$ the contrast describing the half-maximal response.

This type of tuning curve is important to understand how sensory neurons transmit information about a stimulus. Neuron responses that are described by a Hill function showed a higher population coding efficiency thanks to the finest discrimination of individual neurons (Brunel and Nadal, 1998; Pouget et al., 1999; Seriès et al., 2004; Butts and Goldman, 2006). Moreover, the Hill function has been found to describe responses of photoreceptors to luminance (Boynton and Whitten, 1970; Normann and Perlman, 1979; Euler and Masland, 2000). It has been shown that photoreceptors have a Hill coefficient equal to 1. Moreover, BCs soma have a Hill coefficient equal to 1 as well reflecting a linear transmission of the input signals.

Some parameters of the Hill equation and can be useful to understand the behaviour of BCs terminals.

- When $C \ll C_{1/2}$:

$$(\frac{C_{\frac{1}{2}}}{C})^n \gg 1$$

Hence,

$$1 + (\frac{C_{\frac{1}{2}}}{C})^n \sim (\frac{C_{\frac{1}{2}}}{C})^n$$

Thus (from (13)),

$$R \sim \frac{C_{max}}{(\frac{C_{1/2}}{C})^n} = C_{max} * (\frac{C}{C_{1/2}})^n$$

The Hill coefficient **(n)** becomes the power law indicating how the responses increase as a function of contrast **(C)** and the $C_{1/2}$ which is the contrast describing the half-maximal response.

•

- when C=C1/2:

$$R = \frac{C_{max}}{1 + (\frac{C_{1/2}}{C_{1/2}})^n} = \frac{C_{max}}{2}$$

The response of the BCs is half the maximum, regardless of the Hill coefficient. It helps to indicate some notion of cooperativity in quanta release. I wanted to understand how quanta release could produce neuron responses that are described by a Hill equation.

At maximum contrast, OFF cells and ON cells were releasing 17 vesicles s^{-1}. This measurement is similar to what was observed before (Odermatt et al., 2012, Freed, 2000).

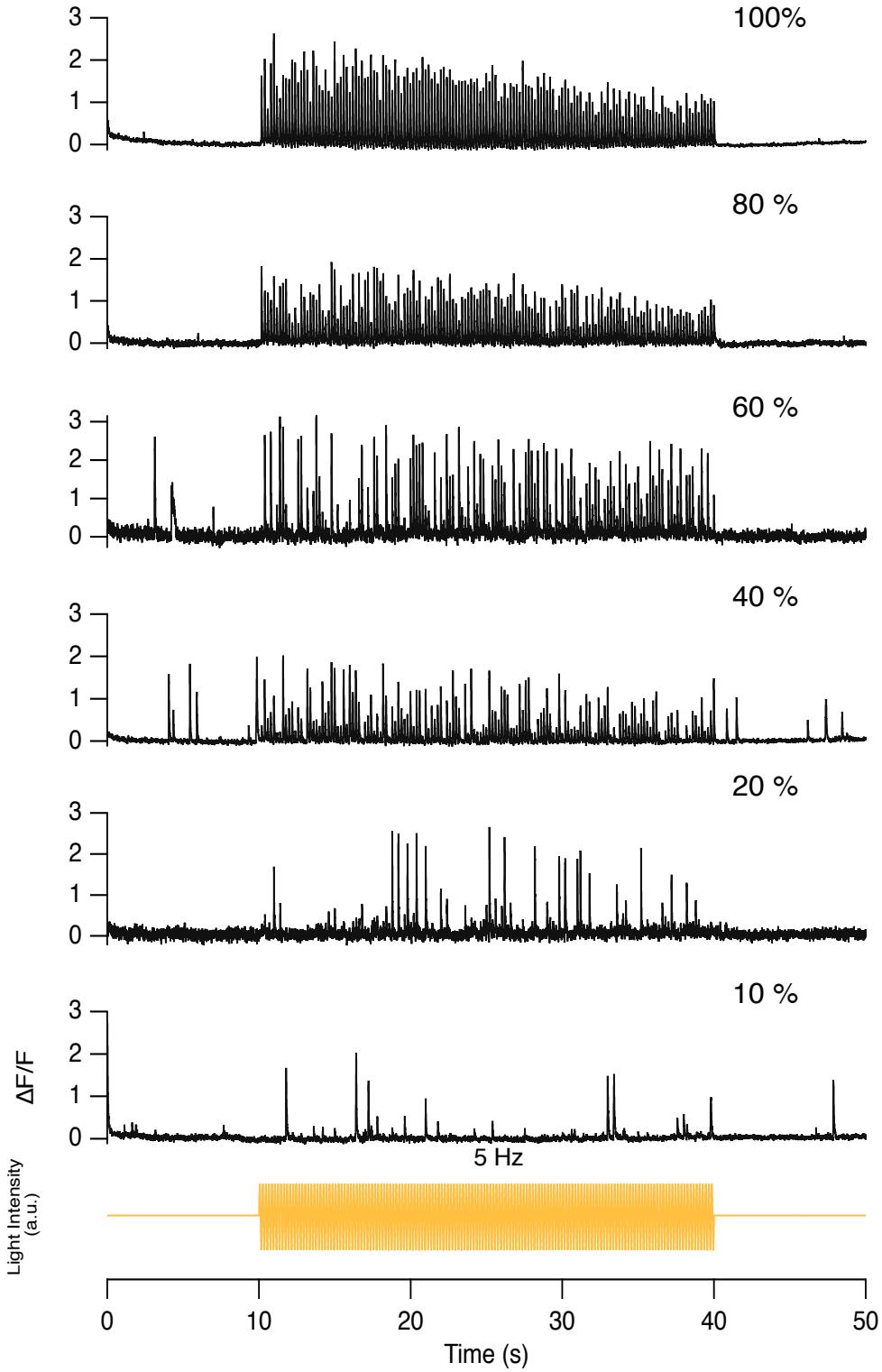

Figure 4.2. Example of a terminal responding at different contrast at 5 Hz.

From top to bottom: 100%, 80%, 60%, 50%, 40%, 20%, 10%). The stimulus is represented by the yellow trace (bottom).

Here, the BC terminal responded to different contrasts from 10% to 100%. The terminal adapts at 100%. Also, the terminal does not respond to each cycle below 60%. Moreover, the amplitude of responses seems higher at 60 % (several times the ΔF/F is around 3). This could be explained by the fact that the releasable pool of vesicles is always full when there is a response at 60% whereas when the terminal is responding at each cycle (80% and 100%), the pool of vesicles is not refilled completely before the next response. I quantified the responses of different terminals to contrast by calculating the average of quanta per cycle and by fitting the responses with a Hill equation.

Figure 4.3. presents the results:

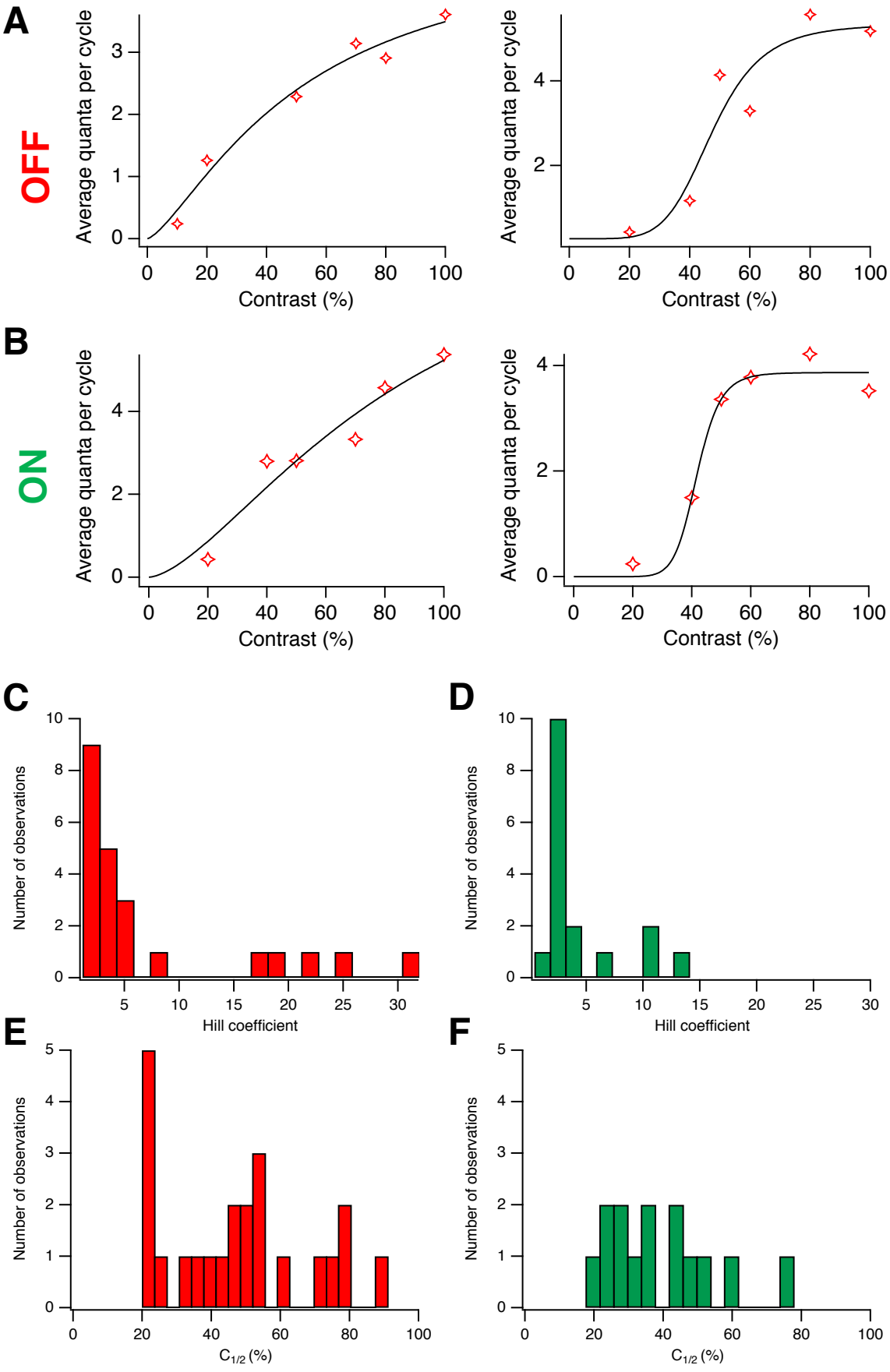
A
OFF
Average quanta per cycle
Contrast (%)
B
ON
Average quanta per cycle
Contrast (%)
C
Number of observations
Hill coefficient
D
Number of observations
Hill coefficient
E
Number of observations
C1/2 (%)
F
Number of observations
C1/2 (%)

Figure 4.3. ON cells are more sensitive to temporal contrast than OFF cells.

(A,B) Examples of contrast sensitivity traces for ON and OFF cells. Curves are fit to the Hill equation. The red crosses represent the data point and the black trace the Hill equation fit.

(C,D) Values of Hill coefficient for ON cells (n=17) (mean = 4.66 $\pm$ 1.2) (C) and OFF cells (n=23) (mean = 8.9 $\pm$ 2.7)(D).

(E,F) Values of $C_{1/2}$ for ON cells (mean = 51.2 $\pm$ 6.9%) (F) and for OFF cells (mean = 42.9% $\pm$ 4.3%)(E).

The curve has a sigmoid shape with a C_{max} that varies from synapse to synapse. For instance, in Fig. 4.3. A. on the right, the saturation occurs at 70-80%. How to explain this saturation? It could be due to external factors such as feedback inhibition from ACs, due to a saturation of the receptors at the levels of the BC dendrites or due to the fact that the maximum number of vesicles that can be released has been reached. It could also be limitations due to the ribbon size or the size of the fusion site for instance.

Figure 4.3.C. and 4.3.D. show $C_{1/2}$ for ON (n=17) and OFF cells (n=23). This shows that ON and OFF cells have similar $C_{1/2}$ on average (42.9% $\pm$ 4.3 for OFF cells and 51.2% $\pm$ 6.9 ON terminals 51.2% $\pm$ 6.9). However, the OFF cells have a broader distribution compared to ON cells.

Figure 4.3.E. and 4.3.F show the distribution of Hill coefficient for ON cells and OFF cells. OFF cells have a higher range of values whereas ON cells seem to be part of one group. Moreover, I found linear cells in OFF and ON cells (Hill coefficient <1.5). Although it seems that there is a higher diversity concerning OFF cell responses these results are not significant and more data are required to draw solid conclusions.

4.3.2. Bipolar cells increase the number of quanta per event to encode higher contrasts

A fundamental issue is to understand how BCs encode visual information with quanta and what the role of MVR in encoding contrast is. BCs could increase the number of events, the number of quanta per event or fire in a synchronous fashion to increase the global input onto RGCs. For the first time, I was able to address these issues *in vivo* with direct measurements of glutamate release.
What are the mechanisms that are underlying the variation of vesicle release with the increase of contrast? BCs release quanta of neurotransmitters and are capable of releasing several vesicles almost simultaneously. Some of the

reasons that explain this phenomenon is that BCs could release more events per stimulation or increase the number of quanta released per event (MVR).

To understand the importance of multiquantal events versus event frequency in encoding contrast, the proportion of different multiquantal events was calculated from the preceding experiment. Each multiquantal event was counted and then divided by the total number of events. Figure 4.4. and 4.5. show two examples for ON cells and OFF cells. BCs presented in Figures 4.5. A, B, C and Figures 4.5.A, B, C were the examples that the amount of multiquantal events does not vary with the increase of the contrast. The bottom parts of Figures 4.4. and 4.5. (Figure 4.3.F.) illustrate examples of OFF cells and ON cells that increase the proportion of quanta per event. For instance, Figure 4.5.F. shows an example of an ON cell where the peak at 100 % is at 4 quanta whereas the peak for OFF cells (Figure 4.4.F) is at 7 quanta per event. These examples reflect the majority of cells that I observed.

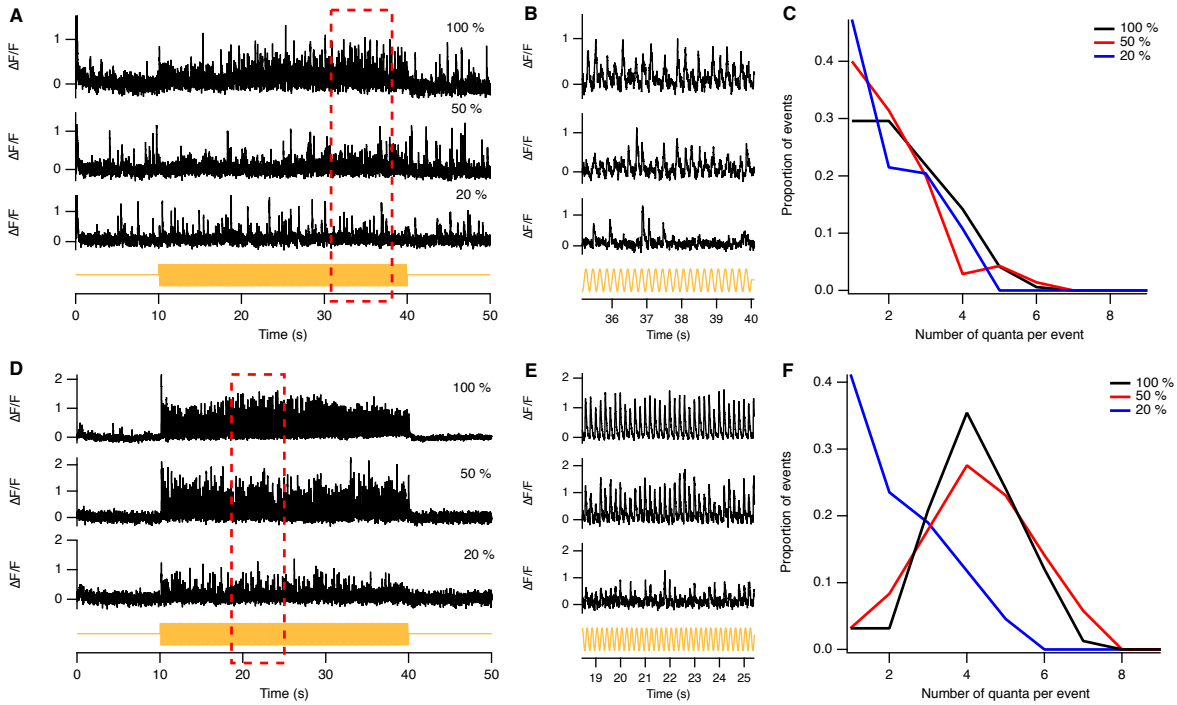

Figure 4.4. Different types of multiquantal event distribution in ON cells.

(A) Traces of SF-iGluSnFR signal in a BC terminal with different temporal contrast stimuli (100 %, 50 % and 20 %) at 5 Hz (yellow trace). Note that this example shows at 20%, the events amplitude do not seem lower than at 100%.

(B) High-magnification of traces from a region indicated by the box with dashed red line. Note that the amplitude of the events at lower contrast is the same than at higher contrast.

(C) Analysis of the event amplitude for the example presented in (A). The average amplitude of events at different contrasts does not vary.

(D-F) This example underlines that the amplitude of events at different contrasts varies. Note the higher proportion of 4-5 quanta events at 100%, 50% compared to 20% where the uniquantal event is the majority.

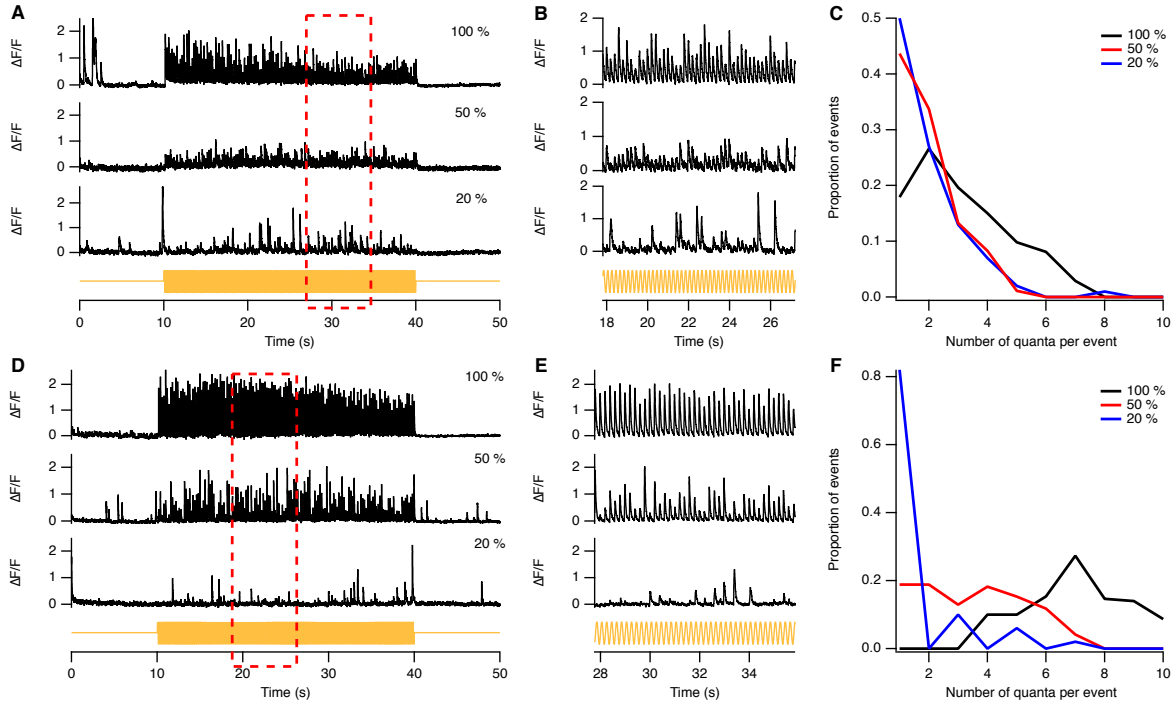

Figure 4.5. Different types of multiquantal event distribution in OFFs cells.

(A) Traces of SF-iGluSnFR signal in a BC terminal with different temporal contrast stimuli (100 %, 50 % and 20 %) at 5 Hz (yellow trace). Note that this example shows at 20%, the events amplitude do not seem lower than at 100%. The amplitude of events at different contrast does not vary as seen in the plot for the proportion of multiquantal events.

(B) High-magnification of traces from a region indicated by the box with dashed red line. Note that the amplitude of the events at low contrast (20 %) is the same than at high contrast (100%).

(C) Analysis of the event amplitude for the example presented in (A). The average amplitude of events at different contrasta does not vary.

(D-F) Another example of an OFF terminal presenting a different distribution of multiquantal events. This example underlines that the amplitude of events at different contrasts varies.

A summary of all the ON and OFF cells is presented in Figure 4.6. I then divided the OFF and ON cells into two categories. For each BC type, I could observe some that increase the number of quanta per event when the temporal contrast increases. However, some others did not increase the number of quanta per event. The average number of quanta per cycle (Q_C), the number of events per cycle (EC) as well as the number of quanta per event per cycle (Q_e) across trials were calculated.

These three quantities are linked by the following equation:

$$Qc = Qe * Ec \tag{14}$$

where ***Qc*** is the number of quanta per cycle, ***Qe*** is the number of quanta per event and ***Ec*** is the number of events per cycle.

Figure 4.6. indicates the proportion of multiquantal events for ON (n=18) and OFF cells (n=33) at different contrast intensity (100%, 50% and 20%). ON and OFF cells are increasing Q_e when the contrast increases. The maximum of Q_e is higher at 100% (12 for OFF cells and 8 for ON cells) compared to 50% (10 for OFF cells and 7 for ON cells) or 20% (8 for OFF cells or 7 for ON cells). OFFs cells are releasing more Q_e than ON cells at 100% and 50% (Figure 4.6.A and B). There are no differences between ON and OFF cells at 20% (Figure 4.6.C). Differences between ON and OFF cells can be quantified by calculating the average of Q_e for each cell (Figure 4.6.D). OFF cells are releasing more Q_e on average (3.4) than ON cells (2.45) ($p < 0.02$). Another interesting information is to look at the distribution of the average of Q_e. It seems that ON cells are grouped into one group whereas OFF cells are grouped into two groups: one that might be similar to the group of ON cells and the other one uses a higher number of quanta per event. A clustering method could be performed to identify such clusters.

To compare with event frequency, the average of E_c (of temporal contrast) for ON and OFF cells was analysed (Figure 4.6.E.). ON cells use more event rate (E_c) to encode signals compared to OFF cells: the average of E_c for ON cells is 1.69 where the average for OFF cells is 1.24 ($p < 1.01$). Overall, this could indicate

that ON cells use more event rate whereas OFF cells use more MVR to encode temporal contrast. Moreover, by observing more closely to the ON distribution, it looks like the ON cells are distributed into 3 groups revealing perhaps physiological distinct groups of ON BCs.

Overall, this data suggests that OFF cells use a larger number of quanta than ON cells to encode temporal contrast. Hence, I showed that in some cases, BCs are using MVR to encode contrast whereas in some cases, MVR does not seem to prevail upon event rate as it seems in ON BCs.

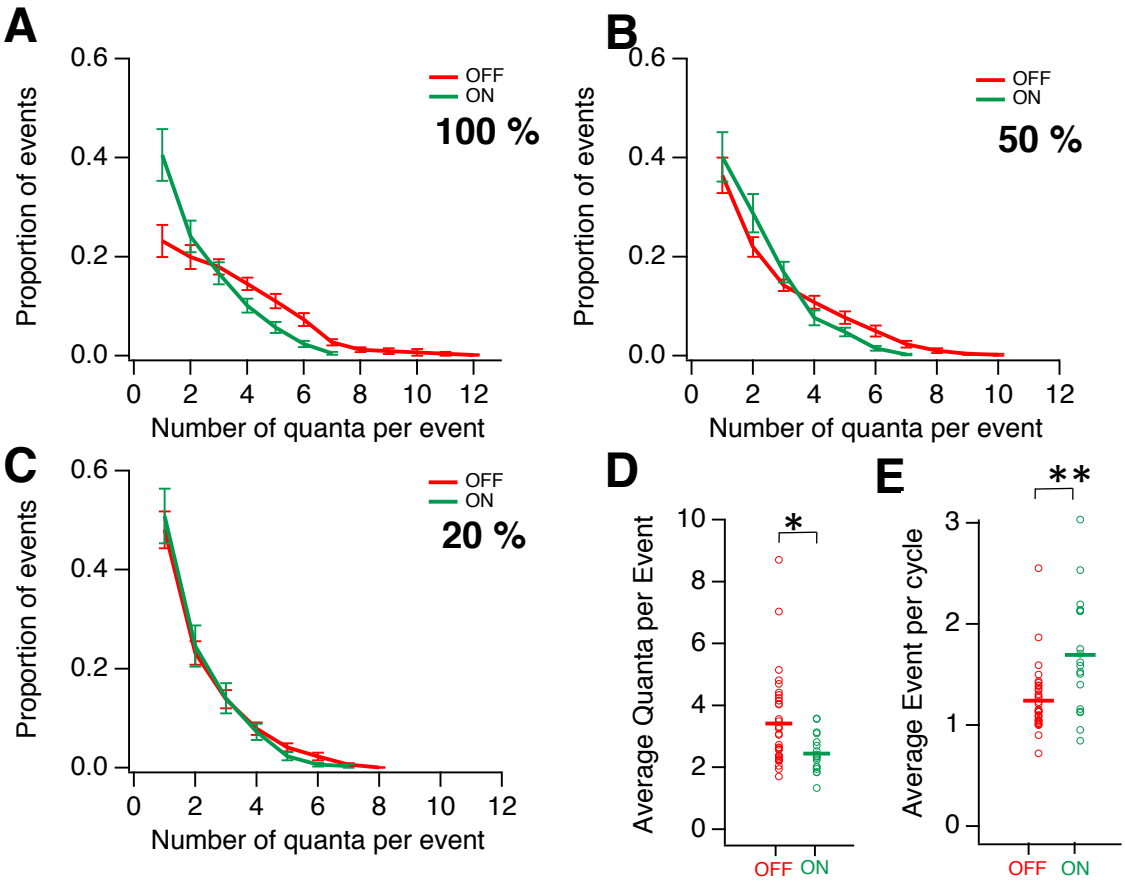

Figure 4.6. Proportion of quanta per event with different contrasts.

(A, B, C) The average proportion of Q_e for ON (n=18) and OFF cells (n=33) at different contrasts: 100 % (A), 50 % (B), 20% (C). (D) The average of Q_e for OFF and ON cells at 100 %. (E) The average of E_c for OFF and ON cells at 100 %. Note that OFF cells have higher number of Q_e compared to ON cells whereas ON cells have a higher number of E_c. *: $p < 0.02$, **: $p < 0.01$. Error bars: S.E.M.

4.3.3. Bipolar cells use MVR as well as event rate to encode temporal contrast

A limitation of the experiment presented before is the fact that there are different types of BCs. I can measure responses at different contrasts for each BC but it is more difficult to compare responses to increase of contrast because different BCs respond differently to contrast: they can start to respond at different intensities or they can adapt or sensitize at different time scales. To study them, it would be interesting to have a point of comparison for every BC. A similar feature for most BCs could be the half contrast response, the contrast where the response of BCs is half its maximal response. This $C_{1/2}$ could be used as a reference point for each BC terminal. The BCs can be compared afterwards by comparing their responses around this value. I can then apply to this terminal a range of contrasts around this value. This is what I used to design the experiment described above.

The principle of this experiment is the following one: BCs can use two strategies to encode temporal contrast with a modulation of the quanta number. They can increase the number of quanta per event (thanks to MVR) or they can modulate the number of events per stimulation (frequency coding). However, it is difficult to compare BCs by comparing according to responses for different contrasts because they are responding differently to contrast. However, for most of them, their tuning curve is described by a Hill function and each of them is characterized by their $C_{1/2}$. Thus, by using $C_{1/2}$ as a reference value for each terminal, it becomes possible to compare them.

The design of this experiment is summarized in Figure 4.7. The midpoint (which is $C_{1/2}$) is estimated using a stimulus of different contrasts. Subsequently, fish were presented with several steps of contrasts that consisted of randomized sequences of different contrasts around the midpoint. Two different randomized sequences were used and alternatively presented to the fish. The average number of quanta per cycle (Q_c), the number of events per cycle (E_c) as well as

the number of quanta per event per cycle (Q_e) were calculated again across trials (see 4.3.2.). To compare different terminals between them, each trace was normalized with the first value. The average Q_e represents the amplitude coding and the part that MVR is playing in encoding temporal contrast. The mean of the E_c corresponds to the contrast coding by event rate (frequency coding), the mean of the Q_e reflects the role of MVR in encoding temporal contrast. The average Q_c is the quantity of vesicles that the postsynaptic neuron (ACs or RGCs) will receive. At least 5 trials were recorded to calculate each average (Figure 4.8.). Figure 4.8. illustrates with two examples (one example for ON cells (Figure 4.8.B). and one example for OFF cells (Figure 4.8.A.) how BCs use both MVR and event rate to encode temporal contrast. The output of the BCs (total number of Q_c) results from a combination of MVR and event rate (see ***(14)***). This output enables to distinguish a higher number of contrast steps than the event rate or MVR.

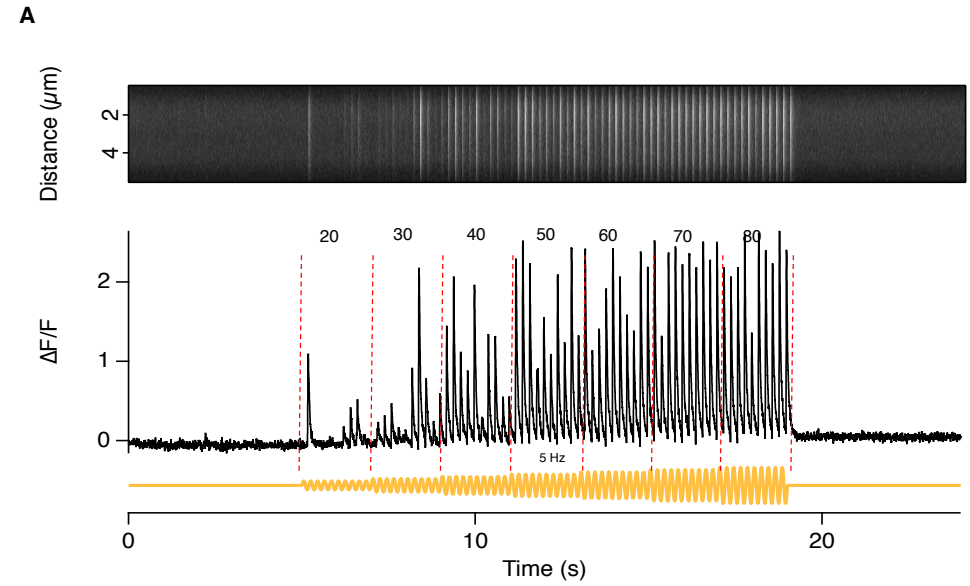
A
Distance (μm)
2
4
ΔF/F
20
30
40
50
60
70
80
2
1
0
5 Hz
0
10
20
Time (s)

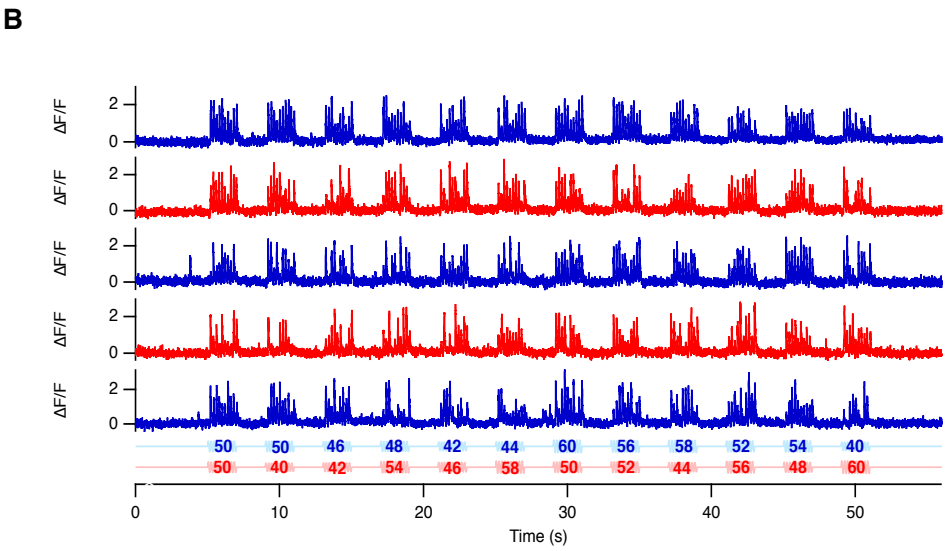
B
ΔF/F
2
0
50 50 46 48 42 44 60 56 58 52 54 40
50 40 42 54 46 58 50 52 44 56 48 60
0
10
20
30
40
50
Time (s)

Figure 4.7. Steps of the experiment that test how bipolar cells are encoding temporal contrast.

(A) To investigate the vesicle code operating at ribbon synapses of BCs, we applied full-field stimuli of varying contrast at 5 Hz. Top: linescan of a BC terminal over time. Bottom: temporal profile of the line scan. The stimulus is represented at the bottom of the figure (yellow trace).

(B) The contrast at which the increase of the responses compared with those at the previous lower contrasts is the highest was chosen as 'midpoint'. Contrast stimulations that are differing by 2% were presented for 2 s to examine the smallest contrast differences that BC can distinguish around the midpoint. We used two protocols in which the sequences of different contrasts were differently randomized. The stimuli for the two protocols are represented in blue or pink traces at the bottom of the graph. The red traces are the responses to the pink stimulus trace and the blue traces are the responses to the blue stimulus trace. The numbers on the stimuli traces indicate the contrasts that were presented. The first block of 2 s contrast was used to adapt BCs to light stimuli and the response during the second to the last blocks of contrasts were used for analysis.

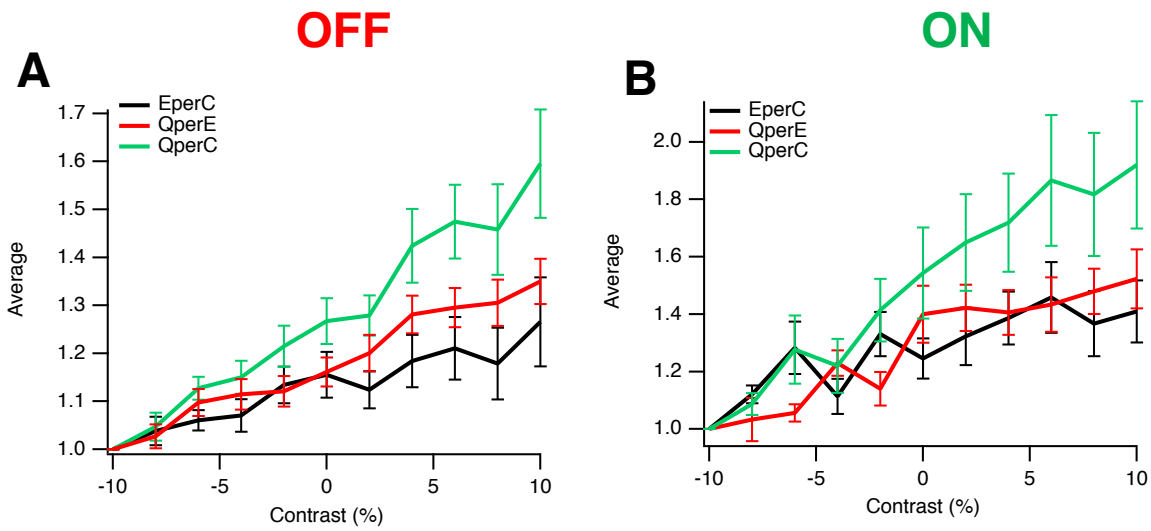

Figure 4.8. MVR contribution comparison between ON and OFFs cells.

(A) The average quanta per cycle, event per cycle, and quanta per event at different contrasts. OFF cells encode temporal contrast by event per cycle and quanta per cycle (n=17).

(B) Both event per cycle and quanta per event contribute to encode temporal contrast in ON cells. Note that the slope of the traces for ON cells is higher than those for OFF cells (n=7).

Error bars: S.E.M.

To understand how BCs are using event rate versus amplitude to encode increase of contrast, I separated ON and OFF cells into two clusters using the Kmeans algorithm (see 4.2.). It appears that some cells are using more amplitude rather than event number to encode temporal contrast (Figure 4.7.). 23% ON cells have a higher average of quanta per event compared to events per cycle. Thus, the majority of ON cells (77%) encode temporal contrast mainly with the event rate whereas 45% of OFF cells encode variation of contrast principally with MVR. This reflects what was presented before (Figure 4.3.4.): ON BCs are using more vesicle release rate to encode temporal contrast compared to OFF cells. Another interesting observation is that the cells that are encoding temporal contrast mainly with event rate are less performant and noisier that the ones using primarily MVR (Figure 4.3.7.B. and Figure 4.3.7.D.) and the discrimination range of temporal contrast intensity seems lower.

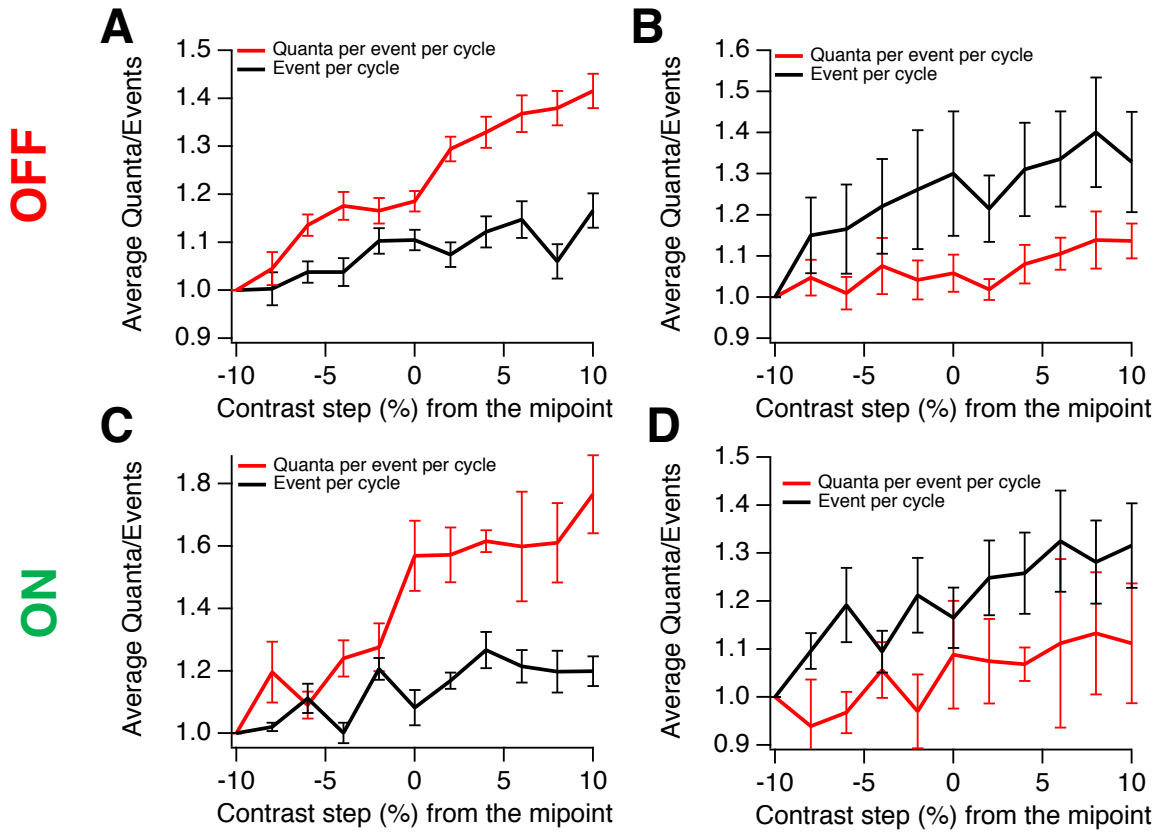

Figure 4.9. Bipolar cells are grouped into two types based on encoding to temporal contrast with event rate and MVR.

(A,C) The average event per cycle and quanta per cycle in OFF (A) or ON (C) BCs that use MVR as the main factor for contrast discrimination.

(B,D) Plots for OFFs (B) or ON (D) BCs that use the event rate as the main factor in temporal contrast encoding.

All the values are normalized using the first value (at -10% from the midpoint).

Error bars: S.E.M.

Moreover, we know from 4.4. that OFF cells have a higher proportion of multivesicular events compared to ON cells and that OFF cells are encoding higher temporal contrast by increasing the number of quanta per event. The results from Figure 4.8. verify these observations. OFF cells have a higher tendency to encode contrast more with MVR compared to ON cells.

I also observed some ON cells were responding to the visual stimulus in a linear fashion (Figure 4.9.) (n=2). These cells are located in the layer s6 of the IPL and could be mixed BCs. The recording of figure 4.9.B shows that this cell type can increase or decrease its release of glutamate. This type of cells has been described in goldfish as well (Baden et al., 2014). I did not observe many cells of this type. It might be because zebrafish larvae retina contains few rod photoreceptors at this stage. Thus, if this cell type could be a mixed BC there would not be many in the zebrafish retina.

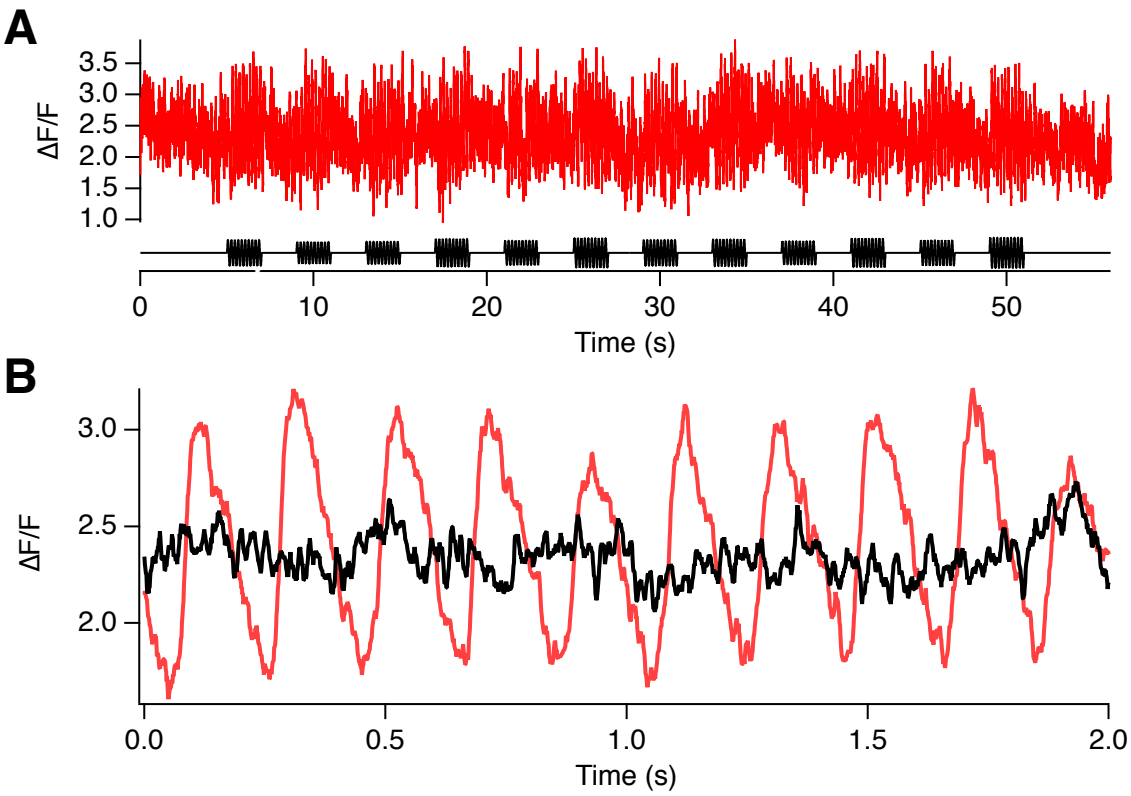

Figure 4.10. Some ON bipolar cells located at the layer s6 of the IPL are encoding temporal contrast in a linear fashion.

(A) Recording of a ON BC in response of different contrasts (black trace).

(B) Average of the baselines (12 baselines, extracted between each stimulus) between stimulus (black trace at the bottom of the panel) and the average response to the 12 stimuli (red trace) from all the stimulation periods shown in (A). Note that the average response to the stimuli seems to go up and down the baseline suggesting that this terminal releases constantly glutamate and is able to increase and decrease linearly the amount of glutamate released in response to contrast.

In a nutshell, BCs are able to use frequency coding and amplitude coding to encode temporal contrast. As a consequence, these two factors lead to an increase of the quanta released. However, other types of codes can be used by individual cells to encode information such as temporal precision. The timing of the response matters and contains information (Gollisch and Meister, 2008) and it has been shown that RGCs respond to visual stimuli with temporal precision of ms (Gollisch et al, 2008, Baden et al., 2011). It has been shown that BCs spike with a high temporal precision relative to visual stimulus (Baden et al., 2011) and are responsible of the RGC temporal precision as well.

4.3.4. MVR improves the temporal precision of signal transmission

I showed that BC terminals can distinguish different contrasts using the number of quanta per event as well as the number of events per cycle of stimulation.
However, while I compared the average number of quanta and events from repeated times of a stimulus to understand what is the neural coding, it doesn't require repeated stimuli for an animal to detect contrast intensity and the visual system must compute after one trial.
Moreover, the response time of visually driven behaviours suggests that the time integration of visual stimuli must be less than 1 s: for instance, a hunting behaviour, the fish larvae converges its eyes within 1 s after presented with a prey stimulus. The population activity in the optic tectum is correlated and active at 0.55 s before the start of the convergence eyes behaviour (Bianco and Engert, 2015). Thus, the brain ends up analysing neuronal responses in a short period of time. Hence the temporal summation and the timing of neuronal responses plays a crucial role in integrating visual information.
To encode information under these circumstances, neurons can use another way to encode information: the input onto the neuron can rely on temporal summation Several neurons fire practically simultaneously onto the same neuronal target. Thus, they increase the global depolarization of the dendritic tree and increase

the probability for the neuronal target to fire. Hence, having a high temporal precision is useful to encode information.

RGCs can elicit spikes with a very high temporal precision (about 3 ms) (Berry et al., 1997) and Baden et al showed that this temporal precision is already present in BCs (Baden et al., 2011). How does MVR relate to this temporal precision? I tackle this question in this chapter. The temporal jitter (the standard deviation of the response timing) was calculated at different contrasts for ON and OFF cells. Figure 4.10. summarizes the results.

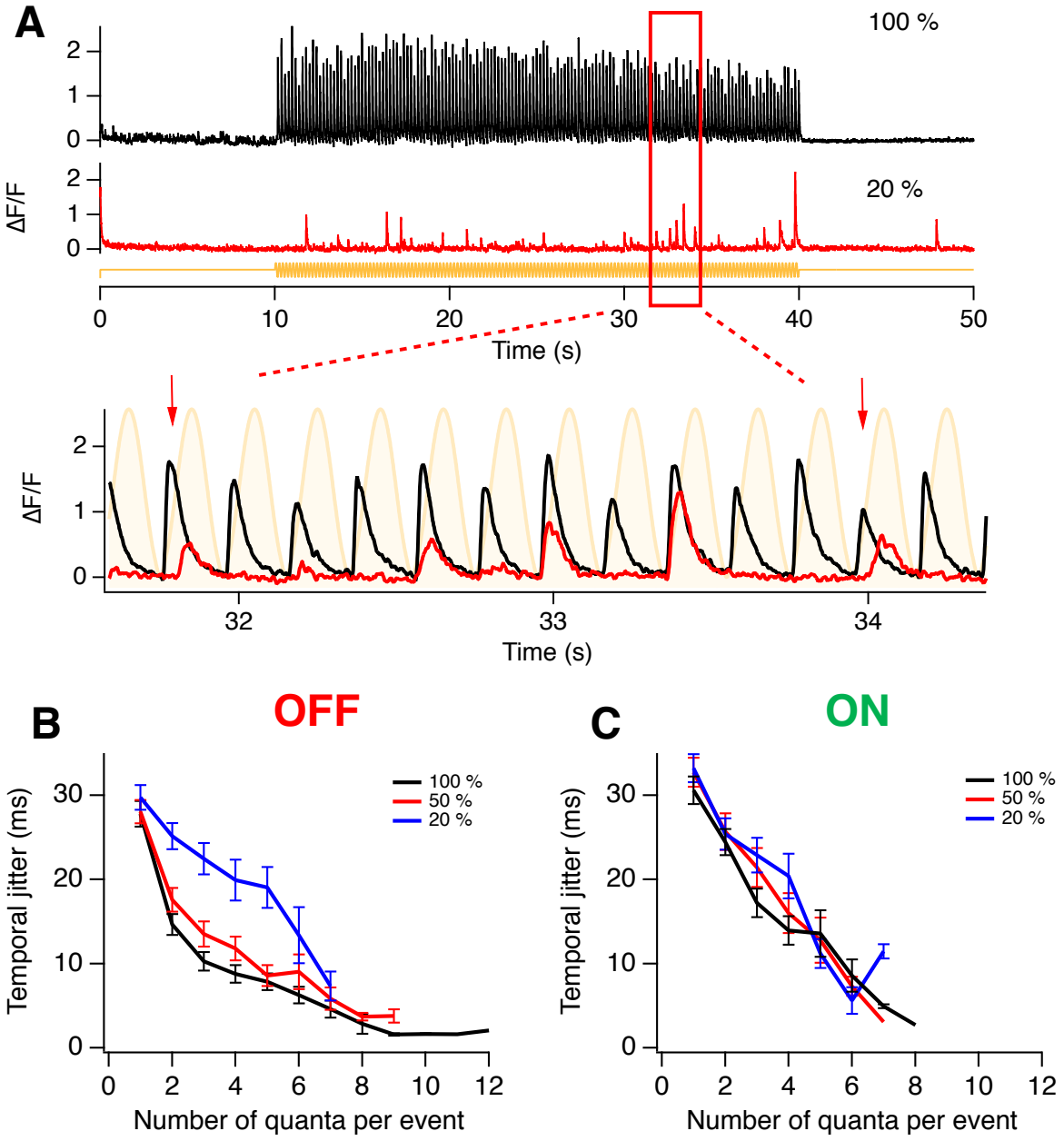

Figure 4.11. Multiquantal events encode contrast with higher temporal precision than uniquantal events.

(A) Period of activity at 20% and 100% contrast (red and black, respectively) is shown in relation to the sinusoidal stimulus (5 Hz). The timing of events at low contrast was more variable relative to the phase of the stimulus than events at high contrast.

(B) The standard deviation in the timing of events (temporal jitter) for OFF cells (n=33) plotted as a function of the number of quanta within the event. At all contrasts, events with larger numbers of quanta were more temporally precise. The largest events displayed a temporal jitter of ~2-3 ms, which is similar to the precision of spike times in post-synaptic RGCs.

(C) The results in B for ON cells (n=18). Note that there is not so many differences between 20% and 100%. At high contrast, ON cells have a lower temporal precision than OFF cells. The largest events were synchronized to a very high degree.

Figure 4.10.A. shows an example of a BC that respond to 20% and 100%. At 100% contrast, the responses have similar response timing whereas at 20% some of the responses are sometimes delayed. To measure these differences, the temporal jitter (Figure 4.10.B.) was calculated. At low contrast (20%), events with few quanta (from 2 to 4) were less phase locked (35 ms) than events with higher number of quanta (2-4 ms for OFF cells). Remarkably, uniquantal events have the lowest phase locking regardless of the intensity of contrasts (with a temporal jitter around 35 ms). Thus, MVR is linked to the high temporal precision of BCs. The more vesicles are released during one event, the higher the temporal precision of the events is. Moreover, the data suggest that ON cell are less temporally precise than OFF cells. This might be due by the fact that ON cells are using a metabotropic pathway (via the receptor mGluR6) (Nakajima et al. (1993), Nomura et al. (1994)) whereas OFF cells are using an ionotropic pathway (via Kainate and AMPA receptors) (DeVries et al. (1999), DeVries (2000)) which is faster and not based on a chain of molecular reactions. Most importantly, my results show that MVR contributes to temporal encoding with temporal jitter that are below 5 ms for higher number of quanta per events in OFFs cells. These results can be compared with the study carried out by Baden et al. (2011) where they measured the temporal jitter of goldfish BCs (spikes, not multivesicular events) *ex vivo* by electrophysiology (temporal jitter of 10 ms at 5 Hz).

4.4. Discussion

4.4.1. Increase of Calcium influx at the BCs synapse promotes MVR?

An interesting observation is that the number of vesicles per event increases when the contrast increases. What could explain this phenomenon? The increasing stimulation triggers an increase of membrane depolarization and calcium influx at the level of the active zone. One hypothesis could be that Ca^{2+} increases the number of vesicles in multivesicular events. As explained in Chapter 1, BCs can generate calcium spikes and sodium spikes in response to a

visual stimulus. The calcium spikes may be responsible for multivesicular events with a higher number of vesicles. This raises the question: what are the vesicle fusion mechanisms that underlie these observations? One of the hypothesis mentioned in the introduction (see Chapter 1) is that the fusion of the vesicles occurs through a compound fusion mechanism. Micrographs from electron microscopy (provided by Rachel Wong's laboratory to Nachiket Kashikar) reveals that compound fusion is happening in BCs terminal of zebrafish larvae (Figure 4.11.) This confirms the fusion coordination role for ribbons. By tethering the vesicles close to each other, they could facilitate the coordination of vesicles by enabling compound fusion. At the basis of the ribbon, a large vesicle seems to be the result of the fusion of two vesicles. This suggests that compound fusion takes place at the base of the ribbon, near calcium channels. Moreover, Figure 4.11.A. shows a large vesicle that does not fuse with the plasma membrane. This suggests that vesicles are able to fuse together before fusion with the plasma membrane. Compound fusion might then not be sequential but rather homotypic (see 1.2.2.). It has been shown in other systems that an increase of calcium concentration facilitates vesicle-vesicle fusion (Gratzl et al., 1977). The same phenomenon could happen at the level of BC terminals. Figure 4.12. summarizes the potential mechanisms behind vesicles fusion. At low contrast, only the vesicles docked at the plasma membrane are released (Figure 4.12., left). At higher contrast (Figure 4.12., right), the increase of calcium could trigger vesicle-vesicle fusion and the fusion of these larger vesicles. The docked vesicles could fuse first with the vesicles at the next row and then fuse with the membrane. Thus, at low contrast the number of vesicles that fuse with the plasma membrane could be lower because there is less compound fusion happening and that the calcium influx is too low to trigger the release of larger vesicles. It would be interesting to compute models to test these hypothesizes.

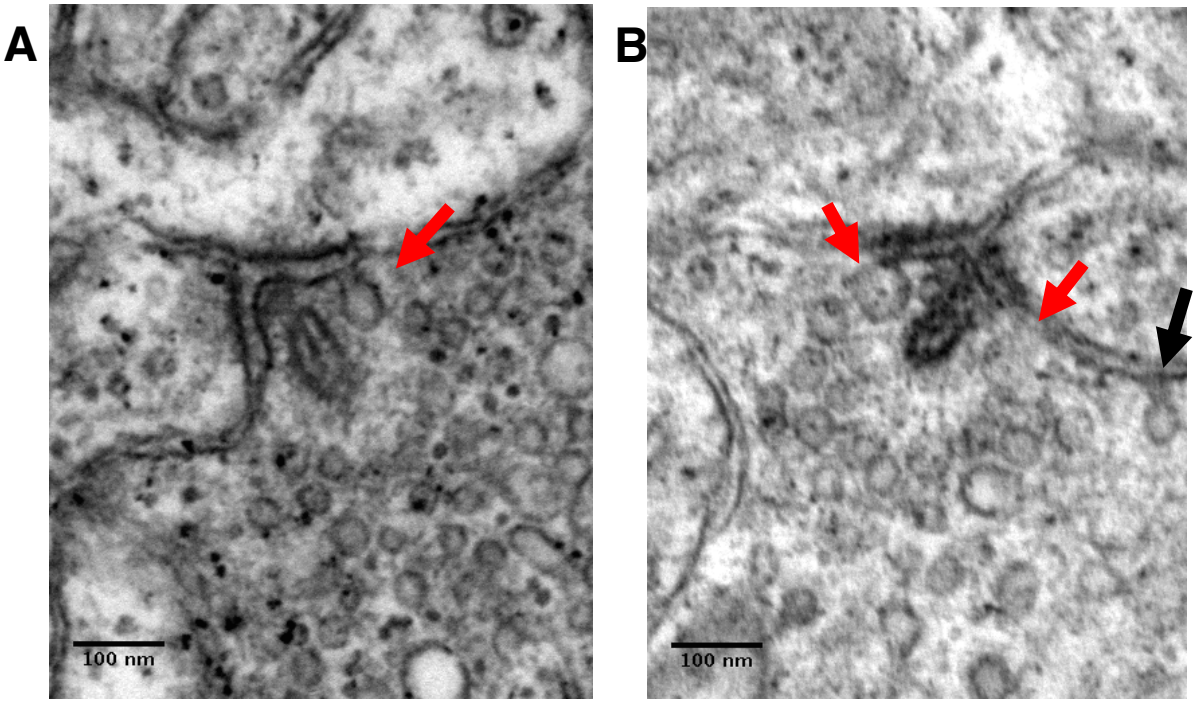

Figure 4.12. Electron microscopy micrograph suggesting the existence of compound fusion in zebrafish BCs. (provided by Rachel Wong's laboratory to Nachiket Kashikar).

(A) Ribbon synapse in 6 dpf zebrafish. The red arrow indicates a vesicle fusing with the membrane. The diameter of this vesicle is twice as large as the diameter of the other vesicles indicating that this vesicle could be the result of the fusion of two vesicles.

(B) Ribbon synapse in 7 dpf zebrafish. Red arrows show two vesicles at the base of the ribbon. The size of these vesicles is again twice than the diameter of the vesicles that are situated in the upper part of the ribbon. One of the vesicles (right) is fusing with the plasma membrane. The black arrow indicates a vesicle fusing outside the ribbon

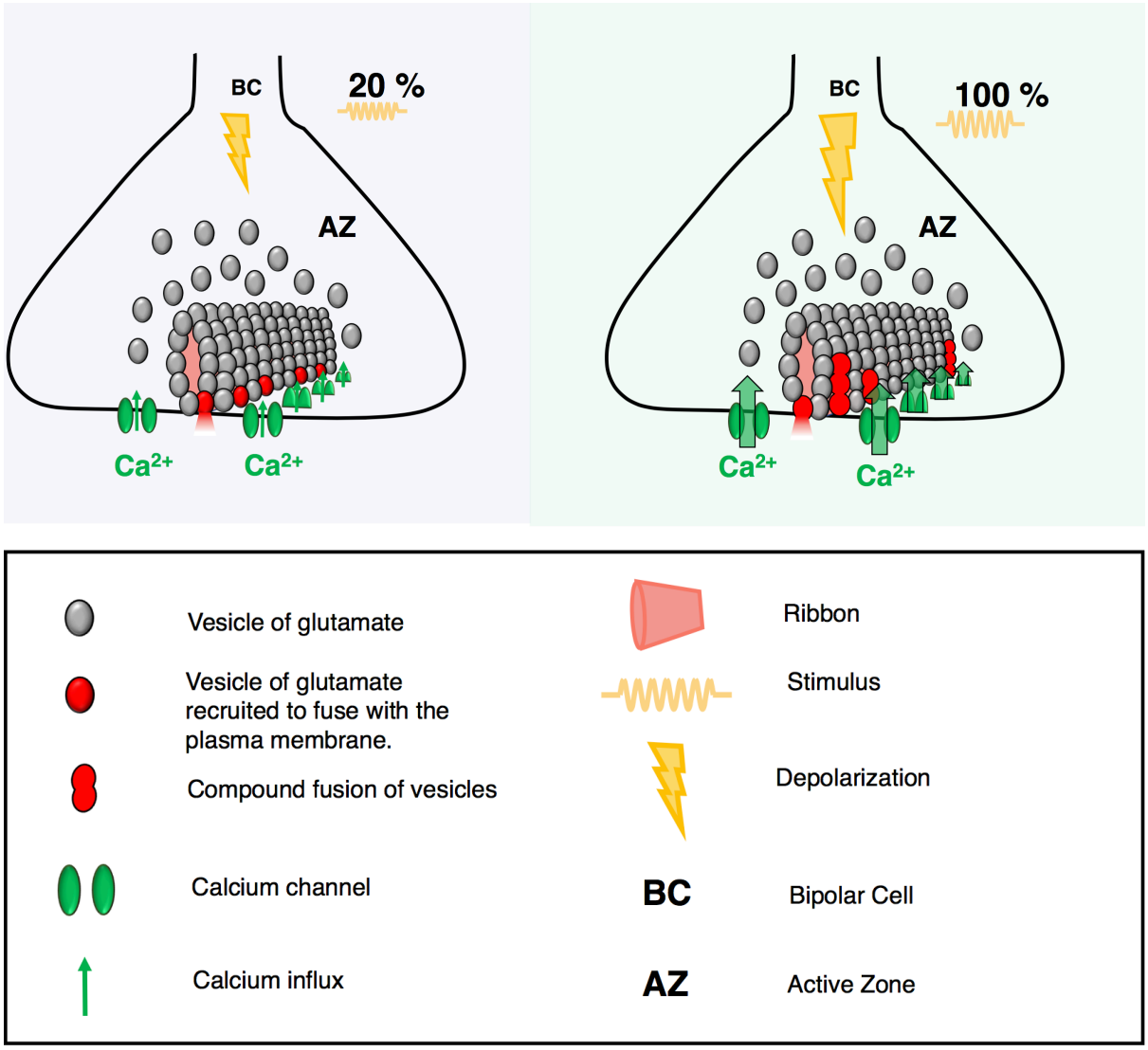

Figure 4.13. The increase of calcium influx into the BC terminal increases the number of vesicles per response during MVR.

The diagram shows a BC terminal containing two active zones. The terminal is responding at a low temporal contrast (20%) or high temporal contrast (100 %). The active zone contains one ribbon with vesicles tethered. The red vesicles represent the vesicles that fuse with the membrane in response to a visual stimulation.

Left: during a low temporal contrast stimulation (20 %), there is a calcium influx that promotes the release of the vesicles quasi-simultaneously during MVR.

Right: at higher temporal contrast (100 %), there is an increase of calcium influx. This increase of calcium influx promotes compound fusion, hence increasing the quantity of vesicles released during MVR.

4.4.2. There are different subtypes of ON and OFF cells that encode contrast differently

My data show that there is a diversity among OFF cells (some of them are able to release more vesicles than others) or ON cells (some of the cells are linear whereas the others rectify.). Where do these differences come from? Concerning ON BCs, the linear ones are located in the layer s6 of the IPL and could be rod BCs because, morphologically, these cells resemble mixed BCs in goldfish that are at the innermost location of the IPL and receive major inputs from rods.
The differences among OFF BCs might be due to different parameters such as the connection with the photoreceptors (Connaughton, 2011; Li et al., 2012), the type of the receptors at the level of dendrites (AMPA vs Kainate), the connections with ACs (Franke and Baden, 2017) or the types of the ribbon, the size of the active zones or the number of vesicles available at the level of the fusion site (LI et al., 2014). One way to identify them could be to look at the position of the terminal in the IPL and to see if there is any correlation with the activity of the cells. The OFF cells in the ON layer of the IPL could encode temporal contrast with MVR the same way as ON BCs because they could receive the same input from ACs or they may have developmental similarities.

4.4.3. Multiquantal events are more precisely phase locked than uniquantal events

For both ON cells and OFF cells, uniquantal events have a lower temporal precision compared to multiquantal events. These differences occurred at all contrast intensities examined (100%, 50% or 20%). One explanation is that uniquantal events include spontaneous noise which could enlighten why the temporal precision is lower for these events. However, for each contrast intensity studied, for ON and OFF cells, the temporal jitter of uniquantal events is the same. It is unlikely that spontaneous noise events could give rise to the same temporal jitter between ON and OFF, and the temporal jitter for uniquantal events is consistent among cells (standard error of the mean for the population data is

not bigger compared to the ones for multiquantal events). Thus, difference in temporal jitters may rather arise from a mechanism of multi- or uniquantal events.

These differences in temporal jitter were reported in other cell types that have ribbon synapses such as hair cells in the auditory system (Li et al, 2014). What are the mechanisms that could explain such a difference? Different hypothesis can be submitted. First, it could be that fewer vesicles are tethered at the level of the ribbon when uniquantal events occur. As it has been suggested before (Li et al., 2014), when a lot of vesicles are tethered to the ribbons, the effective calcium concentration increases faster and higher because the high number of vesicles near the calcium channels act as a diffusion barrier and allows the fusion to occur in a fast and accurate way. However, when few vesicles are tethered to the ribbon, the calcium diffuses more and then the fusion occurrs in a less precise fashion. Thus, the timing of vesicle release may be more arbitrary than for vesicles tethered at the ribbon and closer to the calcium channels.

A second hypothesis is that the fusion mechanisms could happen at the ribbon synapse for mutivesicular release before fused to cell membrane but not for uniquantal release. Such compound fusion (Figure 4.11.) may involve a different mechanism than uniquantal fusion, and thus create differences in temporal jitter.

Since all the BCs examined in this study use MVR, one question that arises is what is the role of uniquantal events? Do they transmit specific types of information? Are they useful to encode a specific type of information? One simple explanation could be that uniquantal events could play a more important role in temporal summation (when a neuron spikes several times to encode information) rather than spatial summation. Therefore, they could give more information about the duration of the stimulus rather than the type of stimulus or its intensity.

Chapter 5

Circuit mechanisms of dynamic predictive coding in retinal ganglion cells

5.1. Introduction

In chapter 4, I showed that individual BCs use both event rate and amplitude to encode temporal contrast. Other behaviours of these cells were also observed, including adaptation, a phenomenon that involves the modulation of the retina's sensitivity in response to the recent history of the stimulus. Adaptation is a widespread phenomenon across sensory systems (Pérez-González and Malmierca, 2014 ; Lampl and Katz, 2017; Webster, 2012) that has been thoroughly studied in the retina (Nikolaev et al., 2013; Demb, 2008; Gollisch and Meister, 2010). Adaptation can be added to the list of various computations that are already occurring, such as motion anticipation or direction selectivity (see 1.1.2.). Contrast adaptation in the retina avoids saturation of neuronal responses and, thus, the retina can use its dynamic range more efficiently.
In the previous chapter, I observed that BC terminals adapt to repeated presentations of stimuli with the same temporal contrast (Figure 4.2.). Adaptation in BCs was already described in several studies (Nikolaev et al., (2013); Manookin and Demb, 2006; Kim et al., 2001). Temporal contrast adaptation was also described in RGCs (Shapley, 1997; Shapley and Enroth-Cugell, 1984).

A different type of adaptation has been described by Hosoya et al. (2005). They showed that RGCs could perform a new type of adaptation for spatial correlation within the visual stimuli. This phenomenon was named pattern adaptation. The retina can adapt to the spatial correlations presented in its recent history in a dynamic manner. In their experiment, Hosoya et al. (2005) used isolated retinas of salamanders and rabbits to record electrical signals with electrophysiology. They presented several sequences of images with spatial correlations that were differing only by the orientation (horizontal or vertical flickering light and dark grating) and studied the different adjustments of neuronal sensitivity to these different orientations After one of the gratings was presented, the following stimulus was either the same grating or a grating with the opposite orientation. The results of this experiment showed that the RGCs were adapting specifically to the first orientation presented. Moreover, they increased their sensitivity to the

opposite grating. This type of complex adaptation is known to occur in the human visual system at the level of higher visual areas such as the visual cortex named “dynamic predictive coding” (DPC) (Müller et al., 1999). The term “predictive coding” was already used to describe the idea that sensory systems are coding preferably non-redundant information and that they use different mechanisms (such as contrast adaptation) to discard redundant information (Srinivasan et al., 1982). For instance, if a natural scene contains many horizontal objects, visual information should mainly include edges of horizontal objects and not the contents of the object itself since it is likely that neighbouring pixels at the centre of an object contain the same - and thus redundant - information whereas at the border, there is a discontinuity. According to predictive coding, the redundant component of the environment is simply predicted not to change, with the retina sending information only when the prediction is not met (Masland, 2005).

The mechanisms underlying DPC in RGCs remain poorly understood. Different suggestions have been made by Hosoya et al., (2005) to understand this phenomenon. They postulated a pattern detector hypothesis: DPC would occur at the level of the RGC inputs. A combination of several pathways within the RGC circuitry would enable to generate DPC signals in RGCs. The neurons implicated in this mechanism would be selective for one orientation. When this orientation is strongly present or for a prolonged period of time, the neurons would be driven intensively, eliciting a fatigue. This would decrease its contribution to the RGC inputs and thus increase the sensitivity of the RGCs to the opposite orientation. This raises the question: what are the potential actors that could act as pattern detectors? There are two main candidates: the BCs and the ACs. Concerning the BCs, the authors point out that the receptive fields of BCs are round or slightly elongated, the latter may be an indication for their weak orientation selectivity. Moreover, based on several studies about adaptation in BCs (Baccus and Meister, 2002, Rieke, 2001), they concluded that BCs adaptation would contribute to less than 1% of the orientation selectivity of RGCs. However, all the studies were based on electrophysiology experiments that measured signals

from the soma of BCs. As mentioned before in chapter 1 (1.1.2.), various studies showed that BC synapses performed various computations. Furthermore, data from Lagnado's laboratory (Johnston et al., (2018) and from Antunicci et al. (2016) show that BCs can be orientation selective and have an elliptic receptive field. Hence BCs could still be a candidate to explain the DPC responses in RGCs of zebrafish.

Concerning ACs, some of them have been shown to be orientation selective (Bloomfield, 1994; Antunicci , 2016; Johnston et al., 2018). Amacrine cells are excited by BCs and have been shown to connect via feedforward inhibition onto RGCs (Werblin, 1970; Werblin and Copenhagen, 1974), feedback inhibition onto BCs (Flores-Herr et al., 2001, de Vries et al., 2011) or lateral inhibition (Roska et al., 1998; Eggers and Lukasiewicz, 2006; Zhang et al., 1997, Ding et al., 2016; Lee and Zhou, 2006). In case of feedforward inhibition and feedback inhibition, a fatigue from ACs would decrease the inhibition of RGCs or increase the excitation from BCs respectively. In the presence of the orientation stimulus, this fatigue would generate an effect opposite to what Hosoya et al. (2005) observed (sensitization of RGCs to the pattern instead of adaptation). Lateral inhibition seems to moderate the weight of feedback inhibition and feedforward inhibition. Hence, removing this lateral inhibition leads to an increase of this adapting-induced phenomenon. Therefore, a fatigue from these cells would explain the adaptation effect observed in Hosoya et al., 2005. Another hypothesis Hosoya et al. (2005) suggested is based on the plasticity of the synapses (Figure 5.1.). In this model, whens the signal from ACs and RGCs are correlated, the synapses become stronger but when the signal is anticorrelated, the synapses become weaker. Therefore, if a ganglion cell has a center-surround receptive field, the surround is modulated by amacrine cells. In the presence of a horizontal grating (Figure 5.1.A.), the RGC is strongly correlated with the ACs on both sides, but anticorrelated with the ACs below and above its center. The receptive field of the RGC becomes elongated in the vertical .

direction (Figure 5.1.B.): it is less sensitive to horizontal grating but more sensitive to the vertical grating.

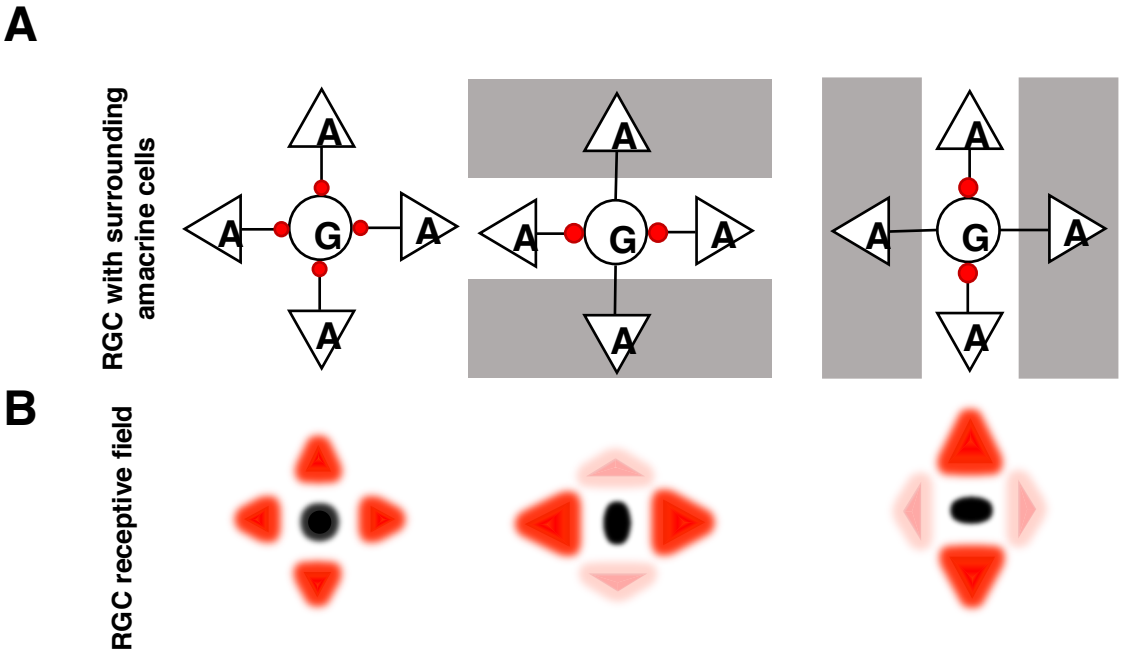

Figure 5.1. Model for DPC based on a synaptic plastic network (Adapted from Hosoya et al, 2005).

(A) Schema representing a RGC (G) connected to 4 amacrine cells (A) through plastic synapses (red dots). Depending on the grating orientation, the synapses that are correlated will become stronger and the synapses that are anticorrelated become weaker.

(B) The red triangles represent the receptive field of ACs that connect to the same RGC as presented in (A). The size and the color indicates the strength of the receptive fields. The black square represents the receptive field of the RGC. During a presentation of a grating, the receptive field of ACs that are correlated with the stimulus becomes stronger whereas the receptive field of the ones that are responsive to the opposite orientation becomes weaker. The shape of the receptive field changes over time as a consequence of the synaptic plasticity. This reduces the RGC sensitivity to the prevalent stimulus.

iGluSnFR is a powerful tool to study the mechanisms of DPC in RGCs. iGluSnFR can be expressed at the level of individual RGCs. It is therefore possible to directly observe the inputs of BCs onto RGCs. Moreover, it is also possible to record the outputs of the same RGCs in the optic tectum of zebrafish. DPC of orientation (concerning spatial patterns) is present in rabbits and salamanders. In this chapter, I showed that DPC exists in zebrafish RGCs as well. To investigate how RGCs were encoding DPC, the following stimulus was designed: 2 gratings, vertical and horizontal, were alternatively presented twice to the fish for 10 s each (Figure 5.2.). DPC was evaluated by observing whether the response to the new grating was larger than the response to the former (adapted) grating. Responses were recorded at the level of the retina to understand what could be the role of excitatory inputs of BCs in DPC. Responses at the level of the optic tectum (where the outputs of RGCs are located) were monitored as well to compare DPC between inputs and outputs. Moreover, I tested whether disrupting inhibition in the IPL by injecting GABA and Glycine antagonists affected DPC in RGCs.

5.2. Methods

The ROI were extracted as explained in 2.3.3. To express iGluSnFR in RGCs, I generated elavl3:HucKalTA4 plasmid. This plasmid was injected in the transgenic line *Tg(UAS:iGluSnFR)*. Only fish with no labelled tectal cells were recorded and analysed.

To study DPC, I recorded the inputs and outputs while presenting a static grating that continuously reversed contrast at 5 Hz. Horizontal and vertical orientations of the grating were presented each for 10 s and were alternately presented during the entire stimulation of 40 s (Figure 5.2.).

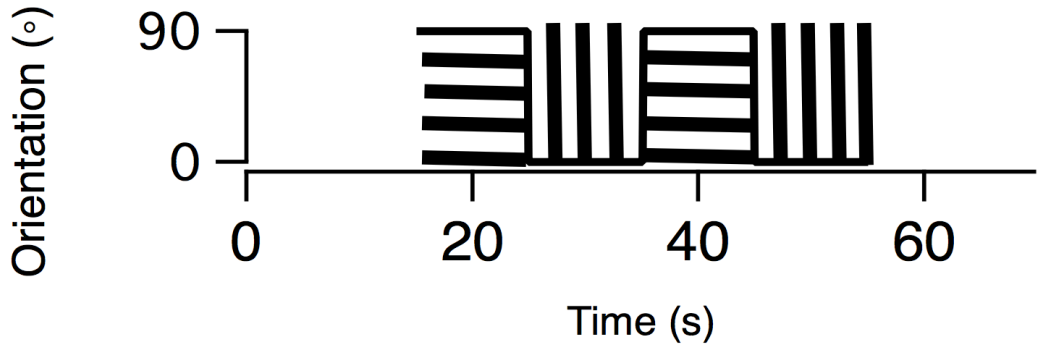

Figure 5.2. Probing DPC in zebrafish RGCs.

The protocol used in the following experiments is 15 s of constant light, followed by 40 s of grating and then 15 s of constant light. The constant light had the same average illuminance than the grated stimulus.

The grating part of the stimulus consisted of 10 s of a horizontal grating (90 degrees), followed by 10 s of a vertical grating (0 degrees), 10 s of the horizontal grating and finally 10 s of the vertical grating.

Glutamatergic inputs onto RGC dendrites were obtained by recording individual RGCs at different planes of depth.

As described in Chapter 2 (see 2.3.3.), ROIs were extracted using Igor scripts written by members of Lagnado's laboratory (Johnston et al., 2018).

One manner to quantify the orientation selectivity of a cell is to calculate the orientation selectivity index (OSI). The OSI for each cell was determined using the formula:

$$OSI = \frac{|a - b|}{|a| + |b|} \qquad (15)$$

Where **a** and **b** are the responses to orthogonal angles. **a** and **b** were the maximum amplitudes measured during the first 0.5 s after the start of each grating. An OSI was only calculated if the difference in a and b was at least four times the standard deviation of the baseline.

DPC cells were identified as follows:
To quantify the response of a new orientation after adaptation from the precedent stimulus, the maximum response during the first 5 seconds after the start of each grating was calculated. This maximum was compared with the average response amplitudes during the preceding stimulation (15 s). If the maximum amplitude was more than four times the average response, It means that the response to the non-adaptive stimulus was larger than the adaptive stimulus. Then the cell was classified as performing DPC.

Contrast cells were identified as follows:
The maximum amplitude of responses during the first 5 seconds after the start of each grating was calculated. If only the first response was four times higher than the baseline (amplitudes during no grating stimulus), then the cell was classified as responding to contrast.

The statistics were performed using the Fisher exact test with the software Igor 7.

5.3. Results

I generated a elavl3: HucKalTA4 plasmid. We injected the plasmid into one-cell stage embryos and we recorded the RGCs for the control experiments together (the data with no drug injection). Dr. Jamie Johnston performed the analysis presented in Figure 5.3 and the analysis for control experiments. I carried out the inhibition experiments and performed the analysis.

5.3.1. iGluSnFR in the optic tectum does not detect spillover from neighbouring RGCs

As I explained in 4.3.1. iGluSnFR does not detect spillover from neighboring terminals in BCs. However, it is necessary to demonstrate it as well in the optic tectum since it is a different area (Figure 5.3.). The principle of the experiment is similar to the one in chapter 3. I recorded a RGC (Figure 5.3.A.) (the retina had only one RGC labelled in this example). I found the output of this cell in the tectum (Figure 5.3.B.) and I recorded responses from its terminals (Figure 5.3.C.).
I then performed a laser ablation of this cell (Figure 5.3.D). Here again, I observed that all the signals from this cell were abolished. Since I did the laser ablation in the retina, my ablation did not affect the environment of the terminal (in the optic tectum). Therefore, I did not need to record neighbouring cells to show that the environment of the terminal was not affected by the laser ablation. The output signals from RGCs were abolished when the cell body was ablated using the InfraRed laser, demonstrating that they reflected the output of the imaged neuron rather than glutamate release from neighbouring cells.

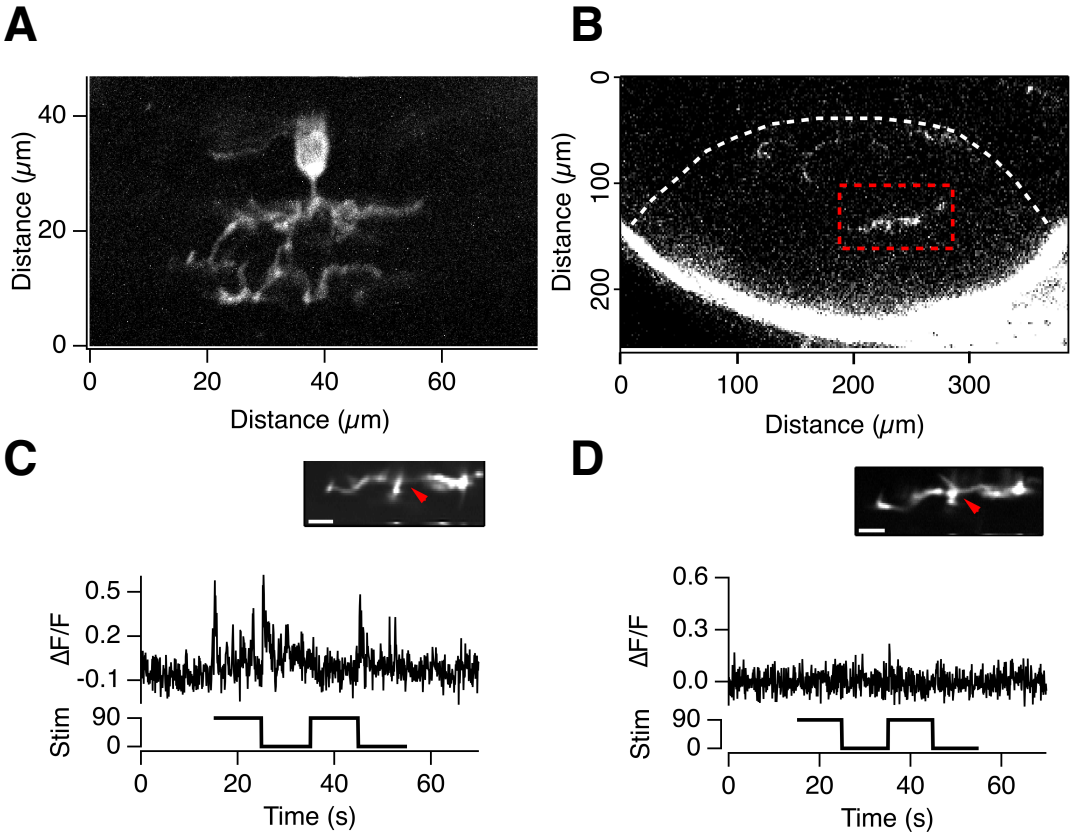

Figure 5.3. Ablation of RGCs completely silenced iGluSnFR signals in the optic tectum.

(A) Maximum intensity of a RGC imaged *in vivo.*

(B) Single plane through the optic tectum showing iGluSnFR expression in the terminal of the RGC shown in (A).

(C)Top: zoom in on the RGC terminal presented in (B). The red arrows indicates the area recorded. Bottom: Response from the axon terminal shown in (B) before laser ablation.

(D) Top: terminal (presented in (B)) after laser ablation of the cell body. The red arrow indicates the area recorded.

Bottom: After laser ablation, the signals presented in (C) were completely abolished.

The stimulus presented in (C) and (D) is the one from Figure 5.2.

Scale bar: 5 μm.

5.3.2. A new optical approach to study glutamate neurotransmission at the level of retinal ganglion cells

Although it has been long known that some RGCs are orientation selective, the underlying circuit mechanisms are much less known (Antinucci et al., 2016). In the study by Antinucci et al. (2016), they expressed SyGCaMP3.5 in RGC to record responses at the RGC axon terminals during the stimulus of drifting bars with various orientations in zebrafish larvae. By genetically ablating a subset of ACs, they found that teneurin3 positive ACs are necessary for generating the orientation selective responses in RGC axon terminals in the tectum. One of the drawbacks of this study is, however, that they analysed the number of voxels with orientation selective responses and this does not provide insights into the number of orientation selective RGCs because RGC axon terminals often span across many voxels. Moreover, because they ablated teneurin3 ACs during development, they could not exclude the possibility that the decrease of orientation selectivity could be explained by developmental issues caused by the absence of this population.

One of the aims of my project was to develop another optical approach to understand how orientation selectivity arises in RGCs and how DPC is affected by inhibition in the IPL. I expressed iGluSnFR in isolated RGCs and observed the BCs glutamatergic inputs onto RGCs and the RGC output signals.

Figure 5.4.A. shows an example of a RGC and its dendrites in the retina. The ROIs are represented by coloured circles and are indicating “hotspots” of approximately 1 μm of diameter: the dendritic areas onto which BCs are releasing glutamate. For each cell, different BC inputs at different planes were extracted (see 2.3.3.) and it was possible to visualize what their glutamatergic inputs onto RGCs were. Figure 5.4.B. shows traces extracted from the ROIs indicated in Figure 5.4.A. The inputs of this cell are responding to contrast but are not orientation selective and are very similar to each other.

We then recorded the outputs of these cells in the optic tectum. A study by Robles et al. (2014) relating the location of RGCs in the retina to the location of their projection sites in the tectum was used to localise the outputs of RGCs and compare them to the inputs of RGCs. Hotspots of fluorescence were also observed on RGC axons projecting into the tectum. An example is shown in Figure 5.4.C-D. Figure 5.4.E. shows different input-types that the cell shown in Figure 5.4.C. received from BCs. In total, this cell received 23 inputs from BCs showing different features. Some inputs were orientation selective (2 from the bottom), whereas some of them were not, but were responding strongly to the start of the grating (three first traces from Figure 5.4.E.). The average of all inputs (Figure 5.4.F., bottom trace) was compared to the cell's output in the tectum (Figure 5.4.F., top trace). The output of the cell had a more transient response at the start of the grating and presented a higher OSI (OSI=0.60 for the output compared to 0.4 for the sum of the inputs) (similar to the orientation selectivity of the inputs the RGC received). One interpretation could be that the inputs received by RGCs have different weights depending on the length of the dendrites or the receptors present on the dendrites. It could be that the inputs that are orientation selective are closer to the soma. Moreover, I observed DPC in RGCs outputs (Figure 5.5.A., bottom trace). When the orientation of the grating changed, the response of the cell increased. Hence, DPC seems to be a mechanism conserved between vertebrates (since it has been shown in salamander and rabbit). zebrafish is a good model to study DPC in RGCs.

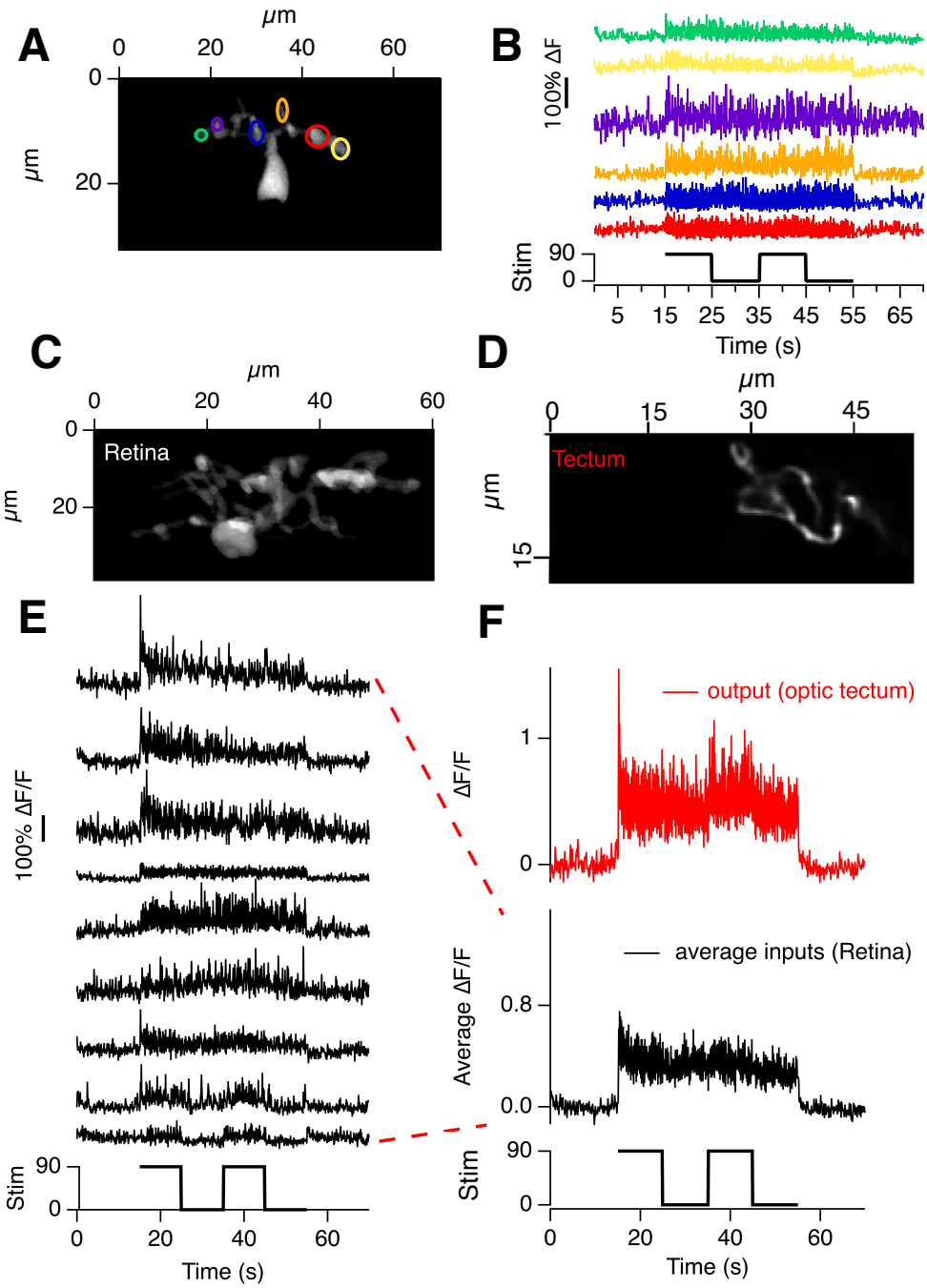
A
μm
0
20
40
60
μm
B
100% ΔF
Stim
90
0
5
15
25
35
45
55
65
Time (s)
C
μm
Retina
D
μm
Tectum
E
100% ΔF/F
Stim
Time (s)
F
output (optic tectum)
ΔF/F
average inputs (Retina)
Average ΔF/F
Time (s)

Figure 5.4. Optical method with iGluSnFR to record excitatory inputs and outputs of RGCs.
(A) Overview of a RGC in the retina. The circles represent the ROIs. The ROIs represent the "hotspots"I observed during my experiments.
(B) Traces extracted from the ROIs presented in B. Note that none of the ROIs presents orientation selectivity.
(C) Overview of another RGC in the retina.
(D) Overview of the output of the same RGC in the tectum.
(E) Example traces of input signals that the RGC presented in C. received. Note that some inputs are orientation selective whereas other are just responding to contrast.
(F) Comparison between the excitatory inputs (black trace) and the output (red trace) of the RGC presented in (C). Note that the OSI of the output has a higher OSI (0.60 for the output against 0.45 for the inputs) and a higher amplitude than the average of the inputs. The output was orientation selective (OSI > 0.5).
The stimulus presented is the one from Figure 5.2.

5.3.3. Testing the role of inhibition in DPC

In these experiments, we did not observe DPC at the level of BCs inputs onto RGCs (606) (Johnston et al., 2018). We did observe strong orientation selectivity inputs onto RGCs (48% of inputs observed on 27 RGCs were orientation selective (analysis from Jamie Johnston)), hence, they play a role in DPC. This also suggests that ACs are involved in computing DPC.

My next aim was to understand how inhibition from ACs affects DPC of RGCs. To do so, I recorded the outputs of RGCs in the tectum (89 cells) and I disrupted inhibition (72 cells). It has been shown that local interactions between the BCs synapse and inhibitory AC dendrites can modify the signal that BCs transmit (Asari and Meister, 2012). Moreover, in Johnston et al. (2018), it has been shown that disrupting inhibition from ACs decreases the number of orientation selective BCs. Similarly, Antinucci et al. (2016) found a class of ACs implicated in generating orientation selectivity. I did not observe predictive coding from glutamatergic inputs onto RGC dendrites, suggesting that DPC was shaped by inhibition inputs or was generated at the level of RGCs. To test this hypothesis, I disrupted inhibition in the IPL by injecting GABA and Glycine antagonists in the vitreous chamber. The results are shown below:

The quantities presented in Figure 5.5. were calculated from 5 fish after disrupting inhibition. There was not a significant decrease of contrast responsive cells (32% (24/89) against 27% (23/72)) ($p=0.49$). The number of DPC cells were not affected (22% (20/72) against 28% (23/89) for the control) ($p=0.20$). The number of orientation selective cells decreases by 10% but it was not significant ($p=0.33$). Cells with a preferred orientation of 0 degrees decreased strongly ((18.7% (16/72) against 50% (45/89)) ($p<0.01$), whereas I observed an increase of the number of cells presenting an orientation selectivity for 90 degrees (23/72 against 10/89) ($p<0.01$). This result seemed surprising, because data from the Lagnado laboratory show that blocking inhibition suppresses orientation selectivity in BCs, the excitatory inputs of RGCs (Johnston et al., 2018). Hence,

when I block the orientation selective input of RGCs I would expect a global decrease in RGCs with a preferred orientation of 90 degrees. This brought me to further analyse my results by looking at the data for each fish separately.

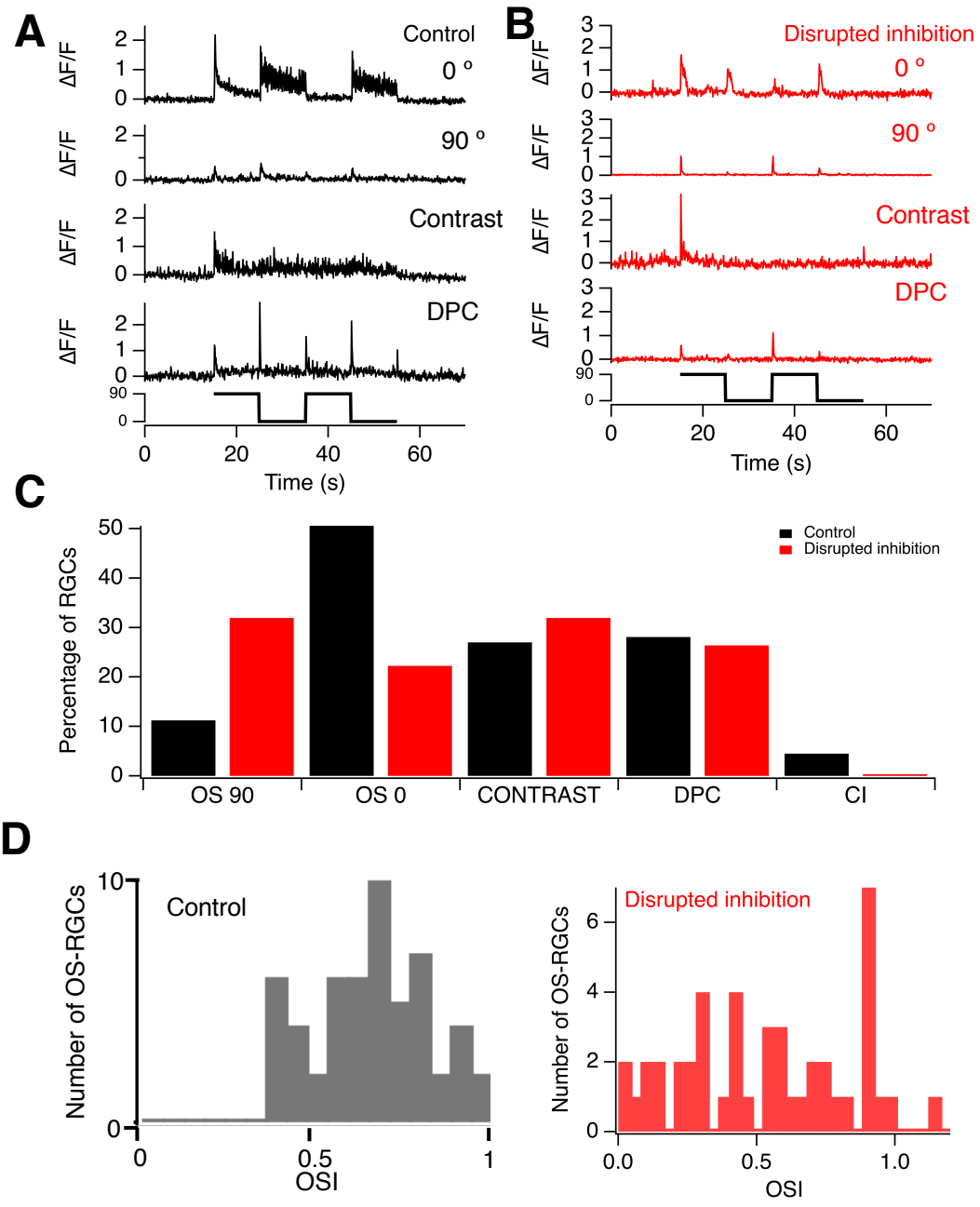
A
Control
0 °
90 °
Contrast
DPC
ΔF/F
Time (s)
B
Disrupted inhibition
0 °
90 °
Contrast
DPC
ΔF/F
Time (s)
C
Control
Disrupted inhibition
Percentage of RGCs
OS 90
OS 0
CONTRAST
DPC
CI
D
Control
Number of OS-RGCs
OSI
Disrupted inhibition
Number of OS-RGCs
OSI

Figure 5.5. Disruption of inhibition decreases the proportion of orientation selective RGCs

(A) Examples of responses from RGCs. Dynamic predictive coding (DPC) cells respond with transient increases in glutamate when the orientation of the stimulus changed. Orientation selective (OS) show larger responses for one orientation. Some cells only responded to the contrast with either and increase or decrease in glutamate.

(B) Example of RGC responses after disrupting inhibition. Note that the responses are more transient.

(C) Comparison of RGCs under control conditions or after injecting gabazine and strychnine. The contrast responsive cells and the cells exhibiting DPC proportions remain the same whereas there is a decrease of 0-OS RGCs and an increase of 90-OS RGCs.

(D) OSI for the OS RGCs under control conditions.

(E) OSI for RGCs after disrupting inhibition. Note that there is a population of cells with an OSI < 0.4.

Stim=stimulus (orientation of the grating).

0 º=Orientation selectivity for 0 º.

90 º=Orientation selectivity for 90 º.

5.3.4. Disrupting inhibition does not change the proportion of DPC RGCs

As mentioned before, the number of DPC cells does not change after disrupting inhibition (23/89 for control against 20/72 after inhibition disruption) (p=0.20). To investigate this observation further, I examined the different DPC responses of RGCs for the controls and the RGCs in the presence of strychnine and gabazine (which disrupts the inhibition in the IPL). The results are presented in Figure 5.6. Figure 5.6.A. and Figure 5.6.B. show raster plots of cells presenting DPC in absence or in presence of strychnine and gabazine respectively. The responses seem more transient after disrupting the inhibition. Two examples are presented in Figure 5.6.C. and Figure 5.6.D. to illustrate the types of responses observed. I did not observe any sustained response after injecting these drugs. The average response of all the cells confirmed this observation (Figure 5.6.E.): the responses of the control remain sustained compared to when inhibition is disrupted. Besides, data from the Lagnado's laboratory indicate that when inhibition from ACs is perturbed, the maximum amplitude response of BCs increase (experiment performed with calcium indicator). This is what I observed as well during my experiments (with iGluSnFR) (Figure 5.6.E.). This could explain why I observed more transient responses: in absence of inhibition, the pool of vesicles in the BCs active zone becomes empty much faster and thus there are not enough vesicles available to obtain a sustained response. Since I observed some changes in the responses of RGCs but no changes concerning the number of DPC RGCs, it is possible that the concentration of the drugs I injected was not high enough to observe an effect of disrupting inhibition on DPC. Therefore, it would be interesting to repeat this experiment using increased concentrations of gabazine and strychnine injected.

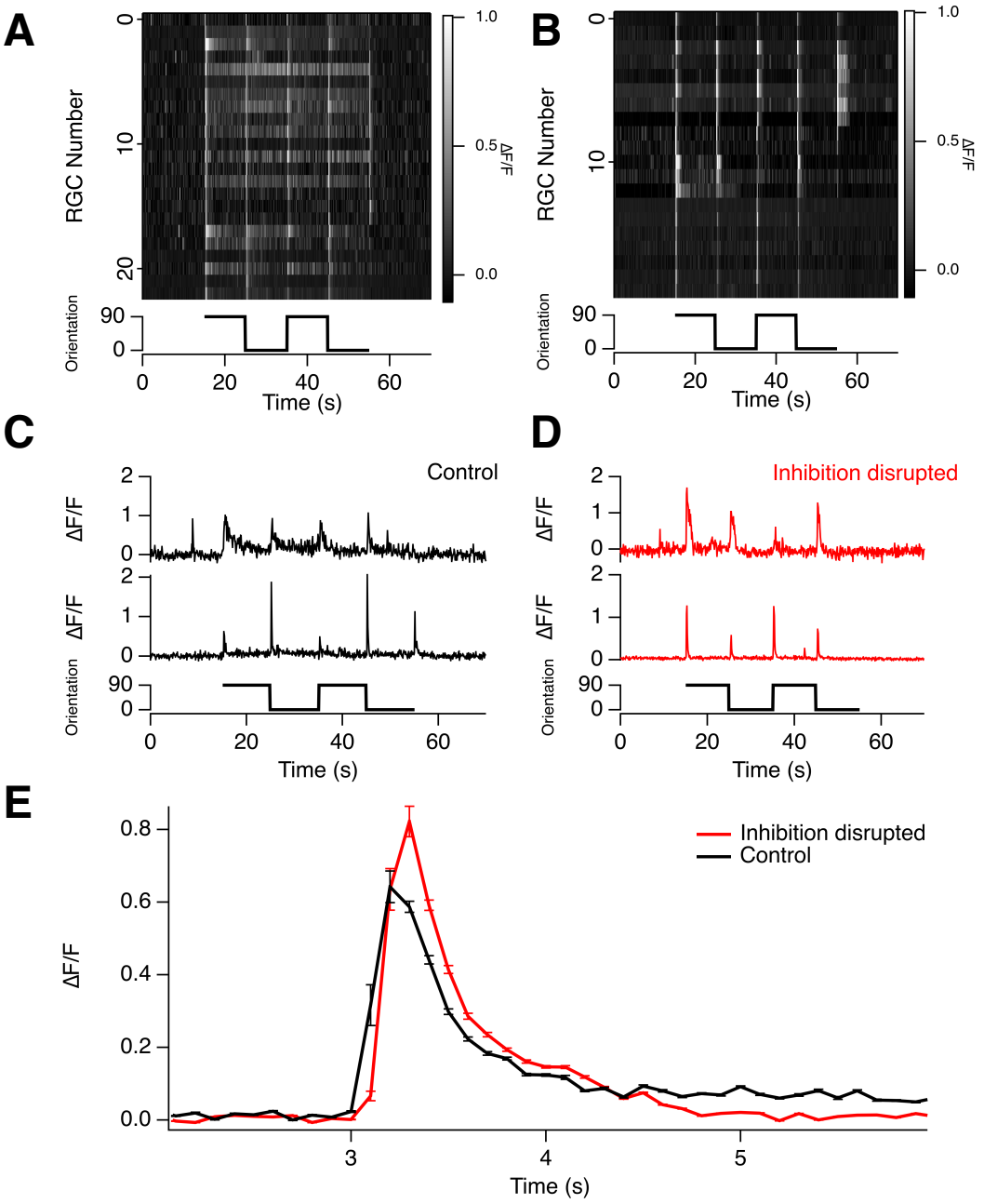

Figure 5.6. Disruption of inhibition does not affect DPC RGCs.

(A) RGCs in the control condition that perform DPC.

(B) DPC RGCs after inhibition disruption.

(C) Two examples of RGCs in control. Top: example where a response is slow. Bottom: example of transient responses.

(D) Two examples of DPC RGCs after inhibition disruption. Note that the responses are more transient than in the control (B). Top: example where a response is slow. Bottom: example of transient responses. Note that a slow response (top row) will still be slower than a fast response The panels (C) and (D) show data from different fish.

(E) Average traces for all the trials concerning the control cells (n=23) (black trace) and the cells after inhibition disrupted (n=20) (red trace). The error bars represent the standard errors.

5.3.5. Disturbing lateral inhibition has variable effects depending on the samples

Because I observed an increase in cells with a preferred orientation of 90 degrees (5.3.4.) (10/89 for the control against 23/72 when inhibition was disrupted, $p<0.01$), I wanted to know whether these results could be explained by heterogeneous effects of disrupting inhibition and I wanted to understand whether the results I obtained were consistent for each fish. I decided to plot the results for each fish separately. The results are presented in Figure 5.7. The results are heterogeneous except for DPC cells. Some fish have few 90-OS cells after drug application (Figure 5.7.C.) (10/89 for the control against 1/17 for Fish 2, $p=0.51$) while for others it is the opposite (Figure 5.7.D.) (10/ 89 for the control against 15/ 28 for Fish 3, $p<0.01$).

For each fish, the sparse labelling of RGCs is random and not targeted at specific RGC subtypes, the effects of the drug may therefore vary. Moreover, the results indicate that the increased number of 90-OS cells is driven by two fish. Since the effects are so heterogeneous for orientation selectivity, it would be necessary to record more samples to draw a general conclusion from this experiment concerning the impact of ACs onto orientation selectivity in RGCs.

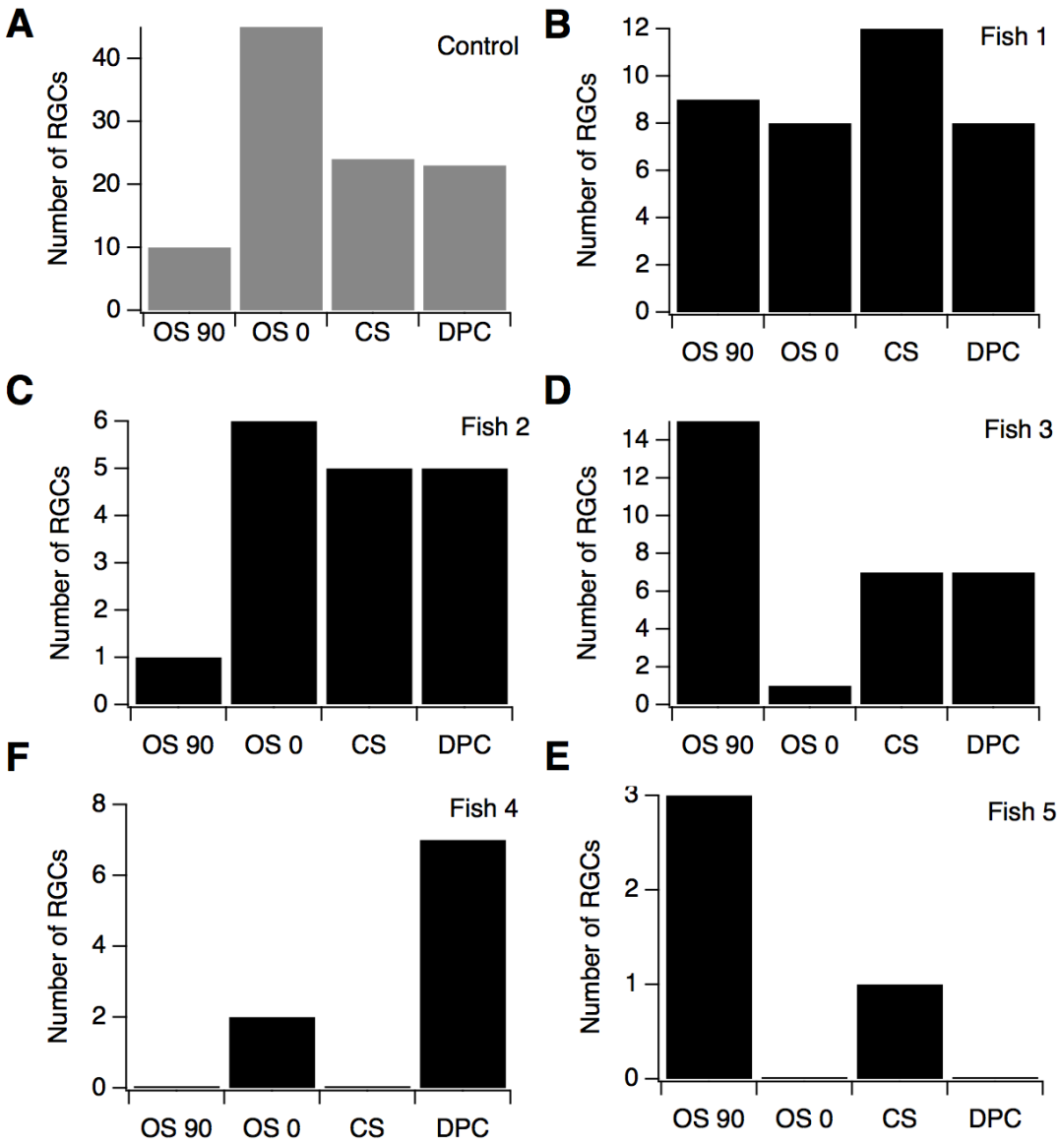

Figure 5.7. Disruption of inhibition has heterogeneous effects on RGCs.

Number of orientation selective RGCs for vertical (OS 0) or horizontal (OS 90) gratings, contrast responsive RGCs (CS) or DPC RGCs (DPC) in control conditions (A) and after disrupting inhibition (B-E; all the fish are included).

5.3.6. Disturbing inhibition decrease the orientation selectivity index for most of the fish analysed

I observed mixed effects of removing inhibition depending on the fish. To understand whether the orientation selectivity index (OSI) was affected, I calculated the OSI for every fish analysed for this experiment. Figure 5.8. indicates that for four out of five fish there is a decrease in the OSI compared to the control (Figure 5.8.A.). The proportion of cells with an OSI inferior to 0.5 increased (10/55 for the control, Figure 5.8.A. against 19/39 when inhibition was disrupted, $p<0.01$). 4/5 fish indicated the same results (Figure 5.8.B-F., $p<0.01$).The only fish that does not show this decrease has only three cells that were responding to the stimulus. The average OSI reflected the individual results (Figure 5.5.D.) (average of OSI of 0.68 for the control experiments against 0.53 after inhibition disruption). Therefore, it appears that removal of inhibition affects the strength of the OSI and this is a general effect. Inhibition would affect mostly the OSI of orientation selective cells.

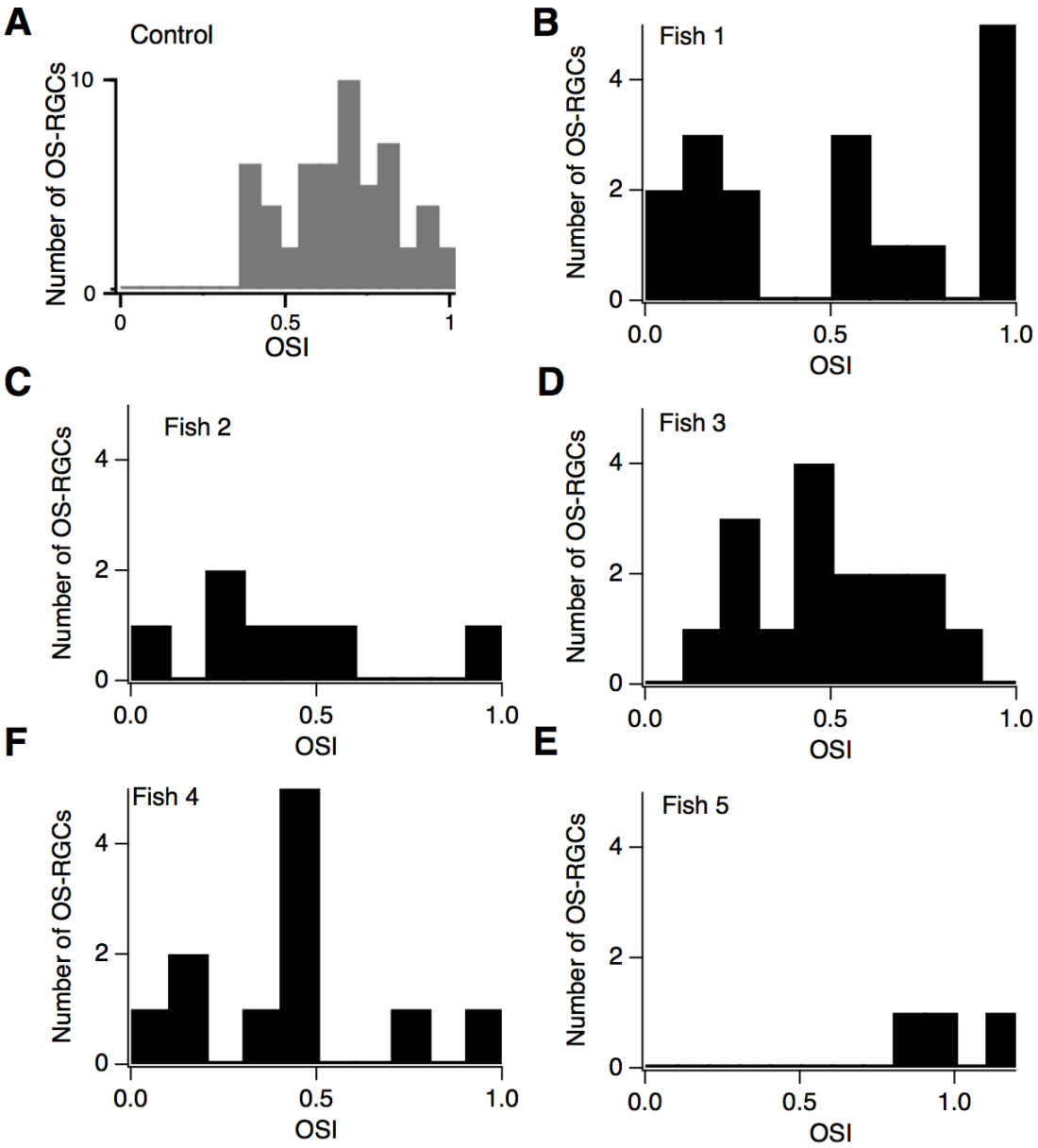

Figure 5.8. Inhibition disruption decreases the OSI of OS-RGCs.

A. OSI in control.

B-F. OSI after inhibition disruption for each fish.

5.4. Discussion

5.4.1. IGluSnFR is a powerful tool to understand how retinal ganglion cells receive and transmit visual information

In this chapter I showed three main points by using IGluSnFR to record the signals at the level of RGCs:
- iGluSnFR was not detecting spillover from other RGCs in the optic tectum.
- It is possible to observe direct inputs from BCs onto RGCs.
- It is then possible to compare the inputs and outputs to understand how RGCs filter and modify the inputs signals. For the first time, the excitatory inputs and outputs of RGCs can be monitored *in vivo*. It would be interesting to visualize the inhibitory input from ACs onto RGCs to have a complete understanding of what are the inputs of RGCs and how RGCs transform this signal.

Other fluorescence reporters are currently being developed for visualising the release of other neurotransmitters like GABA. This would make it possible for the study into RGC computations with iGluSnFR to include recordings of the inhibitory inputs onto the RGCs. The laboratory of Loren Looger is currently developing such reporters. New indicators for GABA (GABASnFR) or acetylcholine (AcetylcholiSnFR) (some ACs named CHAT cells release acetylcholine that is acting as a neuromodulator (Taylor and Smith, 2012) could be used in combination with IGluSnFR to obtain a full understanding about the inhibitory and excitatory inputs of RGCs *in vivo*. This would shed light on how RGCs compute visual information.

5.4.2. Is DPC computed by ACs?

Using iGluSnFR, I was able to observe DPC in RGCs synapses. To understand whether ACs were responsible for the computation of DPC, I injected GABA and Glycine antagonist to block inhibition. When I disrupted the inhibition, I did not observe a change in the percentage of cells that exhibit DPC responses. This

suggests that inhibition does not shape DPC. This is contradictory to what Hosoya et al. (2005) observed when they blocked inhibition in their experiments. However, the disruption of inhibition appears to remove the sustained part of RGC responses. This suggests that ACs are at least modulating DPC. Moreover, a circuit model from Lagnado's laboratory (Johnston et al., 2018) showed that it is possible to generate DPC responses with feedforward inhibition onto RGCs. As mentioned before, one way to further investigate the role of inhibition would be to repeat the iGluSnFR experiment using increased concentrations of the drugs injected in the vitreous chamber of the retina.

Another drawback of this experiment is that ACs are performing a lot of computations (feedforward inhibition, feedback inhibition or lateral inhibition). Disrupting inhibition may completely change the state of the retina. The effects that I observed may therefore not reflect the role played by ACs under physiological conditions. An interesting experiment would be to selectively block the AC feedback or feedforward inhibition. Unfortunately, there is no known method that enables such experiments. However, blocking the lateral inhibition would be possible by only injecting glycine antagonists. It would be interesting to realize this experiment.

Not all the RGCs were able to compute DPC. Therefore, it would be interesting to study if RGCs that are able to compute DPC can be categorised according to their morphology or other RGC characteristics, such as the size or the lamination of the dendrites in the IPL, the receptors density or the area of the optic tectum where these RGCs are projecting to.

5.4.3. Other effects on blocking inhibition could explain the increase of orientation selectivity at 90 degrees

A surprising result was the increase of 90 degrees OS RGCs after disrupting inhibition. Different hypothesis could explain these results.

The ACs could play only a role in 0 degrees orientation selectivity of RGCs and could inhibit the orientation selectivity of 90 degrees of RGCs. However, this is not what my colleagues observed in the laboratory: 118/532 dendrites express 90 degrees orientation selectivity whereas 105/532 exhibit 0 degrees orientation selectivity (data from Lagnado's laboratory (Johnston et al., 2018). Thus, by disrupting the inhibition, I should have the same effect for each orientation selectivity. Injecting GABA and Glycine in the vitreous chamber of the retina could have additional effects that do not come from the IPL, such as effects on horizontal cells. The neurotransmitter that lateral inhibition is using at the level of terminals is still a matter of debate (Kramer and Davenport, 2015). Several studies showed that GABA plays a part in inhibition in the OPL (Hurd and Eldred, 1989; Lam et al., 1978; Schwartz, 1982; Kaneko and Tachibana, 1986, Wu, 1992). GABA is involved in the Horizontal cell-photoreceptor synapse, but does not mediate feedback, it has a role in slow modulation. It is involved in a shunting inhibition effect on negative feedback, this is described by Endeman et al., (2012): chloride currents in cones modify feedback from horizontal cells to cones in goldfish retina.

Thus, while I disrupted inhibition at the level of the IPL, computation at the level of the OPL might be disrupted as well. Hence, other strategies could be used to determine the role of inhibition in generating orientation selectivity by selectively targeting the ACs population. Different genetics tools exist. For instance, expressing the optogenetic tool killerRed (Williams et al., 2013) in ACs will lead to a permanent suppression of these cells. However, there would be numerous side effects such as inflammation of the tissue. Another approach would be to use chemogenetics such as Designer Receptors Exclusively Activated by Designer Drugs (DREADDs) (Roth, 2016; Zhu et al., 2016). DREADDs are engineered G-protein coupled receptors which can be exclusively activated by the designer drug clozapine N-oxide (CNO). They can be used to selectively silence (Gi-based DREADDs) a specific neuronal population. It would be possible to selectively express DREADDs in ACs and silence them by injecting CNO in the retina.

Chapter 6

Discussion

6.1. Introduction

This thesis aims to understand how visual information is transmitted with the synaptic release of glutamate by *in vivo* imaging of the fluorescent reporter iGluSnFR and SF-iGluSnFR. I presented two different aspects of how iGluSnFR (and SF-iGluSnFR) could be used to understand glutamate neurotransmission in zebrafish visual system. iGluSnFR can be used to record the inputs and outputs of neurons such as RGCs (Chapter 5). It is then possible to directly study how the inputs are modified by the neuron recorded and such computation is modulated by inhibitory neurons. Another important breakthrough with iGluSnFR is that it allows one to count vesicles at a single active zone of BCs terminals *in vivo* (Chapter 3). The study published previously about MVR in BCs (Singer et al., 2014) did not use visual stimuli and the experiments were performed *ex vivo*.

The existence of MVR in the central nervous system has been controversial mainly due to the difficulty of demonstrating that the signals recorded was generated by single active zones. In chapter 3, I showed that BCs can generate MVR *in vivo* in response to visual stimulations and that this MVR was produced by the coordination of vesicular release. Moreover, recordings with different contrast visual stimuli revealed that BCs can produce MVR with up to 12 units per event (Figure 4.5.). The previous study could only detect events with up to 4 vesicles (Singer et al., 2004). Finally, several properties of MVR are described in this thesis such as the high temporal precision of MVR (less than 3 ms for events larger than 9 vesicles) (Figure 4.11.) and different numbers of vesicles per event are used to encode different contrasts (see Chapter 4).

Since the work of Katz, it has been assumed for a long time that release sites within a terminal are independent. As mentioned before (see 1.1. and 3.1.), ribbon synapses are an interesting system to study because they contain several release sites within the same active zone and many vesicles are tethered to the ribbon, near the release sites. Such structural arrangements suggest that the ribbon act like a safety belt or a conveying belt that coordinate vesicle release. Singer et al. (2004) found that the MVR at bipolar synapses was coordinated.

With *in vivo* experiments, I also observed (Chapter 3) that the release sites within single active zones are not independent. What are the mechanisms underlying this coordinated MVR? A natural progression of my work could be to model MVR within BCs active zones to understand the molecular mechanisms underlying this coordinated MVR. It could be coordinated by a mechanism of compound fusion (fusion of two vesicles or more together before fusion with the plasma membrane). This compound fusion might be facilitated by influx of calcium. Therefore, calcium spikes could trigger a higher number of vesicles released simultaneously. Modelling could help to understand what mechanisms are involved in MVR.

It would be also interesting to study MVR at ribbon synapses in other systems such as photoreceptors because how glutamate vesicles are released at photoreceptor synapses has never been studied *in vivo*. It is possible for instance to express SF-iGluSnFR in photoreceptors using the promoter gnat2. Several studies suggested that photoreceptors release vesicles in a graded fashion (see review in Heidelberger, 2007). Hence studying how photoreceptors are encoding visual information with the vesicle code may reveal different properties of MVR in photoreceptors than the ones for BC terminals and may give insights into how BCs compute information received from photoreceptors and how photoreceptor outputs are passed into BCs parallel pathways.

6.2. Imaging the retina *in vivo* with two-photon microscopy

Compared to electrophysiological recordings of neural activities, optical recording methods have advantages to study biological systems *in vivo* and enable to access certain neurons that are otherwise difficult to approach. However, two problems can arise with this method. First, the laser can activate the retinal photoreceptors (direct laser-evoked effects). During one photon absorption, the range of absorption for the optical recording probes are typically between 350-700 nm. This band of wavelength is very well absorbed by photoreceptors. Hence neuronal responses to visual stimulations will be disrupted by the laser. Two-

photon microscopy minimizes this problem. The wavelength I used for my experiments (940 nm) will not be absorbed effectively by the photoreceptors. The onset of the laser can trigger a laser response I observed this effect in some of my experiments (more in the experiments of chapter 5). However, after few seconds, the fluorescence returns to the baseline indicating that photoreceptors are adapted to the weak activation light by the two-photon laser. Concerning my experiments, all the visual stimuli were presented 10 s after the start of the laser scanning. Moreover, I used SF-iGluSnFR with the tryptophan system, which expresses brighter version of the sensor (super fold version) and has higher expression level of the sensor (see Chapter 2). This allowed me to use a much lower laser power than the laser power necessary for IGluSnFR. Although photoreceptors do not absorb 940 nm wavelength light effectively, the laser would be still enough to saturate rods (Euler et al., 2009). However even if rods are present in *Danio Rerio* at 3 dpf, they start to be functional at 14 dpf (Bilotta et al., 2001). Hence rod saturation was not a problem with my experiments performed between 7 and 9 dpf.

The second problem for the optical recordings is photoactivation effect by sensors. I used fluorescent probes such as iGluSnFR or SF-iGluSnFR to perform my experiments. When excited, the probe emits photons isotropically that can reach the photoreceptors and excite the retina (indirect laser evoked effects). This activation can be minimized by scanning smaller areas. In the chapters 3 and 4 of this thesis, I performed experiments with linescans (see Chapter 3). This minimized the issue.

Hence, I conclude that I took all the precautions during my experiments to minimize the effects of the laser and the laser-evoked responses negligibly interfere with the visual stimulations presented.

6.3. OFF pathway encodes contrasts better than ON pathway

Among cells that exhibit MVR, two major differences between ON and OFF cells have been established in this study: 1) OFF cells have the capability to release higher number of quanta per event than ON cells (Figure 4.5.) and 2) OFF cells have a higher temporal precision (Figure 4.10.). It seems that OFF cells encode a larger range of information than ON cells. Several reasons can be could explain this observation.

It has been shown that natural scene contains more negative contrasts (around 60%) than positive contrast (Ratliff et al., 2010). It is possible that the retina has evolved to better analyse negative contrasts than positive contrasts. Therefore, OFF pathway would have a major role in contrast discrimination compared to ON pathway. This could explain why OFF cells release more vesicles per event than ON cells as I observed during my experiments.

There is also some evidence showing that the OFF pathway is sufficient to compute visual information. In 1986, Schiller et al. performed an experiment in which they reversibly inhibited the ON pathway in the retina of rhesus monkeys. First, primates have been trained to perform different visual tasks such as recognition of shape, colours, movement, flicker or stereo images. After blocking the ON pathway, the performance for the tasks was rarely changed except monkeys took longer time to discriminate visual objects. This suggests that ON pathway is not necessary to analyse visual information but is needed to increase the vision processing efficiency. However, the converse of this experiment has never been performed: whether OFF pathway is necessary or more important than the ON pathway to transmit visual information: It has been shown that the OFF pathway was implicated in survival behaviours in zebrafish such as escaping to a predator. Escape response can be evoked by a looming stimulus (a classical stimulus known to initiate defensive behaviour (Yilmaz and Meister, 2013; Temizer et al., 2015). This looming stimulus consists in having a negative contrast circle that increases above the head of zebrafish. The RGCs that are necessary to trigger this behaviour were shown to have dendrites in the OFF layer, thus they receive mostly inputs from OFF BCs. Hence, the OFF pathway is the major player

to detect this feature. This could explain why OFF BCs have a more complex range of tools and can communicate more information to the brain than ON cells.

Several studies suggested that only one channel is enough to transmit visual signals (Schiller et al., 1986, Romeny, 2017). However, it appears that it would cost a lot of energy to convey sufficient amount of information in one channel (Romeny, 2017) because it requires higher activity of neurons. On the other hand, having two channels allows an increase of contrast sensitivity and fasten the process of visual transmission with lower activity of neurons by acting as a subtraction frame camera. In this context, OFF channel transfers the most visual information and the ON channel serves to fasten the transmission and add additional information.

6.4. How is visual information transformed at the level of single neurons?

In chapter 5, I studied the glutamatergic inputs and outputs of RGCs (Figure 5.3.). I showed that it was possible to use this information to study the roles of different RGCs partners in computations such as DPC for instance, BCs generate orientation selective inputs. This will help to model this phenomenon. Other experiments could have been done to complete the study of the circuitry of DPC (chapter 5) such as recording glutamatergic inputs of BCs onto ACs to understand what could be the excitatory inputs of BCs onto ACs. However, the promoter to label ACs, ptf1a (Jusuf and Harris, 2009) does not drive the expression of iGluSnFR strongly enough and the expression of iGluSnFR disappears after 5 dpf. Hence, one of the drawbacks would have been that the ACs would not have been mature enough (the circuitry of the retina is enough developed from 7 dpf).

This optical method could be used in combination with the method used in Chapter 3 and 4 to understand transfer how neurons communicate with the vesicle code. Vesicles release onto a neuron as inputs and vesicles release as

outputs could be measured. Another work could be to establish a new characterization of neuronal type based on their own vesicle code. For instance, in chapter 5, how many vesicles are encoding orientation selectivity and how many vesicles are constituting RGCs outputs? It is likely that RGCs are not performing coordinated MVR but it would be worthwhile to understand how the number of vesicles constituting the RGCs inputs are changes into the output of RGCS. It would be interesting to use these data to model neural computations. Since there are different cell types in RGCs or BCs, they use different strategies to encode information (Baden et al., 2016) and they may have their own vesicle code (frequency of release, number of vesicles released per stimulation or per event or the number of vesicles needed to trigger a response might varies by cell type). It would be interesting to understand different types of vesicle code and to link this vesicle code with the morphology of the cells, their connections with other neurons or it location in the retina. Moreover, combining iGluSnFR with a calcium reporter (a red calcium indicator for instance) in RGCs could reveal how vesicles signals are integrated by RGCs. This could complete the work that I performed in chapter 3, 4 and 5.

Chapter 7

Bibliography

Adrian, E.D., and Matthews, R. (1928). The action of light on the eye. J. Physiol. *65*, 273–298.

Akerboom, J., Carreras Calderón, N., Tian, L., Wabnig, S., Prigge, M., Tolö, J., Gordus, A., Orger, M.B., Severi, K.E., Macklin, J.J., et al. (2013). Genetically encoded calcium indicators for multi-color neural activity imaging and combination with optogenetics. Front. Mol. Neurosci. *6*, 2.

Akitake, C.M., Macurak, M., Halpern, M.E., and Goll, M.G. (2011). Transgenerational analysis of transcriptional silencing in zebrafish. Dev. Biol. *352*, 191–201.

Antinucci, P., and Hindges, R. (2018). Orientation-Selective Retinal Circuits in Vertebrates. Front. Neural Circuits *12*, 11.

Antinucci, P., Suleyman, O., Monfries, C., and Hindges, R. (2016). Neural Mechanisms Generating Orientation Selectivity in the Retina. Curr. Biol. CB *26*, 1802–1815.

Arnth-Jensen, N., Jabaudon, D., and Scanziani, M. (2002). Cooperation between independent hippocampal synapses is controlled by glutamate uptake. Nat. Neurosci. *5*, 325–331.

Arshavsky, V.Y., and Burns, M.E. (2012). Photoreceptor signaling: supporting vision across a wide range of light intensities. J. Biol. Chem. *287*, 1620–1626.

Asakawa, K., and Kawakami, K. (2008). Targeted gene expression by the Gal4-UAS system in zebrafish. Dev. Growth Differ. *50*, 391–399.

Asari, H., and Meister, M. (2012). Divergence of visual channels in the inner retina. Nat. Neurosci. *15*, 1581–1589.

Ashmore, J.F., and Copenhagen, D.R. (1983). An analysis of transmission from cones to hyperpolarizing bipolar cells in the retina of the turtle. J. Physiol. *340*, 569–597.

Auger, C., Kondo, S., and Marty, A. (1998). Multivesicular release at single functional synaptic sites in cerebellar stellate and basket cells. J. Neurosci. Off. J. Soc. Neurosci. *18*, 4532–4547.

Ayoub, G. S., Matthews. G. (1992). Substance P modulates calcium current in retinal bipolar neurons.Vis Neurosci. 8(6): 539–544.

Baccus, S.A. (2007). Timing and Computation in Inner Retinal Circuitry. Annu. Rev. Physiol. *69*, 271–290.

Baccus, S.A., and Meister, M. (2002). Fast and slow contrast adaptation in retinal circuitry. Neuron *36*, 909–919.

Baden, T., Esposti, F., Nikolaev, A., and Lagnado, L. (2011). Spikes in Retinal Bipolar Cells Phase-Lock to Visual Stimuli with Millisecond Precision. Curr. Biol. *21*, 1859–1869.

Baden, T., Euler, T., Weckström, M., and Lagnado, L. (2013). Spikes and ribbon synapses in early vision. Trends Neurosci. *36*, 480–488.

Baden, T., Nikolaev, A., Esposti, F., Dreosti, E., Odermatt, B., and Lagnado, L. (2014). A synaptic mechanism for temporal filtering of visual signals. PLoS Biol. *12*, e1001972.

Barlow, H.B., and Levick, W.R. (1965). The mechanism of directionally selective units in rabbit's retina. J. Physiol. *178*, 477–504.

Barlow, H.B., and Levick, W.R. (1969). Changes in the maintained discharge with adaptation level in the cat retina. J. Physiol. *202*, 699–718.

Barlow, H.B., Hill, R.M., and Levick, W.R. (1964). Retinal ganglion cells responding selectively to direction and speed of image motion in the rabbit. J. Physiol. *173*, 377–407.

Beck, J.C., Gilland, E., Tank, D.W., and Baker, R. (2004). Quantifying the ontogeny of optokinetic and vestibuloocular behaviors in zebrafish, medaka, and goldfish. J. Neurophysiol. *92*, 3546–3561.

Berntson, A., and Taylor, W.R. (2003). The unitary event amplitude of mouse retinal on-cone bipolar cells. Vis. Neurosci. *20*, 621–626.

Berry, M.J., and Meister, M. (1998). Refractoriness and neural precision. J. Neurosci. Off. J. Soc. Neurosci. *18*, 2200–2211.

Berry, M.J., Warland, D.K., and Meister, M. (1997). The structure and precision of retinal spike trains. Proc. Natl. Acad. Sci. *94*, 5411–5416.

Berry, M.J., Brivanlou, I.H., Jordan, T.A., and Meister, M. (1999). Anticipation of moving stimuli by the retina. Nature *398*, 334–338.

Bianco, I.H., and Engert, F. (2015). Visuomotor transformations underlying hunting behavior in zebrafish. Curr. Biol. CB *25*, 831–846.

Bianco, I.H., Ma, L.-H., Schoppik, D., Robson, D.N., Orger, M.B., Beck, J.C., Li, J.M., Schier, A.F., Engert, F., and Baker, R. (2012). The tangential nucleus controls a gravito-inertial vestibulo-ocular reflex. Curr. Biol. CB *22*, 1285–1295.

Bilotta, J. , Saszik, S. and Sutherland, S. E. (2001), Rod contributions to the electroretinogram of the dark-adapted developing zebrafish. Dev. Dyn., 222: 564-570.

Bloomfield, S.A. (1994). Orientation-sensitive amacrine and ganglion cells in the rabbit retina. J. Neurophysiol. *71*, 1672–1691.

Borghuis, B.G., Marvin, J.S., Looger, L.L., and Demb, J.B. (2013). Two-Photon Imaging of Nonlinear Glutamate Release Dynamics at Bipolar Cell Synapses in the Mouse Retina. J. Neurosci. *33*, 10972–10985.

Boynton, R.M., and Whitten, D.N. (1970). Visual Adaptation in Monkey Cones: Recordings of Late Receptor Potentials. Science *170*, 1423–1426.

Bringmann A, Grosche A, Pannicke T, Reichenbach A.(2013). GABA and glutamate uptake and metabolism in retinal glial (Müller) cells. Front Endocrinol (Lausanne).;4:48

Brunel, N., and Nadal, J.P. (1998). Mutual information, Fisher information, and population coding. Neural Comput. *10*, 1731–1757.

Burns, M.E., and Baylor, D.A. (2001). Activation, deactivation, and adaptation in vertebrate photoreceptor cells. Annu. Rev. Neurosci. *24*, 779–805.

Butts, D.A., and Goldman, M.S. (2006). Tuning curves, neuronal variability, and sensory coding. PLoS Biol. *4*, e92.

Cajal, S.R. y (1972). The structure of the retina (C. C. Thomas).

Ceppellini, R., Siniscalco, M., and Smith, C.A. (1955). The estimation of gene frequencies in a random-mating population. Ann. Hum. Genet. *20*, 97–115.

Chander, D., and Chichilnisky, E.J. (2001). Adaptation to temporal contrast in primate and salamander retina. J. Neurosci. Off. J. Soc. Neurosci. *21*, 9904–9916.

Chen, X., Hsueh, H.-A., Greenberg, K., and Werblin, F.S. (2010). Three forms of spatial temporal feedforward inhibition are common to different ganglion cell types in rabbit retina. J. Neurophysiol. *103*, 2618–2632.

Choi, S.-Y., Borghuis, B.G., Borghuis, B., Rea, R., Levitan, E.S., Sterling, P., and Kramer, R.H. (2005). Encoding light intensity by the cone photoreceptor synapse. Neuron *48*, 555–562.

Clements, J.D., Lester, R.A., Tong, G., Jahr, C.E., and Westbrook, G.L. (1992). The time course of glutamate in the synaptic cleft. Science *258*, 1498–1501.

Connaughton, V.P. (2011). Bipolar cells in the zebrafish retina. Vis. Neurosci. *28*, 77–93.

Connaughton, V.P., Graham, D., and Nelson, R. (2004). Identification and morphological classification of horizontal, bipolar, and amacrine cells within the zebrafish retina. J. Comp. Neurol. *477*, 371–385.

Dana, H., Mohar, B., Sun, Y., Narayan, S., Gordus, A., Hasseman, J.P., Tsegaye, G., Holt, G.T., Hu, A., Walpita, D., et al. (2016). Sensitive red protein calcium indicators for imaging neural activity. ELife *5*.

Dayan, P. (2005). Theoretical Neuroscience: Computational And Mathematical Modeling of Neural Systems (Massachusetts Institute of Technology Press).

De Sevilla Müller, L.P., Liu, J., Solomon, A., Rodriguez, A., and Brecha, N.C. (2013). Expression of Voltage-Gated Calcium Channel α2δ4 Subunits in the Mouse and Rat Retina. J. Comp. Neurol. *521*, 2486–2501.

Delgado, R., Maureira, C., Oliva, C., Kidokoro, Y., and Labarca, P. (2000). Size of vesicle pools, rates of mobilization, and recycling at neuromuscular synapses of a Drosophila mutant, shibire. Neuron *28*, 941–953.

Demb, J.B. (2008). Functional circuitry of visual adaptation in the retina. J. Physiol. *586*, 4377–4384.

Dempster, A.P., Laird, N.M., and Rubin, D.B. Maximum Likelihood from Incomplete Data via the EM Algorithm. 39.

Denk, W. (1994). Two-photon scanning photochemical microscopy: mapping ligand-gated ion channel distributions. Proc. Natl. Acad. Sci. U. S. A. *91*, 6629–6633.

Denk, W., and Svoboda, K. (1997). Photon upmanship: why multiphoton imaging is more than a gimmick. Neuron *18*, 351–357.

Denk, W., Strickler, J.H., and Webb, W.W. (1990). Two-photon laser scanning fluorescence microscopy. Science *248*, 73–76.

Derrington, A.M., Krauskopf, J., and Lennie, P. (1984). Chromatic mechanisms in lateral geniculate nucleus of macaque. J. Physiol. *357*, 241–265.

DeVries S.H. (2000). Bipolar cells use kainate and AMPA receptors to filter visual information into separate channels. Neuron*.28*, 847–856

DeVries S.H., Schwartz E.A. (1999). Kainate receptors mediate synaptic transmission between cones and 'Off' bipolar cells in a mammalian retina. Nature. *397*, 157–160

Ding, H., Smith, R.G., Poleg-Polsky, A., Diamond, J.S., and Briggman, K.L. (2016). Species-specific wiring for direction selectivity in the mammalian retina. Nature *535*, 105–110.

Distel, M., Wullimann, M.F., and Köster, R.W. (2009). Optimized Gal4 genetics for permanent gene expression mapping in zebrafish. Proc. Natl. Acad. Sci. U. S. A. *106*, 13365–13370.

Do, C.B., and Batzoglou, S. (2008). What is the expectation maximization algorithm? Nat. Biotechnol. *26*, 897–899.

Dorostkar, M.M., Dreosti, E., Odermatt, B., and Lagnado, L. (2010). Computational processing of optical measurements of neuronal and synaptic activity in networks. J. Neurosci. Methods *188*, 141–150.

Dreosti, E., Odermatt, B., Dorostkar, M.M., and Lagnado, L. (2009). A genetically encoded reporter of synaptic activity in vivo. Nat. Methods *6*, 883–889.

Dreosti, E., Esposti, F., Baden, T., and Lagnado, L. (2011). In vivo evidence that retinal bipolar cells generate spikes modulated by light. Nat. Neurosci. *14*, 951–952.

Edmonds, B.W., Gregory, F.D., and Schweizer, F.E. (2004). Evidence that fast exocytosis can be predominantly mediated by vesicles not docked at active zones in frog saccular hair cells. J. Physiol. *560*, 439–450.

Eggers, E.D., and Lukasiewicz, P.D. (2006). GABA(A), GABA(C) and glycine receptor-mediated inhibition differentially affects light-evoked signalling from mouse retinal rod bipolar cells. J. Physiol. *572*, 215–225.

Ellis-Davies, Graham C R (2009). “Basics of photoactivation.” Cold Spring Harbor protocols.

Endeman, D., Fahrenfort, I., Sjoerdsma, T., Steijaert, M., Ten Eikelder, H., and Kamermans, M. (2012). Chloride currents in cones modify feedback from horizontal cells to cones in goldfish retina. J. Physiol. *590*, 5581–5595.

Enroth-Cugell, C., and Lennie, P. (1975). The control of retinal ganglion cell discharge by receptive field surrounds. J. Physiol. *247*, 551–578.

Esposti, F., Johnston, J., Rosa, J.M., Leung, K.-M., and Lagnado, L. (2013). Olfactory stimulation selectively modulates the OFF pathway in the retina of zebrafish. Neuron *79*, 97–110.

Euler, T., and Masland, R.H. (2000). Light-evoked responses of bipolar cells in a mammalian retina. J. Neurophysiol. *83*, 1817–1829.

Euler, T., Hausselt, S.E., Margolis, D.J. et al. Pflugers (2009). Eyecup scope—optical recordings of light stimulus-evoked fluorescence signals in the retina.- Eur J Physiol 457: 1393.

Euler, T., Haverkamp, S., Schubert, T., and Baden, T. (2014). Retinal bipolar cells: elementary building blocks of vision. Nat. Rev. Neurosci. *15*, 507–519.

Feinberg, A.P., and Vogelstein, B. (1983). Hypomethylation distinguishes genes of some human cancers from their normal counterparts. Nature *301*, 89–92.

Feinberg, A.P., Ohlsson, R., and Henikoff, S. (2006). The epigenetic progenitor origin of human cancer. Nat. Rev. Genet. *7*, 21–33.

Flores-Herr, N., Protti, D.A., and Wässle, H. (2001). Synaptic currents generating the inhibitory surround of ganglion cells in the mammalian retina. J. Neurosci. Off. J. Soc. Neurosci. *21*, 4852–4863.

Franke, K., and Baden, T. (2017). General features of inhibition in the inner retina. J. Physiol. *595*, 5507–5515.

Franke, K., Berens, P., Schubert, T., Bethge, M., Euler, T., and Baden, T. (2017). Inhibition decorrelates visual feature representations in the inner retina. Nature *542*, 439–444.

Freed, M.A. (2000). Parallel cone bipolar pathways to a ganglion cell use different rates and amplitudes of quantal excitation. J. Neurosci. Off. J. Soc. Neurosci. *20*, 3956–3963.

Garrick, D., Fiering, S., Martin, D.I., and Whitelaw, E. (1998). Repeat-induced gene silencing in mammals. Nat. Genet. *18*, 56–59.

Glowatzki, E., and Fuchs, P.A. (2002). Transmitter release at the hair cell ribbon synapse. Nat. Neurosci. *5*, 147–154.

Goldberg, J.M., and Brown, P.B. (1969). Response of binaural neurons of dog superior olivary complex to dichotic tonal stimuli: some physiological mechanisms of sound localization. J. Neurophysiol. *32*, 613–636.

Goll, M.G., Anderson, R., Stainier, D.Y.R., Spradling, A.C., and Halpern, M.E. (2009). Transcriptional Silencing and Reactivation in Transgenic Zebrafish. Genetics *182*, 747–755.

Gollisch, T., and Meister, M. (2008). Rapid neural coding in the retina with relative spike latencies. Science *319*, 1108–1111.

Gollisch, T., and Meister, M. (2010). Eye smarter than scientists believed: Neural computations in circuits of the retina. Neuron *65*, 150–164.

Gordon, G.R.J., and Bains, J.S. (2005). Noradrenaline triggers multivesicular release at glutamatergic synapses in the hypothalamus. J. Neurosci. Off. J. Soc. Neurosci. *25*, 11385–11395.

Granseth, B., Odermatt, B., Royle, S.J., and Lagnado, L. (2006). Clathrin-mediated endocytosis is the dominant mechanism of vesicle retrieval at hippocampal synapses. Neuron *51*, 773–786.

Gratzl, M., Dahl, G., Russell, J.T., and Thorn, N.A. (1977). Fusion of neurohypophyseal membranes in vitro. Biochim. Biophys. Acta *470*, 45–57.

Grimes, W.N. (2012). Amacrine cell-mediated input to bipolar cells: variations on a common mechanistic theme. Vis. Neurosci. *29*, 41–49.

Heidelberger, R. (2007). Mechanisms of tonic, graded release: lessons from the vertebrate photoreceptor. J. Physiol. *585*, 663–667.

Helassa, N., Durst, C., Coates, C., Kerruth, S., Arif, U., Schulze, C., Wiegert, J.S., Geeves, M., Oertner, T., and Torok, K. (2017). Ultrafast glutamate sensors resolve synaptic short-term plasticity. BioRxiv 233494.

Heuser, J.E., and Reese, T.S. (1973). Evidence for recycling of synaptic vesicle membrane during transmitter release at the frog neuromuscular junction. J. Cell Biol. *57*, 315–344.

Hires, S.A., Zhu, Y., and Tsien, R.Y. (2008). Optical measurement of synaptic glutamate spillover and reuptake by linker optimized glutamate-sensitive fluorescent reporters. Proc. Natl. Acad. Sci. U. S. A. *105*, 4411–4416.

Holt, M., Cooke, A., Neef, A., and Lagnado, L. (2004). High mobility of vesicles supports continuous exocytosis at a ribbon synapse. Curr. Biol. CB *14*, 173–183.

Hosoya, T., Baccus, S.A., and Meister, M. (2005). Dynamic predictive coding by the retina. Nature *436*, 71–77.

Hubel, D.H., and Wiesel, T.N. (1974). Sequence regularity and geometry of orientation columns in the monkey striate cortex. J. Comp. Neurol. *158*, 267–293.

Hurd, L.B., and Eldred, W.D. (1989). Localization of GABA- and GAD-like immunoreactivity in the turtle retina. Vis. Neurosci. *3*, 9–20.

Isaacson, J.S. (1999). Glutamate spillover mediates excitatory transmission in the rat olfactory bulb. Neuron *23*, 377–384.

James, B., Darnet, L., Moya-Diaz, J., Seibel, S.-H., and Lagnado, L. (2018). An amplitude code increases the efficiency of information transmission across a visual synapse. BioRxiv 328682.

Johnston, J., and Lagnado, L. (2015). General features of the retinal connectome determine the computation of motion anticipation. ELife *4*.

Johnston, J., Seibel, S.-H., Darnet, L.S.A., Renninger, S., Orger, M., and Lagnado, L. (2018). A retinal circuit generating a dynamic predictive code for orientated features. BioRxiv 331504.

Jusuf, P.R., and Harris, W.A. (2009). Ptf1a is expressed transiently in all types of amacrine cells in the embryonic zebrafish retina. Neural Develop. *4*, 34.

Kaneko, A., and Tachibana, M. (1986). Effects of gamma-aminobutyric acid on isolated cone photoreceptors of the turtle retina. J. Physiol. *373*, 443–461.

Katz, B. (1969). The Release of Neural Transmitter Substances.

Kim, K.J., and Rieke, F. (2001). Temporal contrast adaptation in the input and output signals of salamander retinal ganglion cells. J. Neurosci. Off. J. Soc. Neurosci. *21*, 287–299.

Kim, K.J., and Rieke, F. (2003). Slow Na+ inactivation and variance adaptation in salamander retinal ganglion cells. J. Neurosci. Off. J. Soc. Neurosci. *23*, 1506–1516.

Kobat, D., Horton, N.G., and Xu, C. (2011). In vivo two-photon microscopy to 1.6-mm depth in mouse cortex. J. Biomed. Opt. *16*, 106014.

Koike, C., Numata, T., Ueda, H., Mori, Y., and Furukawa, T. (2010). TRPM1: a vertebrate TRP channel responsible for retinal ON bipolar function. Cell Calcium *48*, 95–101.

Korn, H., and Faber, D.S. (1991). Quantal analysis and synaptic efficacy in the CNS. Trends Neurosci. *14*, 439–445.

Korn, H., Mallet, A., Triller, A., and Faber, D.S. (1982). Transmission at a central inhibitory synapse. II. Quantal description of release, with a physical correlate for binomial n. J. Neurophysiol. *48*, 679–707.

Korn, H., Sur, C., Charpier, S., Legendre, P., and Faber, D.S. (1994). The one-vesicle hypothesis and multivesicular release. Adv. Second Messenger Phosphoprotein Res. *29*, 301–322.

Kramer, R.H., and Davenport, C.M. (2015). Lateral Inhibition in the Vertebrate Retina: The Case of the Missing Neurotransmitter. PLOS Biol. *13*, e1002322.

Kuromi, H., and Kidokoro, Y. (2000). Tetanic stimulation recruits vesicles from reserve pool via a cAMP-mediated process in Drosophila synapses. Neuron *27*, 133–143.

Lagnado, L., Gomis, A., and Job, C. (1996). Continuous vesicle cycling in the synaptic terminal of retinal bipolar cells. Neuron *17*, 957–967.

Lam, D.M., Lasater, E.M., and Naka, K.I. (1978). gamma-Aminobutyric acid: a neurotransmitter candidate for cone horizontal cells of the catfish retina. Proc. Natl. Acad. Sci. U. S. A. *75*, 6310–6313.

Lampl, I., and Katz, Y. (2017). Neuronal adaptation in the somatosensory system of rodents. Neuroscience *343*, 66–76.

Lee, S., and Zhou, Z.J. (2006). The synaptic mechanism of direction selectivity in distal processes of starburst amacrine cells. Neuron *51*, 787–799.

Lettvin, J.Y., Maturana, H.R., McCulloch, W.S., and Pitts, W.H. (1959). What the Frog's Eye Tells the Frog's Brain. Proc. IRE *47*, 1940–1951.

Li J, Wang Y, Chiu S-L and Cline HT (2010). Membrane targeted horseradish peroxidase as a marker for correlative fluorescence and electron microscopy studies. Front. Neural Circuits 4:6.

Li, G.-L., Cho, S., and von Gersdorff, H. (2014). Phase-locking precision is enhanced by multiquantal release at an auditory hair cell ribbon synapse. Neuron *83*, 1404–1417.

Li, Y.N., Tsujimura, T., Kawamura, S., and Dowling, J.E. (2012). Bipolar Cell-Photoreceptor Connectivity in the Zebrafish (Danio rerio) Retina. J. Comp. Neurol. *520*, 3786–3802.

Lipin, M.Y., and Vigh, J. (2015). Calcium spike-mediated digital signaling increases glutamate output at the visual threshold of retinal bipolar cells. J. Neurophysiol. *113*, 550–566.

LoGiudice, L., and Matthews, G. (2009). The role of ribbons at sensory synapses. Neurosci. Rev. J. Bringing Neurobiol. Neurol. Psychiatry *15*, 380–391.

Mackay, D.M. (1970). Elevation of visual threshold by displacement of retinal image. Nature *225*, 90–92.

Mainen, Z.F., Maletic-Savatic, M., Shi, S.H., Hayashi, Y., Malinow, R., and Svoboda, K. (1999a). Two-photon imaging in living brain slices. Methods San Diego Calif *18*, 231–239, 181.

Mainen, Z.F., Malinow, R., and Svoboda, K. (1999b). Synaptic calcium transients in single spines indicate that NMDA receptors are not saturated. Nature *399*, 151–155.

Manookin, M.B., and Demb, J.B. (2006). Presynaptic mechanism for slow contrast adaptation in mammalian retinal ganglion cells. Neuron *50*, 453–464.

Marmarelis, P.Z., and Naka, K.I. (1973). Nonlinear analysis and synthesis of receptive-field responses in the catfish retina. 3. Two-input white-noise analysis. J. Neurophysiol. *36*, 634–648.

Marvin, J.S., Borghuis, B.G., Tian, L., Cichon, J., Harnett, M.T., Akerboom, J., Gordus, A., Renninger, S.L., Chen, T.-W., Bargmann, C.I., et al. (2013). An optimized fluorescent probe for visualizing glutamate neurotransmission. Nat. Methods *10*, 162–170.

Marvin, J.S., Scholl, B., Wilson, D.E., Podgorski, K., Kazemipour, A., Mueller, J.A., Schoch-McGovern, S., Wang, S.S.-H., Quiroz, F.J.U., Rebola, N., et al. (2017). Stability, affinity and chromatic variants of the glutamate sensor iGluSnFR. BioRxiv 235176.

Masland, R.H. (1996). Processing and encoding of visual information in the retina. Curr. Opin. Neurobiol. *6*, 467–474.

Masland, R.H. (2005). Sensory Systems: Fine-Tuning the Visual Scene. Curr. Biol. *15*, R808–R810.

Matsuzaki M, Ellis-Davies GC, Nemoto T, Miyashita Y, Iino M, Kasai H (2001). Dendritic spine geometry is critical for AMPA receptor expression in hippocampal CA1 pyramidal neurons. *Nat Neurosci.*;4(11):1086-92.

Matthews, G., and Fuchs, P. (2010). The diverse roles of ribbon synapses in sensory neurotransmission. Nat. Rev. Neurosci. *11*, 812–822.

Matthews, G., and Sterling, P. (2008). Evidence that vesicles undergo compound fusion on the synaptic ribbon. J. Neurosci. Off. J. Soc. Neurosci. *28*, 5403–5411.

Mehta, B., Snellman, J., Chen, S., Li, W., and Zenisek, D. (2013). Synaptic ribbons influence the size and frequency of miniature-like evoked postsynaptic currents. Neuron *77*, 516–527.

Meister, M., and Berry, M.J. (1999). The neural code of the retina. Neuron *22*, 435–450.

Mennerick, S., and Matthews, G. (1996). Ultrafast exocytosis elicited by calcium current in synaptic terminals of retinal bipolar neurons. Neuron *17*, 1241–1249.

Movshon, J.A., Thompson, I.D., and Tolhurst, D.J. (1978). Spatial and temporal contrast sensitivity of neurones in areas 17 and 18 of the cat's visual cortex. J. Physiol. *283*, 101–120.

Müller, J.R., Metha, A.B., Krauskopf, J., and Lennie, P. (1999). Rapid adaptation in visual cortex to the structure of images. Science *285*, 1405–1408.

Nakajima Y, Iwakabe H, Akazawa C, Nawa H, Shigemoto R, Mizuno N, Nakanishi S (1993). Molecular characterization of a novel retinal metabotropic glutamate receptor mGluR6 with a high agonist selec- tivity for L-2-amino-4-phosphonobutyrate. J Biol Chem *268*, 11868-11873.

Namiki, S., Sakamoto, H., Iinuma, S., Iino, M., and Hirose, K. (2007). Optical glutamate sensor for spatiotemporal analysis of synaptic transmission. Eur. J. Neurosci. *25*, 2249–2259.

Nikolaev, A., Leung, K.-M., Odermatt, B., and Lagnado, L. (2013). Synaptic mechanisms of adaptation and sensitization in the retina. Nat. Neurosci. *16*, 934.

Nomura A, Shigemoto R, Nakamura Y, Okamoto N, Mizuno N, Nakani- shi S (1994). Developmentally regulated postsynaptic localization of a metabotropic glutamate receptor in rat rod bipolar cells. Cell *77*, 361-369.

Normann, R.A., and Perlman, I. (1979). The effects of background illumination on the photoresponses of red and green cones. J. Physiol. *286*, 491–507.

Odermatt, B., Nikolaev, A., and Lagnado, L. (2012). Encoding of luminance and contrast by linear and nonlinear synapses in the retina. Neuron *73*, 758–773.

Oertner, T.G., Sabatini, B.L., Nimchinsky, E.A., and Svoboda, K. (2002). Facilitation at single synapses probed with optical quantal analysis. Nat. Neurosci. *5*, 657–664.

Okumoto, S., Looger, L.L., Micheva, K.D., Reimer, R.J., Smith, S.J., and Frommer, W.B. (2005). Detection of glutamate release from neurons by genetically encoded surface-displayed FRET nanosensors. Proc. Natl. Acad. Sci. U. S. A. *102*, 8740–8745.

Olveczky, B.P., Baccus, S.A., and Meister, M. (2003). Segregation of object and background motion in the retina. Nature *423*, 401–408.

Otori Y, Shimada S, Tanaka T, Ishimoto I, Tana Y, Tohyama M. Marked. (1994) Increase in glutamate-aspartate transporter (GLAST/GluT-1) mRNA following transient retinal ischemia. Brain Res Mol Brain Res. 27:310–314.

Parsons, T.D., and Sterling, P. (2003). Synaptic ribbon. Conveyor belt or safety belt? Neuron *37*, 379–382.

Pédelacq, J.-D., Cabantous, S., Tran, T., Terwilliger, T.C., and Waldo, G.S. (2006). Engineering and characterization of a superfolder green fluorescent protein. Nat. Biotechnol. *24*, 79–88.

Pérez-González, D., and Malmierca, M.S. (2014). Adaptation in the auditory system: an overview. Front. Integr. Neurosci. *8*.

Pologruto, T.A., Sabatini, B.L., and Svoboda, K. (2003). ScanImage: flexible software for operating laser scanning microscopes. Biomed. Eng. Online *2*, 13.

Pouget, A., Deneve, S., Ducom, J.C., and Latham, P.E. (1999). Narrow versus wide tuning curves: What's best for a population code? Neural Comput. *11*, 85–90.

Pugh, E.N., Nikonov, S., and Lamb, T.D. (1999). Molecular mechanisms of vertebrate photoreceptor light adaptation. Curr. Opin. Neurobiol. *9*, 410–418.

Rampino, M.A.F., and Nawy, S.A. (2011). Relief of Mg2+-dependent Inhibition of TrpM1 by PKCα at the Rod – Bipolar Cell Synapse. J. Neurosci. Off. J. Soc. Neurosci. *31*, 13596–13603.

Ratliff, C.P., Borghuis, B.G., Kao, Y.-H., Sterling, P., and Balasubramanian, V. (2010). Retina is structured to process an excess of darkness in natural scenes. Proc. Natl. Acad. Sci. U. S. A. *107*, 17368–17373.

Rauen, T., and Wiessner, M. (2000). Fine tuning of glutamate uptake and degradation in glial cells: common transcriptional regulation of GLAST1 and GS. *Neurochem. Int.* 37, 179–189.

Redman, S. (1990). Quantal analysis of synaptic potentials in neurons of the central nervous system. Physiol. Rev. *70*, 165–198.

Regus-Leidig, H., and Brandstätter, J.H. (2012). Structure and function of a complex sensory synapse. Acta Physiol. Oxf. Engl. *204*, 479–486.

Richards, D.A., Guatimosim, C., and Betz, W.J. (2000). Two endocytic recycling routes selectively fill two vesicle pools in frog motor nerve terminals. Neuron *27*, 551–559.

Rieke, F. (2001). Temporal contrast adaptation in salamander bipolar cells. J. Neurosci. Off. J. Soc. Neurosci. *21*, 9445–9454.

Robles, E., Laurell, E., and Baier, H. (2014). The Retinal Projectome Reveals Brain-Area-Specific Visual Representations Generated by Ganglion Cell Diversity. Curr. Biol. *24*, 2085–2096.

Rodieck, R.W. (1965). Quantitative analysis of cat retinal ganglion cell response to visual stimuli. Vision Res. *5*, 583–601.

Romeny, B.M. ter H. (2017). Energy saving in vision at the first synapse: The ON and OFF pathways measure temporal differences. BioRxiv 225557.

Rosa, J.M., Ruehle, S., Ding, H., and Lagnado, L. (2016). Crossover Inhibition Generates Sustained Visual Responses in the Inner Retina. Neuron *90*, 308–319.

Roska, B., Nemeth, E., and Werblin, F.S. (1998). Response to change is facilitated by a three-neuron disinhibitory pathway in the tiger salamander retina. J. Neurosci. Off. J. Soc. Neurosci. *18*, 3451–3459.

Roth, B.L. (2016). DREADDs for Neuroscientists. Neuron *89*, 683–694.

Rudolph, S., Tsai, M.-C., von Gersdorff, H., and Wadiche, J.I. (2015). The ubiquitous nature of multivesicular release. Trends Neurosci. *38*, 428–438.

Sakai, H.M., Wang, J.L., and Naka, K. (1995). Contrast gain control in the lower vertebrate retinas. J. Gen. Physiol. *105*, 815–835.

Saszik, S., and DeVries, S.H. (2012). A mammalian retinal bipolar cell uses both graded changes in membrane voltage and all-or-nothing Na+ spikes to encode light. J. Neurosci. Off. J. Soc. Neurosci. *32*, 297–307.

Savitzky, A.; Golay, M.J.E. (1964). Smoothing and Differentiation of Data by Simplified Least Squares Procedures. Analytical Chemistry. *36*, 1627–1639.

Schikorski, T., and Stevens, C.F. (1997). Quantitative ultrastructural analysis of hippocampal excitatory synapses. J. Neurosci. Off. J. Soc. Neurosci. *17*, 5858–5867.

Schiller, P.H., Sandell, J.H., and Maunsell, J.H. (1986). Functions of the ON and OFF channels of the visual system. Nature *322*, 824–825.

Schultz K, Stell WK. (1996). Immunocytochemical localization of the high-affinity glutamate transporter, EAAC1, in the retina of representative vertebrate species. Neurosci Lett. 211:191–194.

Schwartz, E.A. (1982). Calcium-independent release of GABA from isolated horizontal cells of the toad retina. J. Physiol. *323*, 211–227.

Seriès, P., Latham, P.E., and Pouget, A. (2004). Tuning curve sharpening for orientation selectivity: coding efficiency and the impact of correlations. Nat. Neurosci. *7*, 1129–1135.

Shapley, R. (1997). Retinal physiology: adapting to the changing scene. Curr. Biol. CB *7*, R421-423.

Shapley, R. (2009). Linear and nonlinear systems analysis of the visual system: why does it seem so linear? A review dedicated to the memory of Henk Spekreijse. Vision Res. *49*, 907–921.

Shapley, R., and Enroth-Cugell, C. (1984). Chapter 9 Visual adaptation and retinal gain controls. Prog. Retin. Res. *3*, 263–346.

Singer, J.H., Lassová, L., Vardi, N., and Diamond, J.S. (2004). Coordinated multivesicular release at a mammalian ribbon synapse. Nat. Neurosci. *7*, 826.

Sjostrand, F.S. (1953). The ultrastructure of the innersegments of the retinal rods of the guinea pig eye as revealed by electron microscopy. J. Cell. Comp. Physiol. *42*, 45–70.

Sjostrand, F.S. (1958). Ultrastructure of retinal rod synapses of the guinea pig eye as revealed by three-dimensional reconstructions from serial sections. J. Ultrastruct. Res. *2*, 122–170.

Skavenski, A.A., Hansen, R.M., Steinman, R.M., and Winterson, B.J. (1979). Quality of retinal image stabilization during small natural and artificial body rotations in man. Vision Res. *19*, 675–683.

Smirnakis, S.M., Berry, M.J., Warland, D.K., Bialek, W., and Meister, M. (1997). Adaptation of retinal processing to image contrast and spatial scale. Nature *386*, 69–73.

Solomon, S.G., White, A.J., and Martin, P.R. (1999). Temporal contrast sensitivity in the lateral geniculate nucleus of a New World monkey, the marmoset Callithrix jacchus. J. Physiol. *517 (Pt 3)*, 907–917.

Spekreijse, H., and Norton, A.L. (1970). The dynamic characteristics of color-coded S-potentials. J. Gen. Physiol. *56*, 1–15.

Squire, L.R. (2009). Encyclopedia of Neuroscience: Volume One (Academic Press).

Srinivasan, M.V., Laughlin, S.B., and Dubs, A. (1982). Predictive coding: a fresh view of inhibition in the retina. Proc. R. Soc. Lond. B Biol. Sci. *216*, 427–459.

Stevens, C.F. (2003). Neurotransmitter Release at Central Synapses. Neuron *40*, 381–388.

Sulaiman, P., Fina, M., Feddersen, R., and Vardi, N. (2010). Ret-PCP2 colocalizes with protein kinase C in a subset of primate ON cone bipolar cells. J. Comp. Neurol. *518*, 1098–1112.

Sulaiman, P., Xu, Y., Fina, M.E., Tummala, S.R., Ramakrishnan, H., Dhingra, A., and Vardi, N. (2013). Kir2.4 Surface Expression and Basal Current Are Affected by Heterotrimeric G-Proteins. J. Biol. Chem. *288*, 7420–7429.

Suli, A., Guler, A.D., Raible, D.W., and Kimelman, D. (2014). A targeted gene expression system using the tryptophan repressor in zebrafish shows no silencing in subsequent generations. Dev. Camb. Engl. *141*, 1167–1174.

Szapiro, G., and Barbour, B. (2007). Multiple climbing fibers signal to molecular layer interneurons exclusively via glutamate spillover. Nat. Neurosci. *10*, 735–742.

Tanaka K. Functions of glutamate transporters in the brain. (2000). Neurosci Res. May;37(1):15-9.

Tartuferi, F. (1887). Sull'anatomia della retina. Int. Monatsschrift Anat. Physiol. *4*, 421–441.

Taylor, W.R., and Smith, R.G. (2012). The role of starburst amacrine cells in visual signal processing. Vis. Neurosci. *29*, 73–81.

Temizer, I., Donovan, J.C., Baier, H., and Semmelhack, J.L. (2015). A Visual Pathway for Looming-Evoked Escape in Larval Zebrafish. Curr. Biol. CB *25*, 1823–1834.

Tong, G., and Jahr, C.E. (1994). Multivesicular release from excitatory synapses of cultured hippocampal neurons. Neuron *12*, 51–59.

Tranchina, D., Sneyd, J., and Cadenas, I.D. (1991). Light adaptation in turtle cones. Testing and analysis of a model for phototransduction. Biophys. J. *60*, 217–237.

Vaney, D.I., and Taylor, W.R. (2002). Direction selectivity in the retina. Curr. Opin. Neurobiol. *12*, 405–410.

de Vries, S.E.J., Baccus, S.A., and Meister, M. (2011). The projective field of a retinal amacrine cell. J. Neurosci. Off. J. Soc. Neurosci. *31*, 8595–8604.

Wadiche, J.I., and Jahr, C.E. (2001). Multivesicular release at climbing fiber-Purkinje cell synapses. Neuron *32*, 301–313.

Walker, A.S., Burrone, J., and Meyer, M.P. (2013). Functional imaging in the zebrafish retinotectal system using RGECO. Front. Neural Circuits *7*, 34.

Wässle, H., and Boycott, B.B. (1991). Functional architecture of the mammalian retina. Physiol. Rev. *71*, 447–480.

Webster, M.A. (2012). Evolving concepts of sensory adaptation. F1000 Biol. Rep. *4*.

Werblin, F.S. (1970). Response of retinal cells to moving spots: intracellular recording in Necturus maculosus. J. Neurophysiol. *33*, 342–350.

Werblin, F.S., and Copenhagen, D.R. (1974). Control of retinal sensitivity. 3. Lateral interactions at the inner plexiform layer. J. Gen. Physiol. *63*, 88–110.

Wiener, N. (1964). Extrapolation, Interpolation, and Smoothing of Stationary Time Series (The MIT Press).

Williams, D.C., Bejjani, R.E., Ramirez, P.M., Coakley, S., Kim, S.A., Lee, H., Wen, Q., Samuel, A., Lu, H., Hilliard, M.A., et al. (2013). Rapid and permanent neuronal inactivation in vivo via subcellular generation of reactive oxygen with the use of KillerRed. Cell Rep. *5*, 553–563.

Wu, S.M. (1992). Feedback connections and operation of the outer plexiform layer of the retina. Curr. Opin. Neurobiol. *2*, 462–468.

Wu, J., Abdelfattah, A.S., Miraucourt, L.S., Kutsarova, E., Ruangkittisakul, A., Zhou, H., Ballanyi, K., Wicks, G., Drobizhev, M., Rebane, A., et al. (2014). A long Stokes shift red fluorescent Ca2+ indicator protein for two-photon and ratiometric imaging. Nat. Commun. *5*, 5262.

Wu, L.-G., Ryan, T.A., and Lagnado, L. (2007). Modes of Vesicle Retrieval at Ribbon Synapses, Calyx-Type Synapses, and Small Central Synapses. J. Neurosci. *27*, 11793–11802.

Yilmaz, M., and Meister, M. (2013). Rapid innate defensive responses of mice to looming visual stimuli. Curr. Biol. CB *23*, 2011–2015.

Zhang, J., Jung, C.S., and Slaughter, M.M. (1997). Serial inhibitory synapses in retina. Vis. Neurosci. *14*, 553–563.

Zhao, Y., Araki, S., Wu, J., Teramoto, T., Chang, Y.-F., Nakano, M., Abdelfattah, A.S., Fujiwara, M., Ishihara, T., Nagai, T., et al. (2011). An expanded palette of genetically encoded Ca^{2+} indicators. Science *333*, 1888–1891.

Zhu, H., Aryal, D.K., Olsen, R.H.J., Urban, D.J., Swearingen, A., Forbes, S., Roth, B.L., and Hochgeschwender, U. (2016). Cre dependent DREADD (Designer

Receptors Exclusively Activated by Designer Drugs) mice. Genes. N. Y. N 2000 *54*, 439–446.

Zucker, R.S. (1973). Changes in the statistics of transmitter release during facilitation. J. Physiol. *229*, 787–810.